NASA TECHNICAL MEMORANDUM

NASA TM-73747

NASA TM-73747

(NASA-TM-73747) IDENTIFICATION AND MEASUREMENT OF COMBUSTION NOISE FROM A TURBOFAN ENGINE USING CORRELATION AND COHERENCE TECHNIQUES Ph.D. Thesis (NASA) 156 p HC A08/MF A01 CSCL 20A G3/07

N77-33162

Unclas 49137

IDENTIFICATION AND MEASUREMENT OF COMBUSTION NOISE FROM A TURBOFAN ENGINE USING CORRELATION AND COHERENCE TECHNIQUES

by Allen M. Karchmer
Lewis Research Center
Cleveland, Ohio 44135
September 1977

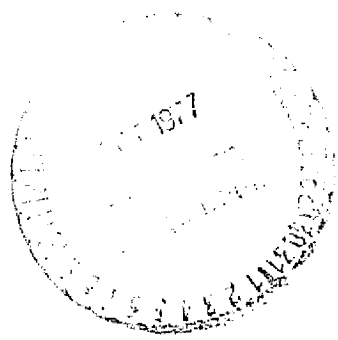

1. Report No.	2. Government Accession No.	3. Recipient's Catalog No.
NASA TM-73747		

4. Title and Subtitle	5. Report Date
IDENTIFICATION AND MEASUREMENT OF COMBUSTION NOISE FROM A TURBOFAN ENGINE USING CORRELATION AND COHERENCE TECHNIQUES	September 1977
	6. Performing Organization Code
7. Author(s)	8. Performing Organization Report No.
Allen M. Karchmer	E-9319
	10. Work Unit No.
9. Performing Organization Name and Address	
National Aeronautics and Space Administration Lewis Research Center Cleveland, Ohio 44135	11. Contract or Grant No.
	13. Type of Report and Period Covered
12. Sponsoring Agency Name and Address	Technical Memorandum
National Aeronautics and Space Administration Washington, D.C. 20546	14. Sponsoring Agency Code

15. Supplementary Notes

Thesis submitted in partial fulfillment of the requirements for the Degree of Doctor of Philosophy.

16. Abstract

Fluctuating pressure measurements within the combustor and tailpipe of a turbofan engine are made simultaneously with far-field acoustic measurements. The pressure measurements within the engine are accomplished with cooled "semi-infinite" waveguide probes utilizing conventional condenser microphones as the transducers. The measurements are taken over a broad range of engine operating conditions and for 16 far-field microphone positions between 10° and 160° relative to the engine inlet axis. Correlation and coherence techniques are used to determine the relative phase and amplitude relationships between the internal pressures and far-field acoustic pressures. The results indicate that the combustor is a low frequency source region for acoustic propagation through the tailpipe and out to the far-field. Specifically, it is found that the relation between source pressure and the resulting sound pressure involves a 180° phase shift. This latter result is obtained by Fourier transforming the cross-correlation function between the source pressure and acoustic pressure after removing the propagation delay time. Further, it is found that the transfer function between the source pressure and acoustic pressure has a magnitude approximately proportional to frequency squared. These results are shown to be consistent with a model using a modified source term in Lighthill's turbulence stress tensor, wherein the fluctuating Reynolds stresses are replaced with the pressure fluctuations due to fluctuating entropy. Finally, the measured ordinary coherence functions between fluctuating combustor pressure and far-field acoustic pressures are used to obtain the far-field combustor associated noise in terms of spectra, directivity, and acoustic power. The results so obtained are compared with various existing empirical prediction procedures and are found to be in good agreement with respect to directivity patterns, but somewhat low when compared with respect to acoustic power.

17. Key Words (Suggested by Author(s))	18. Distribution Statement
Combustion noise; Correlation; Coherence; Aircraft noise; Core noise; Aeroacoustics; Noise identification	Unclassified - unlimited STAR Category 71

19. Security Classif. (of this report)	20. Security Classif. (of this page)	21. No. of Pages	22. Price*
Unclassified	Unclassified		

* For sale by the National Technical Information Service, Springfield, Virginia 22161

IDENTIFICATION AND MEASUREMENT OF COMBUSTION NOISE FROM A TURBOFAN ENGINE USING CORRELATION AND COHERENCE TECHNIQUES

Abstract

by

ALLEN MARTIN KARCHMER

Fluctuating pressure measurements within the combustor and tailpipe of a turbofan engine are made simultaneously with far-field acoustic measurements. The pressure measurements within the engine are accomplished with cooled "semi-infinite" waveguide probes utilizing conventional condenser microphones as the transducers. The measurements are taken over a broad range of engine operating conditions and for sixteen far-field microphone positions between 10° and 160° relative to the engine inlet axis. Correlation and coherence techniques are used to determine the relative phase and amplitude relationships between the internal pressures and far-field acoustic pressures. The results indicate that the combustor is a low frequency source region for acoustic propagation through the tailpipe and out to the far-field. Specifically, it is found that the relation between source pressure and the resulting sound pressure involves a 180° phase shift. This latter result is obtained by Fourier transforming the cross-correlation function between the source pressure and acoustic pressure after removing the propagation

delay time. Further, it is found that the transfer function between the source pressure and acoustic pressure has a magnitude approximately proportional to frequency squared. These results are shown to be consistent with a model using a modified source term in Lighthill's turbulence stress tensor, wherein the fluctuating Reynolds stresses are replaced with the pressure fluctuations due to fluctuating entropy. Finally, the measured ordinary coherence functions between fluctuating combustor pressure and far field acoustic pressures are used to obtain the far-field combustor associated noise in terms of spectra, directivity and acoustic power. The results so obtained are compared with various existing empirical prediction procedures and are found to be in good agreement with respect to directivity patterns, but somewhat low when compared with respect to acoustic power.

ACKNOWLEDGMENTS

I wish to thank my thesis advisor, Professor Isaac Greber for his continuous interest, support, and encouragement throughout this research program. I would also like to express my gratitude to several of my colleagues at NASA Lewis: Dr. Marvin Goldstein, whose insight and understanding of aeroacoustics have provided continuous guidelines throughout the course of this work and who generously gave of his time for many helpful, stimulating, and fruitful discussions; Mr. Eugene Krejsa, with whom I held many useful discussions on the interpretation of some of the experimental data; Mr. Meyer Reshotko, who provided invaluable assistance in data acquisition; and Mr. Paul Penko, who supervised and directed engine operations.

Appreciation is also expressed to Mrs. Judy Ragone and Mrs. Kathleen Dorsey for their typing services and to the Editorial Branch and Graphics Branch of NASA Lewis for their help in preparing the manuscript and illustrations.

I also wish to thank the Lewis Training Committee, especially Miss Gertrude Collins, whose support made this work possible.

Finally, I wish to express my deepest gratitude to my wife, Marcia, for her patience, understanding, and continuous encouragement throughout this effort.

CONTENTS

LIST OF TABLES

LIST OF FIGURES

Figures

1. INTRODUCTION

Noise, defined as unwanted or excessive sound, is a relatively local phenomenon affecting only the immediate vicinity of its source, and does not accumulate in the environment. Nevertheless it is now broadly recognized as a form of environmental degradation. Noise can be annoying, can interfere with sleep, work, or recreation and, under some circumstances, may cause physical and psychological damage.

The most prevalent noise sources in society today stem from transportation operations with aircraft noise playing a particularly significant role, especially since the introduction of jet powered aircraft into commercial service in the late 1950's. Because of increasing public concern with the environment and the phenomenal growth of commercial aviation in this country (predicted to reach 430 million flight operations per year by 1985 (ref. 1)) aircraft noise abatement has become a major objective of both industry and government.

Efforts to reduce airport community noise have essentially taken two paths. The first is through a multitude of aircraft and airport operational procedures such as the multi-segment approach, power cutback and turnouts after takeoff, runway restrictions, the establishment of airport buffer zones, land use control, and even

curfews. Operational restrictions such as these, however, can only be partially effective or are limited in their implementation because of local conditions or safety considerations. The second approach, and the one where the preponderance of research effort is concentrated is aimed at the reduction or alteration of the primary aircraft noise source itself, the propulsion system.

A jet powered propulsion system is a complex acoustic source. It is composed of a number of individual but interrelated noise sources. While these sources are not strictly independent of one another, we can generally associate with each of the noise sources within a turbofan engine some identifiable physical generating mechanism and acoustic characteristics which, in turn, are usually related to specific components of the engine. It is entirely appropriate, therefore, when analyzing the constituents of aircraft propulsion system noise to analyze them (or synthesize, when predicting) on an engine component by component basis.

Figure 1, for example, is an illustration of a typical turbofan engine, schematically depicting the primary component noise sources. The noise which is emitted from the inlet and from the fan discharge duct is generated principally by the fan and, to a lesser extent, by the compressor. The fan is responsible for the high frequency whine heard principally on approach and primarily forward of the aircraft. The noise emitted by the primary jet exhaust at the rear of the engine is generated by the violent turbulent mixing between the high velocity exhaust jet and the rela-

tively quiescent ambient environment. This turbulent mixing noise is responsible for the low frequency roar which is heard principally on takeoff and primarily in the rear of the aircraft. Less important, but not insignificant, is the noise generated by the secondary, or fan, jet exhaust as well as turbine noises which are emitted at the rear of the engine. Finally, there are noises associated with the combustion of the air-fuel mixture, as well as noises due to the interaction of the engine gases as they flow through, over and around various internal surfaces and passages.

These latter sources, because they originate in the gas generator section, or core, of the turbofan, have collectively been given the name core noise. For virtually all of the aircraft in commercial service today, fan and jet noise are thought to be, by significant margins, the dominant contributors to overall engine noise, with core noise sources relatively unimportant.

In recent years, however, there have been substantially increased research efforts to determine the causes, generating mechanisms, and characteristics of core associated noise in turbofan engines. There are a number of reasons for this and these will be briefly discussed.

The general conclusion that the fan and jet are the primary sources of turbofan engine noise has, for the most part, been reached as a result of extensive model nozzle, fan and full scale engine static tests; that is, tests under nonflight conditions. It has long been recognized, however, that jet mixing noise is significantly reduced by forward motion as a result of the reduction of

the relative velocity between the jet and the ambient atmosphere. One of the earliest analyses of jet noise (by Lighthill, ref. 2) indicated that the total sound power generated by a turbulent jet is proportional to the eighth power of jet velocity. This has since been verified by numerous investigators. Relatively modest reductions in jet velocity, therefore, provide enormous reductions in jet noise. Reduction of jet velocity by 50 percent, for example, results in a 250 fold (24 dB) reduction in sound power. Model jet experiments in various forward velocity simulation facilities (e.g., large free jets, wind tunnels, etc.) have shown similar strong dependencies by the jet noise on the relative velocity between jet and ambient flow, although not as strong as eighth power (refs. 3, 4, 5). Forward motion reduces relative velocity and therefore reduces jet noise generation.

Recent experimental studies (refs. 6 and 7, for example) have also shown reductions in fan noise generation under simulated forward velocity conditions, primarily as a result of inflow cleanup conditions. That is, the forward velocity conditions eliminate or minimize the ingestion of ground vortices or large scale turbulence, thus reducing the noise generated as these flow irregularities pass through the fan.

A significant theoretical effort has also been made in attempts to understand such forward flight effects on fan and jet noise (refs. 3 and 6). For the most part, these analytical approaches are able to predict the acoustic characteristics observed on model nozzles and fans in simulation facilities. However, a comparison of the theo-

retically predicted or experimentally observed model simulation results with the noise characteristics measured from actual aircraft flight tests shows large discrepancies. The flight data generally indicate more noise than would be expected from the theoretical predictions or model simulation tests. The reasons for these discrepancies are not fully understood. Some investigators (refs. 8 and 9), however, have advanced the argument that internal noise sources (i.e., core noise), which are not simulated in model nozzle or fan tests, and which are not observable in static engine tests because of extremely high jet noise levels, become significant contributors to overall engine noise during takeoff or approach when the fan and jet noise are reduced because of forward velocity effects. This would indicate that core noise, consequently, may present a floor to the aircraft noise abatement engineer. If new federal regulations mandate further engine noise reductions, it is possible that the effort will have to be aimed at these core noise sources as well as the fan and the jet.

The second factor stimulating research into core noise is related to the possible development of an advanced supersonic cruise commercial aircraft. In the early 1970's it became obvious that with the then existing technology, a commercial supersonic aircraft would generate unacceptable levels of jet noise because of the extremely high jet velocities. At least partially for this reason, further development work on an American SST was halted. Continued research, however, has recently indicated that inverting the conventional turbofan jet exhaust velocity profile so that the outside (fan) jet has

a greater velocity than the inside (primary, or core) jet results in a significant reduction in jet noise without correspondingly significant thrust losses (refs. 10 and 11).

One proposed method of accomplishing this inversion simply requires direct supplementary combustion in the fan duct. In the conventional turbofan, it is generally thought that the presence of the turbine between combustor and exhaust significantly attenuates combustion associated noise (between 5 and 20 dB, depending on frequency, see ref. 12). It is possible, therefore, that for the duct-burning turbofan, where there is no intervening turbomachinery downstream of the supplementary combustor, combustion noise may be a major contributor to core noise.

It should be noted that although the terms "combustion" noise and "core" noise are often used interchangeably in the literature, they refer to distinctly different phenomena. In the present work, the term "core" noise refers collectively to all noise or noise sources associated with the gas generator of a turbofan. As noted previously this can include compressor noise, turbine noise, noises associated with the gases flowing through, over and around the various internal surfaces and passages, as well as combustion noise. The term "combustion noise" refers only to the noise generated as a result of the combustion process (direct or indirect), and which would be absent if combustion did not take place. This is not a trivial distinction and, in fact, provides a primary motivation for the present work.

A typical procedure in identifying core noise from an engine is to make a series of far-field acoustic measurements at progressively lower engine power settings. Fan, compressor, and turbine noise can generally be identified in the data because of the characteristic tone-like spectra associated with their high rotational speeds. (Alternatively, the fan noise can be muffled, as in ref. 13, and the jet noise can be reduced by replacing the nozzle with a section of straight pipe, as in ref. 14.) The data are then examined for behavior not characteristic of jet noise (e.g., sound power not proportional to the eighth power of jet velocity; improper Strouhal scaling of spectra, etc.). The observed differences are then attributed to internal, or core, noise sources. Such a technique, at best, is imprecise from a quantitative viewpoint, and is unable to qualitatively distinguish one internal source from another.

Several investigators (refs. 15 and 16) have attempted to identify specific regions within the core as contributors to far-field noise by combining internal pressure measurements with far-field acoustic measurements and cross-correlating them. While this approach is generally more useful than acoustic measurements taken only outside the engine, cross-correlation measurements by themselves shed very little light on cause-effect relationships. For example, it is certainly possible, as will be shown later, to have a non-zero correlation between the pressure (or any other fluid property) at some point within the engine and the acoustic pressure outside the engine and yet have the source of the acoustic information at some unidentified other point within the engine. That is, correlation

alone does not demonstrate cause-effect, although examination of time delay information can provide useful information, as was shown in reference 15.

There have also been numerous attempts using a variety of measurement techniques to specifically identify and characterize the noise from gas turbine combustors in non-engine installations. That is, such investigations are conducted on combustors installed in specially designed apparatus which do not contain the additional machinery and hardware (compressor, turbine, nozzle, etc.) associated with a turbofan propulsion system. The techniques range from correlation analysis (ref. 17) and coherence analysis (ref. 18) to simple far field acoustic measurements (ref. 19). In experiments such as these the noise source, of course, is known and the effort involves one of quantifying the combustion noise contribution. It is not clear, however, how the results of these experiments can be applied or related to an actual engine where the presence of the turbine and nozzle can serve to partially attenuate or alter some of the noise generated by the combustor, as well as generate noise themselves.

The present work will describe an experiment conducted on an operating turbofan engine. The objective of the investigation was to determine specifically whether or not the combustor could be identified as a contributor to far-field engine noise and to quantify this contribution. The engine was not modified in any way to reduce the noise generated by the fan or jet. Correlation, coherence, and cross-spectral measurements were made between fluctuating pressures

at various locations within the gas-generating section of the engine and acoustic pressure in the far-field of the engine.

The results of the measurement program are basically divided into two parts: a diagnostic phase which focuses on a rigorous interpretation of certain correlation function characteristics to determine the relationship between internal pressures and far-field acoustic pressure and thus identify acoustic source regions and possible physical generating mechanisms; and a computational phase which presents the quantitative contribution of the combustor associated far-field noise to overall engine noise in terms of spectra, directivity, and level, including acoustic power.

2. PHYSICAL CONSIDERATIONS

2.1 Derivation of Lighthill's Equation

As indicated in the INTRODUCTION, the existence of a correlation between two physical variables in no way implies a cause-effect relationship. However, there is additional information on the relative phase and amplitude between the two variables being correlated. This information can be extracted through the frequency domain representation of the correlation function by the appropriate Fourier transformation of the correlation function. It is this phase and amplitude information which can provide clues as to the nature of the relationship between the two variables.

For example, one expects that if the pressure in an acoustic source region were correlated with the pressure at an acoustic field (i.e., observation) point, then the phase and amplitude relationship derived from that correlation should be consistent with some physical generating, or source mechanism. If, on the other hand, the two pressures being correlated were both simply in the acoustic field of a third point which is a common source for those two, then the phase and amplitude relationship should be consistent with pure time delay. It is this notion upon which the diagnostic phase of the present work is based. It is appropriate at this point, therefore, to

briefly review the derivation and interpretation of the governing equations for aerodynamic noise generation.

In 1952 and 1954, in two now famous papers (refs. 2 and 20), M. J. Lighthill proposed his fundamental theory of noise production by aerodynamic sources alone. Physically, he showed that sound is generated by an unsteady fluid flow exactly as in a uniform medium at rest which is acted upon by certain externally applied fluctuating stresses. His derivation is as follows.

The starting point is the continuity equation

$$\frac{\partial \rho}{\partial t} + \frac{\partial \rho u_i}{\partial x_i} = 0 \tag{1}$$

and the momentum equation (neglecting body forces):

$$\rho \frac{Du_i}{Dt} = \frac{\partial e'_{ij}}{\partial x_j} \tag{2}$$

where

$$\frac{D}{Dt} \equiv \frac{\partial}{\partial t} + u_j \frac{\partial}{\partial x_j}$$

and e'_{ij} is the stress tensor.

The equations are written for an infinite, uniform quiescent medium, which contains a region of turbulent flow. Here ρ = density, and u_i is the component of velocity in the x_i direction ($i = 1,2,3$).

Expanding the material derivative in (2), adding $u_i(\partial \rho u_j / \partial x_j)$ to both sides, and substituting continuity into the result gives:

$$\frac{\partial}{\partial t}(\rho u_i) = \frac{\partial}{\partial x_j}(e'_{ij} - \rho u_i u_j) \tag{3}$$

Differentiating continuity with respect to time, and differentiating (3) with respect to x_i gives, respectively:

$$\frac{\partial^2 \rho}{\partial t^2} + \frac{\partial^2 \rho u_i}{\partial t\, \partial x_i} = 0 \tag{4}$$

and

$$\frac{\partial^2 \rho u_i}{\partial t\, \partial x_i} = \frac{\partial^2}{\partial x_j\, \partial x_i}(e'_{ij} - \rho u_i u_j) \tag{5}$$

Subtracting (5) from (4) and adding $c_0^2(\partial^2\rho/\partial x_i\, \partial x_i)$ to the result gives:

$$\frac{\partial^2 \rho}{\partial t^2} - c_0^2 \frac{\partial^2 \rho}{\partial x_i\, \partial x_i} = \frac{\partial^2}{\partial x_i\, \partial x_j}\left[\rho u_i u_j - e'_{ij} - c^2 \rho \delta_{ij}\right] \tag{6}$$

where c_0 is the constant speed of sound and δ_{ij} is the Kronecker Delta.

For an isotropic Newtonian fluid,

$$e'_{ij} = -\delta_{ij} p + 2\mu\varepsilon_{ij} + \delta_{ij}\lambda\varepsilon_{ii} \tag{7}$$

where

μ is the shear coefficient of viscosity

λ is the bulk coefficient of viscosity

ε_{ij} is the strain rate tensor $= 1/2[(\partial u_i/\partial x_j) + (\partial u_j/\partial x_i)]$

p is the pressure

For the traditional assumption of a Stokesian fluid, $\lambda + 2/3\ \mu \equiv 0$

and (6) becomes:

$$\frac{\partial^2 \rho}{\partial t^2} - c_0^2 \frac{\partial^2 \rho}{\partial x_i \partial x_i} = \frac{\partial^2}{\partial x_i \partial x_j} \left[\rho u_i u_j - e_{ij} + (p - c^2 \rho)\delta_{ij}\right] \qquad (8)$$

where e_{ij} is the viscous part of the stress tensor:

$$e_{ij} = \mu\left[\frac{\partial u_i}{\partial x_j} + \frac{\partial u_j}{\partial x_i} - \frac{2}{3}\frac{\partial u_k}{\partial x_k}\delta_{ij}\right]$$

Finally, then, equation (8) becomes:

$$\frac{\partial^2 \rho}{\partial t^2} - c_0^2 \frac{\partial^2 \rho}{\partial x_i \partial x_i} = \frac{\partial^2}{\partial x_i \partial x_j}(T_{ij})$$

where

$$T_{ij} = \rho u_i u_j - e_{ij} + (p - c^2 \rho)\delta_{ij}$$

Referring the pressure and density to (constant) reference values (subscript 0):

$$\rho' = \rho - \rho_0$$

$$p' = p - p_0$$

Then

$$\frac{\partial^2 \rho'}{\partial t^2} - c_0^2 \frac{\partial^2 \rho'}{\partial x_i \partial x_i} = \frac{\partial^2}{\partial x_i \partial x_j}(T'_{ij}) \qquad (9)$$

where T'_{ij} is known as Lighthill's turbulence stress tensor.

Equation (9) clearly has the <u>form</u> of a wave equation describing the propagation of sound in a stationary medium driven by a distribution of quadrupole sources $\partial^2/\partial x_i \partial x_j (T'_{ij})$. This analogy between the density fluctuations in a real flow and those in an ideal acoustic medium at rest embedded with a distribution of quadrupoles is called Lighthill's acoustic analogy.

More importantly, however, is the fact that equation (9) is an exact equation, at least within the assumptions of the momentum equation, continuity equation, and the assumption of a Newtonian and Stokesian medium. All real flow and acoustic effects are accounted for: refraction, convection, turbulence scattering of acoustic waves, mean flow-acoustic interaction effects, and viscous dissipation of the sound waves by the flow.

Some difficulty arises upon a strict interpretation that the right hand side is a pure source term, and the left-hand side accounts solely for acoustic propagation. The source term, T'_{ij}, contains the fluctuating density, which is the dependent variable being solved for on the left-hand side. Since T'_{ij} is not, in general, an a priori known quantity except for the most trivial of flows, a complete description of the "source term" would imply a solution to the general non-linear flow equations. Note that all the non-linear terms are on the right hand side of (8). The precise description of the effects of refraction, convection, acoustic-flow interactions, etc. would require that a solution of (8) already be in hand.

Nevertheless, Lighthill's equation has been extensively used over the years, particularly for jet noise analysis, where the lack of solid surfaces in the region under consideration permits relatively simple boundary conditions in its solution. Various approaches to incorporate more of the real fluid effects in the wave operator portion of the equation and less in the source term have been developed (for example Lilley in ref. 21, Phillips in ref. 22). These

procedures necessarily deviate from the acoustic analogy approach of Lighthill and although more direct and precise from a computational viewpoint, are less intuitively satisfying from a physical viewpoint.

2.2 Solution of Lighthill's Equation

Lighthill obtained the solution to his equation, in the absence of solid surfaces, as:

$$\rho'(\overline{X},t) = \rho(\overline{X},t) - \rho_0 = \frac{1}{4\pi c_0^2}\int \frac{1}{|\overline{X} - \overline{Y}|}\left[\frac{\partial^2 T'_{ij}(\overline{Y},t')}{\partial y_i \, \partial y_j}\right] d^3\overline{Y} \qquad (10)$$

where

$\overline{X}=\{x_1,x_2,x_3\}$ is the distance from the origin to the observation point

$\overline{Y}=\{y_1,y_2,y_3\}$ is the distance from the origin to a source point

and the brackets indicate that the derivative is to be evaluated at the retarded time $t' = [t - (|\overline{X} - \overline{Y}|)/c]$. The volume integration is to be performed over all space.

It can be shown (ref. 23, e.g.) that at large distances from the source region (i.e., if the observation point $\overline{X}$ is many acoustic wavelengths from any point in the source region) and if, additionally, the distance between the source point and observation point is large compared with the dimensions of the source region (i.e., the observation point is in the radiation field) then the spatial divergence in (10) becomes a time derivative and

$$\rho'(\overline{X},t) \approx \frac{1}{4\pi c_0^4}\frac{x_i x_j}{x^3}\int \frac{\partial^2 T'_{ij}}{\partial t^2}\left(\overline{Y}, t - \frac{r}{c_0}\right)d^3\overline{Y} \qquad (11)$$

with $r = |\overline{X} - \overline{Y}|$. The argument that, at least for isothermal flows, T'_{ij} is a relatively acceptable description of the acoustic sources, and that mean flow-acoustic interactions may be neglected as a first approximation was made by Lighthill and proceeds as follows.

The term under consideration is (see fig. 2):

$$T'_{ij} = (\rho_0 + \rho')u_i u_j - e_{ij} + \left[(p - p_0) - c_0^2(\rho - \rho_0)\right]\delta_{ij} \qquad (12)$$

If the ratio of turbulence or Reynolds stresses to viscous stresses is very large, that is for large Reynolds number, then within the region of turbulence, the term $(\rho_0 + \rho')u_i u_j$ is very large compared to e_{ij}. Within the region of turbulence, therefore, e_{ij} is negligible. Further if the turbulent region is essentially isothermal, then the effects of heat transfer should also be negligible for cases where the ambient temperature is the same as that of the flow. Entropy spottiness within the flow should be negligible, and the isentropic relation between pressure and density changes

$$c^2 = \frac{dp}{d\rho}$$

should hold. Consequently, within the jet $(p - p_0) \approx c_0^2(\rho - \rho_0)$. Hence the T'_{ij} term becomes

$$T'_{ij} \approx (\rho_0 + \rho')u_i u_j$$

Lighthill then assumed that the density fluctuations of the flow are

small compared to the mean density and hence may be neglected, so that finally

$$T'_{ij} \approx \rho_0 u_i u_j$$

In the region outside the flow, only acoustic disturbances need be considered, so that $p' \approx c_0^2 \rho'$, $u_i u_j$ is very small, and viscous effects on the acoustic waves are entirely negligible (24), except for propagation over very large distances. The result, therefore, is that T'_{ij} is approximated by $\rho_0 u_i u_j$ within the region of turbulence, and is zero outside the flow. On this basis, equation (9) can be interpreted as a wave operator governing the propagation of sound whose source is given by T'_{ij} on the right hand side.

Equation (11), which allows the calculation of the density fluctuations in the radiation field once the source term T'_{ij} is known, is the usual starting point for the analysis of noise generated by turbulent mixing, specifically jet noise.

The present work, however, focuses its attention on noise generated in a turbulent combustion region. It is certainly not appropriate, therefore, to neglect entropy spottiness in (12) and assume that $p' - c_0^2 \rho' \approx 0$. Instead, in the region of combustion we retain the "thermal stress" term $p' - c_0^2 \rho'$ as a measure of pressure fluctuations due to fluctuating entropy and neglect the Reynolds stress term. This latter assumption is made on the grounds that even though the turbulence intensity in a combustor may be as high as that in the mixing region of a jet, the flow velocities are relatively low. This would result in a relatively low level of turbulent

mixing noise. The quantity $(p' - c_0^2\rho')$, then, is retained as the only source term. (The viscous stress e_{ij} is still left out.)

Still making the assumption that in the radiation field the flow is isentropic so that here $p' \approx c_0^2\rho'$, equation (11) becomes:

$$p'(\overline{X},t) \approx \frac{1}{4\pi c_0^2 x}\int \frac{\partial^2}{\partial t^2} S'\left(\overline{Y},t - \frac{r}{c_0}\right)d^3\overline{Y} \tag{13}$$

where the source term $S' = p' - c_0^2\rho'$ is a measure of the pressure fluctuations due to local entropy fluctuations.

Following the procedure of Siddon for surface generated noise (ref. 25), equation (13) written for a time, say t', can be multiplied through by the local source pressure at $\overline{Y}$ at an earlier time $t'' - (r/c_0)$ and time averaged:

$$\overline{p'\left(\overline{Y},t'' - \frac{r}{c_0}\right)p'(\overline{X},t')} \propto \int \overline{p'\left(\overline{Y},t'' - \frac{r}{c_0}\right)\frac{\partial^2}{\partial t^2} S'\left(\overline{Y}',t' - \frac{r'}{c_0}\right)}\,d^3\overline{Y}' \tag{14}$$

where the dummy variable $\overline{Y}'$ has been introduced and $r' = |\overline{X} - \overline{Y}'|$. The overbars indicate a long time average.

For flows at low Mach numbers, the retarded time differences can usually be neglected over the correlation volume (25) (i.e., $\overline{r} \approx \overline{r}'$). Furthermore, if $p'(\overline{Y})$ and $p'(\overline{X})$ are individually and jointly stationary random variables, then their cross-correlation function is independent of time translations (26):

$$\overline{p'\left(\overline{Y},t'' - \frac{r}{c_0}\right)p(\overline{X},t')} = \overline{p'(\overline{Y})p'\left(\overline{X},\tau + \frac{r}{c_0}\right)} \qquad (\tau = t' - t'') \tag{15}$$

Similarly, for the integrand on the right hand side of (14)

$$\overline{p'\left(\bar{Y},t'' - \frac{r}{c_0}\right)\frac{\partial^2}{\partial t^2}\,S'\left(\bar{Y}',t' - \frac{r}{c_0}\right)} = \overline{p'(\bar{Y})\,\frac{\partial^2}{\partial t^2}\,S'(\bar{Y}',\tau)} \qquad (16)$$

Putting $\bar{Y}' - \bar{Y} = \bar{\eta}$ and substituting (15) and (16) into (14) gives:

$$\overline{p'(\bar{Y},t)p'(\bar{X},t+\tau')} \propto \int \overline{p'(\bar{Y},t)\,\frac{\partial^2}{\partial t^2}\,S'(\bar{Y}+\bar{\eta},t+\tau)}\,d^3\bar{\eta} \qquad (17)$$

where

$$\tau' = \tau + \frac{r}{c_0}$$

The integrand on the right-hand side of (17) is a two point, space-time correlation between one function and the second time derivative of another function, delayed in time. A theorem relating correlations of jointly stationary random functions to their derivatives may be found in reference 27. It is expressed as:

$$\overline{\frac{d^m}{dt^m}f_1(t)\,\frac{d^n}{dt^n}f_2(t+\tau)} = (-1)^m\,\frac{d^{n+m}}{d\tau^{n+m}}\,\overline{f_1(t)f_2(t+\tau)} \qquad (18)$$

or, in words, the cross-correlation of the time derivatives of two random variables may be contracted to the time derivative of the cross-correlation of the two variables. In equation (17) we have $m = 0$, $n = 2$, so (17) can be written:

$$\overline{p'(\bar{Y},t)p'(\bar{X},t+\tau')} \propto \frac{d^2}{d\tau^2}\int \overline{p'(\bar{Y},t)S'(\bar{Y}+\bar{\eta},t+\tau)}\,d^3\bar{\eta} \qquad (19)$$

If $p'(\bar{Y})$ and S' are uniformly coherent through the entire source volume, then the correlation in the integrand of the right hand side of (18) is independent of $\bar{\eta}$, and (18) becomes:

$$\overline{p'(\bar{Y},t)p'(\bar{X},t+\tau')} \propto V_{corr} \frac{d^2}{d\tau^2} \overline{p'(\bar{Y},t)S'(\bar{Y},t+\tau)} \qquad (20)$$

where V_{corr} is the correlation volume:

$$V_{corr} = \int d^3\bar{\eta} \qquad (21)$$

For a more realistic case, where the relationship between p' and S' in the source region exhibits the properties of decay in space and time, uniform coherence will not prevail and equation (21) is not an adequate representation of the correlation volume. Nevertheless, equation (20) does suggest that as a first approximation we arbitrarily define the correlation volume as

$$V_{corr} \equiv \frac{\int \overline{p'(\bar{Y},t)S'(\bar{Y}+\bar{\eta},t+\tau)} d^3\bar{\eta}}{\overline{p'(\bar{Y},t)S'(\bar{Y},t+\tau)}} \qquad (22)$$

With this definition, then, equation (20) becomes somewhat more general and will form the basis for the diagnostic phase of this investigation.

Subject to the assumptions made to here, (19) states that a cross-correlation between the pressure in a combustion noise source region and the pressure in the (acoustic) radiation field is proportional to the second time derivative of the cross-correlation between that same pressure in the source region and the pressure fluctuations due to fluctuating entropy, at the same point.

The correlation on the right hand side of (19) may be expanded as:

$$\overline{p'(\bar{Y},t)S'(\bar{Y},t+\tau)} = \overline{p'(\bar{Y},t)\left[p'(\bar{Y},t+\tau) - c_0^2\rho'(\bar{Y},t+\tau)\right]}$$

$$= \overline{p'(\bar{Y},t)p'(\bar{Y},t+\tau)} - \overline{p'(\bar{Y},t)c_0^2\rho'(\bar{Y},t+\tau)} \tag{23}$$

The first term on the right-hand side of (23) is simply the autocorrelation of the fluctuating pressure in the source region. The second term is a single-point cross-correlation between the fluctuating pressure and density in the source region. Consequently, if this density and pressure are in phase with each other, or if they are not in phase but their correlation is negligible in comparison with the pressure autocorrelation function, then the entire correlation on the right hand side of (19) must behave as, and therefore satisfy the properties of, an autocorrelation function. (If p' and ρ' are not in phase with each other, it is not likely that they would correlate since there is no reason to expect a systematic phase relationship between them.)

For the present investigation, the two important properties are as follows: an autocorrelation function must be an even function about the $\tau = 0$ axis, i.e., $R(\tau) = R(-\tau)$ for all values of τ; an autocorrelation function must have its maximum value at $\tau = 0$, i.e., $R(0) \geq |R(\tau)|$ for all values of τ. These two properties, then, and the second derivative operation on the right-hand side of (20), define the shape of the correlation on the left-hand side of (20).

Specifically, even order derivatives of an even function must also be even functions. Hence, the correlation on the left-hand side of (20) must be symmetric, and this symmetry must occur at a value of $t = \tau' = r/c_0$, where r is the distance between the source region and the observation point; that is at a time delay corresponding to the acoustic propagation time between the source region and the observation point. Furthermore, since the $p'S'$ correlation should have a positive peak, the second derivative operation requires the left-hand side of (20) to have a negative peak at this axis of symmetry (see fig. 3).

Qualitatively, then, the relationship given by (20) defines the shape of the $p'p'$ correlation. This can be formalized quantitatively by recalling that in the frequency domain the operation corresponding to time differentiation in the time domain is multiplication by frequency and a 90° phase shift. The two time derivatives, then, produce a 180° phase shift and a multiplication by frequency squared.

If the $p'\rho'$ correlation in equation (23) is negligible, then (20) becomes:

$$\overline{p'(\bar{Y},t)p'\left(\bar{X},t+\tau+\frac{r}{c_0}\right)} \propto \frac{d^2}{d\tau^2}\,\overline{p'(\bar{Y},t)p'(\bar{Y},t+\tau)}$$

Taking the Fourier Transform of both sides:

$$G_{\overline{YX}}(j\omega)e^{jr\omega/c_0} \propto -\omega^2 G_{\overline{YY}}(\omega)$$

or

$$\frac{G_{\overline{YX}}(j\omega)}{G_{\overline{YY}}(\omega)} \propto -\omega^2 e^{-jr\omega/c_0} = \omega^2 e^{-j[r(\omega/c_0)\pm\pi]} \tag{24}$$

where $j = \sqrt{-1}$, and $\omega = 2\pi f$ (f = frequency).

Here, $G_{\overline{YX}}(j\omega)$ is the cross-spectral density between $p'(\overline{Y})$ and $p'(\overline{X})$, and $G_{\overline{YY}}(\omega)$ is the auto spectral density of $p'(\overline{Y})$.

Equation (24) is simply the definition of the transfer function between $p'(\overline{Y})$, the fluctuating pressure in the source region, and $p'(\overline{X})$, the fluctuating pressure at an observation point outside the source region:

$$H_{\overline{YX}}(j\omega) \equiv \frac{G_{\overline{X}}(j\omega)}{G_{\overline{YY}}(\omega)} \tag{25}$$

So the transfer function between pressure in the source region and observation pressure has a magnitude proportional to frequency squared, and a phase factor given by $(-r\omega/c_0 \pm \pi)$. The first part of the phase factor, $-r\omega/c_0$, is just due to time delay and depends upon the distance between the two points. It produces a phase shift which is linearly proportional to frequency. The second part of the phase shift results from the second derivative operation and is independent of frequency. These two elements of the transfer function, amplitude, and that part of the phase shift not due to time delay, uniquely determine the relationship between $p'(\overline{X})$ and $p'(\overline{Y})$.

The basic approach used in the diagnostic phase of this investigation was to examine the phase and amplitude relationships between the fluctuating pressure in the combustion region of a turbofan engine and the fluctuating pressure at other locations within the core

of the engine as well is in the acoustic far-field. Measured transfer functions between points within the engine which are consistent with the quantitative results discussed above would indicate measurable combustion noise generation (since the turbulent mixing noise was assumed negligible). Additionally, if the transfer function between the pressure in the combustion region and the acoustic pressure in the engine far-field was also consistent with the above relationships, this would indicate that the combustion noise was, in fact, propagating through the engine and contributing to the overall engine noise.

As will be described in the next section, the core of the engine was instrumented with a number of pressure transducers at locations other than in the combustion region. This was done to characterize and track the pressure signal as it propagated or convected through the core. To accomplish this tracking, the pair-wise time domain (cross correlation) and frequency domain (cross spectral density and coherence) characteristics were measured between points in the core from which noise generated by mechanisms other than combustion might be expected.

Earlier it was mentioned that the combustion process was only one of a number of noise sources which could be identified with the core of a turbofan engine. In addition to the relatively high frequencies associated with the rotating machinery (compressor and turbine) and which can be readily removed from data by appropriate filtering procedures, there is noise generated by the flow of the gases through, over, and around the various internal engine surfaces and

passages. In general, the spectral characteristics of this noise is broadband and not as easily identifiable as rotating machinery noise. The generating mechanisms of this so called "scrubbing" noise, or surface interaction noise is quite different from combustion noise, however. Consequently, if such noise generating mechanisms are significant, they should be identifiable through the appropriate transfer function as described above for combustion associated noise.

Before beginning a description of the experimental work performed, therefore, it is appropriate to briefly describe the characteristics of these noise sources.

Equation (11) is the solution to Lighthill's equation in the absence of solid surfaces. Curle (ref. 28) generalized the solution to Lighthill's equation to predict the acoustic radiation from a region of unsteady flow which contains an embedded surface. His solution, in the geometric and acoustic far-fields was obtained as:

$$p'(X,t) = \frac{1}{4\pi}\int_{\xi}\rho\left[\frac{\partial u_n}{\partial t}\right]d\xi + \frac{x_i}{4\pi x^2 c_0}\int_{\xi}\frac{\partial}{\partial t}\left[f_i + \rho u_i u_n\right]d\xi$$

$$+ \frac{x_i x_j}{4\pi x^3 c_0}\int\left[\frac{\partial^2 T_{ij}}{\partial t^2}\right]d^3\overline{Y} \qquad (26)$$

Here, the brackets denote evaluation at the retarded time $\tau = t - r/c_0$ as in equation (10). The first two terms on the right hand side of (26) are the additional terms associated with the noise generated by the fluid interacting with the surfaces ξ, which are

allowed to deform with surface velocity u_n. The quantity f_i is the local resultant stress at each point on the surface and may have both tangential (shear) and normal (pressure) stress components. The third integral is the contribution from the quadrupole noise from turbulence, as was shown earlier.

Siddon (ref. 25) has shown that for cases where the volume generated noise is weak and when the surfaces are stationary or in rigid steady motion ($\partial u_n/\partial t = 0$), the correlation between source pressure and observation point pressure is given by

$$\overline{p'(\bar{X},t)p'(\bar{Y},t)} \propto A_{corr} \frac{d}{d\tau} \overline{p'(\bar{Y},t)p'(\bar{Y},t+\tau)} \qquad (27)$$

if the source pressure is uniformly coherent over the entire surface ξ. Here A_{corr} is a correlation area analogous to the correlation volume in equation (21). If the source pressure is not uniformly coherent, then A_{corr} may be generalized analogously to V_{corr} in equation (22), with similar restrictions.

It is clear from equation (27) that the transfer function between source pressure $p'(\bar{Y})$ and observation point pressure $p'(\bar{X})$ can be obtained similarly to equation (24) as

$$H_{\overline{YX}}(j\omega) \equiv \frac{G_{\overline{YX}}(j\omega)}{G_{\overline{YY}}(\omega)} \propto \omega e^{-j[(r\omega/c_0)+(\pi/2)]}$$

For surface generated noise, then, the magnitude of the transfer function between source pressure and observation point pressure is linearly proportional to frequency and the part of the phase shift not due to time delay is ±90°, independent of frequency. In the time

domain, the cross-correlation is the first derivative of an even function, and so it will be an odd function, with the axis of anti-symmetry being at a value of $\tau = r/c_0$ (see fig. 3).

We see, then, that the phase and amplitude relationships which prevail between the pressure in a source region and in a non-source region are uniquely determined by the acoustic generating mechanism. The transfer functions, which can be written in terms of the phase and amplitude between the various pressures can then be used to identify this mechanism.

Finally there exists the possibility that neither pressure transducer of a pair within the engine which is being correlated is in a source region. In this case the transfer function between the two should have a constant magnitude (i.e., flat and independent of frequency) and a phase factor due to time delay only. The relative phase between the two which is not due to time delay should be zero.

These relatively straightforward notions regarding transfer functions between pressures within the engine core and/or outside the engine (i.e., the acoustic pressure) form the basis for the diagnostics to be described.

3. DESCRIPTION OF EXPERIMENT

3.1 Engine

The engine which was the object of the current investigation was an AVCO-Lycoming YF-102 turbofan engine. The core, or gas generating section of the engine was originally designed for and used to power gas turbine driven helicopters. The fan stage was added by Lycoming to convert the engine into a turbofan. This engine will eventually be the propulsion system for the NASA Quiet Short-Haul Research Aircraft (QSRA), with the airframe designed and built by The Boeing Company.

A cutaway illustration of this engine in the unmounted configuration is shown in figure 4. The engine has a relatively high by-pass ratio of six to one and a rated thrust of 33 kN. The gas generating section consists of an eight stage compressor, seven axial and one centrifugal, driven by the first two (high pressure) stages of the turbine with a reverse-flow annular combustor. The fan and supercharger are driven through a 2.3 to 1 speed reduction gear by the second two stages (low pressure) of the turbine. The fan is 1 meter in diameter, the primary nozzle exit area is 0.136 square meters (42 cm diam) and the fan nozzle exit area is 0.361 square meter. The engine was tested with a bellmouth inlet to provide for smooth inflow conditions. A photograph of the engine

mounted on the test stand is shown in figure 5.

It should be noted that the reverse flow-combustor in this engine is an unusual arrangement for most aircraft powerplants, especially those in commercial service. Essentially the design represents a compromise made to minimize engine length. As such, it is more appropriate for helicopters and small business jet aircraft. It is possible that the characteristics of combustion noise generated by the annular or can-annular combustors on commercial turbofan engines without reverse flow are different than those of the reverse-flow combustor. This may be particularly true of the spectral content, which is likely to be sensitive to combustor geometry.

The final point to be made about the YF-102 engine concerns its moderately high by-pass ratio of six to one, which permits a relatively low primary jet exhaust velocity of approximately 315 meters/sec at takeoff thrust. This compares with approximately 550 meters/sec primary jet velocity for the Pratt & Whitney JT8D turbofan which has a bypass ratio of 1.05 to one. Because of the much lower jet velocities for the YF-102 engine, the relative combustion noise contribution to overall engine noise may be greater than for an engine like the JT8D, which powers approximately 65 percent of commercial jet aircraft in this country. Consequently, for these reasons, caution should be exercised in generalizing the results to be presented later to the lower bypass ratio turbofan engines with more conventional combustor configurations.

3.2 Internal Pressure Instrumentation

The fluctuating pressure measurements within the engine core were made at seven different locations, as shown in figure 6. Their number and locations were: two just downstream of the compressor exit about 2 cm apart; one at the combustor entrance; two within the annular combustor itself, both at the same axial location but separated 90° circumferentially; and two within the primary nozzle, one just downstream of the turbine at the primary nozzle entrance, and one close to the nozzle exit plane.

This thesis, however, will report the results obtained from the two combustor probes and the two tailpipe probes only. The three other pressure probes were used to obtain data in a parallel program at the Lewis Research Center and will not be discussed here.

The actual transducers used were conventional 0.635 cm condenser microphones with pressure response cartridges. To avoid direct exposure of the microphones to the high temperature combustion gases within the core, they were mounted outside the engine and the fluctuating static pressure in the engine core was communicated to the transducers by means of a "semi-infinite" acoustic waveguide tube. As described below, this waveguide tube consists, essentially, of a very long extension of narrow tubing. The long length is required to make the tube essentially anechoic to eliminate longitudinal probe resonances (i.e., standing waves).

A drawing of a typical probe is shown in figure 7. The microphone was flush mounted in the acoustic waveguide through a support-

ing block and housed in a pressure chamber. Attached to the block were a 5/8-cm diameter sensing tube on one end and a coil of tubing of the same diameter, 30 meters long on the other. The diameter of the coil was approximately 30 cm, so the ratio of the tube radius to coil bend radius was approximately 50 to 1. This was considered sufficient to minimize the possibility of reflections from the bends in the tube.

The lowest frequency at which transverse resonances (i.e., radial or circumferential) could be expected was estimated from (ref. 29)

$$f = \frac{1.84\ \pi c}{D}$$

Where c is the speed of sound in the tube, and D is the tube diameter. For $c = 340$ m/sec, and $D = 5/8$ cm, then $f = 31.8$ kHz. This is well beyond the frequency range of interest, as will be seen.

The sensing tube of each probe was flush mounted as a static pressure tap at each of the various measuring locations within the engine core. A regulated nitrogen purge flow was maintained in each sensing line to protect the microphone from hot core gases. Since the signals from various pairs of probes were to be cross-correlated, the regulated purge flow system was separate for each probe. This eliminated the possibility of any common valve noise from the regulator contributing to the correlations. Static pressure was balanced across the microphone by means of a small vent hole connecting the pressure chamber and sensing line. Figure 8 is a

schematic of a typical core pressure probe installation.

An inescapable characteristic of such probes is the frequency response roll-off with increasing frequency due to viscous attenuation in the tube between the sensing opening and the microphone. Prior to the tests, the frequency response of the probes were determined. The amplitude and phase response were determined by comparison with a microphone identical to the one used in the probe using a symmetric placement with respect to the axis of a loudspeaker, in an anechoic room. The input to the loudspeaker was a signal from a white noise generator low pass filtered at 10 kHz.

The frequency response for a typical probe is shown in figure 9. The results indicated that the amplitude response of the probes was flat within ±2 dB from 50 to 1500 Hz. Similarly, the phase response of the probes was flat within about 5° up to 1500 Hz after accounting for the phase lag associated with the length of the sensing tube of each particular probe. Between 1500 Hz and about 3500 Hz the response was generally flat within ±4 dB and ±10°. Beyond 3500 Hz the response curves showed large distortions, and it was not clear whether these distortions were due to limitations in the calibration facility or were intrinsically related to probe construction and geometry. However, even at 1500 Hz, with the exception of the high frequency tones generated by the rotating machinery, the core noise associated with this engine was confined to a frequency range well within the acceptable response region of the probes.

A facility for probe calibration at the elevated temperatures prevailing within the core of the engine (between 810 K and 1375 K, depending upon operating conditions) was not available. Consequently, the actual response of the probes during testing cannot be documented. However, it is felt that the presence of the nitrogen purge, the primary purpose of which was to prevent a blow-by of hot gases across the microphone during engine start-up and operating transients, served to significantly cool the sensing tube. The temperature within the tube, just upstream of the microphone (see figs. 7 and 8), was monitored with a thermocouple. During engine operation the temperature did not exceed ambient by more than about 5 K.

The purging nitrogen flowing through the transmission tube can generate pseudosound as it passes across the face of the microphone. This pseudosound pressure level was measured directly with the engine off and found to be a minimum of 20 dB below the fluctuating pressure levels in the core at the highest flow rates required during testing. The nitrogen purge flow rate was monitored (see fig. 8) during engine operation for the pressure level comparison between engine on and engine off.

The probe sensing tubes and anechoic extensions were required to cross the fan flow stream when mounted on the engine. Impingement of the fan flow on the tubes, then, would induce noise within the tubes themselves, as well as radiate noise to the far-field. To minimize this flow induced noise, airfoil shaped struts attached to the cowl of the core engine and surrounding the tubes were used. A

photograph of the engine with the probes and struts in place is shown in figure 10.

3.3 Test Arena and Far-Field Microphone Array; Test Conditions

All tests were conducted at an outdoor test facility with a hard-surface (concrete) ground plane, at the NASA Lewis Research Center. The engine was suspended from the test stand with its centerline 2.9 meters above the ground plane.

The far-field microphone array consisted of sixteen 1.27 cm diameter condenser microphones placed on circular arcs centered on the pivot plane of the test stand (i.e., the plane at which the engine is suspended from the test stand). The microphones were spaced at intervals of 10° from 10° to 160°, relative to the engine inlet axis. To minimize problems associated with ground plane reflections, the microphones were mounted at ground level. Additionally, all microphones were fitted with wind screens. Because of the presence of small utility junction boxes on the ground, the radius of the rearward arc (29.9 m) was 0.6 meter less than the radius of the forward arc (30.5 m). Figure 11 is a schematic illustration of the test arena.

The simultaneous internal (i.e., core) fluctuating pressure and far-field acoustic measurements were made at eight different fan speeds at approximately equal intervals between 30 and 95 percent of maximum speed (7600 rpm). The corresponding range of combustor temperatures and primary jet exhaust velocities were from 810 K and

98 m/sec to 1375 K, and 314 m/sec. The ambient temperature during testing ranged between 0° and 13° C, and the relative humidity ranged between 50 and 70 percent. Data were not taken during periods of precipitation or when the wind velocity exceeded about 10 km/hr (5 knots).

3.4 Data Acquisition

Prior to operation, all microphones were calibrated with a pistonphone which provided a standard sound pressure level of 124 dB (referenced to 2×10^{-5} Pa) at 250 Hz. During testing, signals from all transducers were transmitted to a remote control room via shielded cable for amplification, signal conditioning, and recording.

The signals from the far-field microphones and the core fluctuating pressure probes were FM recorded on magnetic tape for later processing. The tape recorders were equipped with IRIG standard, intermediate band, group II electronics, which provide a flat frequency response to 20 kHz on both record and reproduce at a tape speed of 60 in./sec. The dynamic range available was approximately 48 dB. Two fourteen channel tape recorders were used with all seven internal probe signals recorded on each machine, with the 40° through 100° far-field signals recorded on one, and the 110° through 160° far-field signals on the other. Additionally, one channel on each machine was used for annotation. The 10°, 20°, and 30° microphone signals were not recorded simultaneously with the

remainder of the data and so could not be used for correlation purposes.

All internal fluctuating pressure signals and far-field acoustic signals were recorded in 120 second record lengths. This was initially considered sufficient to obtain high statistical confidence in the data. However, in some cases it provided only marginal confidence levels, and these will be noted later.

Engine operating conditions as well as probe temperature, pressure, and nitrogen purge flow rate were monitored and recorded on the NASA-Lewis CADDE system (Central Automatic Digital Data Encoder). On-line data processing and analysis was limited to 1/3 octave-band spectral analysis of the various pressure signals for "quick-look" purposes. Obviously anomalous data were discarded. The Lewis Research Center is immediately adjacent to Cleveland Hopkins International Airport, and occasional aircraft flyovers would require re-running a data point.

3.5 Data Processing

Virtually all of the results presented herein were obtained by off-line data processing of the taped signals on a two-channel, FFT (Fast Fourier Transform) digital signal processor, with built-in analog to digital converters and 120 dB/octave anti-aliasing filters. The processor was capable of direct computation of up to a 4096 sample ensemble average of a 1024 point forward or inverse Fourier transform to yield either single or double channel time

domain (auto or cross-correlation) or frequency domain (auto or cross-spectra, phase, transfer function, and ordinary coherence) information.

The processor also had a unique feature which permitted manual editing of stored input data prior to processing. For example, the input memory could have its contents rotated relative to a fixed memory address register. If the stored data represents a time series, then rotation represents a time translation. A Fourier transform could then be performed on the rotated data. This very useful feature enabled a previously computed cross-correlation function to be rotated in memory for time delay removal. A Fourier transform of the translated cross-correlation then produces the relative phase shift between the two correlated signals unobscured by that part of the phase shift due to time delay.

There was a slight limitation in the selection of anti-aliasing frequencies imposed by the design of the processor. To understand this limitation, a brief description of the frequency selector settings of the processor is necessary. The analyzer had available 57 front panel selectable frequency ranges, from 10 Hz full scale to 150 kHz full scale in integer steps of 1 through 15, with multipliers of 10, 100, 1000, and 10,000. These 57 frequency settings represented the 0 Hz (nominal) to full scale frequency analysis ranges available to the user. However, the anti-aliasing filters could only be activated at cutoff frequencies equal to exactly 80 percent of any one of the full scale analysis ranges (not

necessarily the range being used).

For example, if it was desired to analyze data in a frequency range of 0 to 400 Hz, then the anti-aliasing frequency could be selected at precisely 400 Hz since 400 Hz is 80 percent of 500 Hz, and 500 Hz was a selectable frequency range. However, if it was desired to analyze data in a frequency range of, say, 0 to 1000 Hz, it was not possible to select an anti-aliasing frequency of exactly 1000 Hz since this would have required a frequency range setting of 1250 Hz to be available, which it wasn't. Hence, in this case, an anti-aliasing frequency of 1040 Hz would be required since 1300 Hz as a frequency selection was available. Consequently some of the data contains small aliasing errors due to this characteristic of the analyzer. This is considered to be a relatively small compromise in return for the avoidance of using external filtering with lower roll-off rates, and the possible introduction of small phase shifts due to mismatched filters. At any rate, in all the data to be presented, both the frequency range of analysis as well as the anti-aliasing frequency selected will be specified.

Another limitation in the processor, this one somewhat more serious than above, concerns the computation of coherence functions between signal pairs. In the usual analysis of signal pairs, the similarities or mutual properties between the two signals do not coincide with one another until some time delay has elapsed. If this time delay is on the order of the sampling period which is being used for analysis, this will lead to a low estimate of the

true coherence function. In a fixed point analysis, however, the sampling period is related directly to the frequency analysis range and is not independently controllable.

The following illustrative example will serve to clarify this point. The signal processor used to analyze the data in this investigation digitizes each time record into 1024 words at a sampling rate of 2.048 times the highest frequency selected (i.e., the maximum frequency in the range selected. Note that this is slightly in excess of the Nyquist sampling criterion). Hence

$$f_{sample} = 2.048\ f_m$$

where f_m is the maximum frequency to be resolved.

The memory period, or sample record length, therefore is:

$$T = \frac{\text{Number of words/record}}{\text{Number of words/sec}}$$

$$= 1024/(2.048\ f_m) = 500/f_m \text{ sec/record}$$

If, for example, frequency information to 10,000 Hz is required, then $f_m = 10{,}000$, and $T = 500/10{,}000 = 0.05$ seconds. If the natural time delay between the two signals being analyzed is on the order of 0.05 second or greater, than a significant bias error is introduced into the measured, or estimated coherence functions, with the estimate being low (30).

The required procedure to eliminate this bias error is to introduce a pre-computation delay (i.e., sample and hold) in the signal which occurs earlier in time, thus waiting for the second signal to "catch up" before implementing any computations. The

processor had such a precomputation delay feature when computing cross-correlations and cross spectra, but not when computing coherence functions. This did not present any problems when computing coherence functions between pressures within the engine, since the natural time delays were relatively short in comparison with the processor memory periods. In any event, the in engine results were used for diagnostic purposes only.

Between the engine and the far-field, where separations of approximately 30 meters and 90 msec prevails, however, the time delays were a significant fraction of the processor memory period for frequency analysis ranges above about 500 Hz. Furthermore, it was between the engine and the far-field that the numerical value of the coherence was required for computing far-field combustor spectra, directivity and power levels. For all cases where the numerical value of the coherence was used for computations the bias correction due to time delay was calculated, and its effect on the resulting computation noted.

Finally, it should be pointed out that the somewhat less than flat response of the waveguide probes do not affect the quantitative results to be shown in Chapter 5. The normalized nature of the coherence function is such as to cancel the effect of probe response (as long as the response is linear). All measurement errors, therefore, are determined by the microphone response themselves, which generally are accurate to better than ± 1 dB.

4. INDENTIFICATION OF COMBUSTION NOISE

4.1 Correlations Between Internal Pressure

This chapter discusses the results of the diagnostics conducted in the present investigation to identify combustion noise in the YF-102 turbofan engine. We begin by noting that when conducting fluctuating measurements in a turbulent fluid for purposes of obtaining direct acoustic information, the investigator is normally confronted with a significant problem in interpreting his data. There is no straightforward way of distinguishing between that part of the pressure signal which is acoustic information, and that part which is due to hydrodynamic pressure fluctuations arising from local or convecting turbulence.

In general, however, the convection speeds of turbulence within an engine are much less than the local speed of sound. This leads to the idea of cross-correlating the pressures at two separate points within the engine and examining the time delay. If the pressure signal is entirely due to convecting turbulence, then the cross-correlation will be a positively peaked, even function with respect to a time delay corresponding to the convection speed. If the pressure signal is due entirely to a propagating acoustic-wave, then the cross-correlation will have similar properties with

respect to a time delay corresponding to the acoustic propagation speed (augmented or diminished by the speed of the flow, depending on direction).

If the pressure signal is due to both acoustic waves and convecting turbulence then the cross-correlation should show two positive peaks, with each peak occurring at the appropriate time delay, as described above. For this case, digital computational techniques have been developed which utilize the symmetry properties of correlation functions to separate the acoustic contributions to the correlation from the contribution due to convecting turbulence (ref. 31). This may then be Fourier transformed to obtain the acoustic spectrum. It is not necessary to remove the time delay, since time delay produces phase shifts only, and does not alter the spectral shape. (It should be noted that this technique requires the acoustic information to be uncoupled from the turbulence. If the two are not independent, then their individual cross-correlations are not separable in this manner. In aerodynamic noise problems, of course, the acoustics are very often coupled to the turbulence.)

With the objective of characterizing the internal fluctuating pressures in the tailpipe of the YF-102, these two pressure signals (see fig. 6) were cross-correlated. The normalized result is shown in figure 12[1]. The correlation was obtained at a fan speed of

---

[1]All correlation data to be shown in this chapter will have the following notation shown on the figures: The anti-aliasing filter cutoff frequency, f_c; the number of disjoint (i.e., independent)

43 percent of maximum, which is near flight idle conditions, but below approach conditions. Both signals were low-pass filtered at 1600 Hz with the anti-aliasing filters of the digital signal processor (DSP). This cutoff frequency was chosen as the approximate upper limit of the acceptable response range of the probes. As will be shown shortly, this is not a significant limitation since the combustion noise for this engine is confined to low frequencies.

The correlation was normalized with respect to the zero time delay values of the individual auto-correlations (i.e., the individual rms values within the 1600 Hz passband). The signals correlate rather strongly at a positive delay time of 0.54 msec. The separation between the two tailpipe probes was 0.34 m. Consequently, considering the gas temperature within the nozzle ($\sim$670 K) and the flow velocity ($\sim$90 m/sec) for this case, the calculated time for an acoustic wave to travel between the two probes is about 0.56 msec. At the speed of the flow, the corresponding convection time would be about 3.8 msec.

This close agreement between the measured delay time and the calculated acoustic delay time must be considered fortuitous. Although, as indicated earlier in Chapter 3, the temperatures in the probe sensing tubes were monitored and were within about 10 K of

---

samples used for ensemble averaging, N, and the digitizing time increment, $\Delta\tau$. Additionally, frequency domain data will have the following notation on the data-figures: Upper frequency of analysis range, f_m; anti-aliasing frequency, f_c; number of disjoint samples for the ensemble average, N; resolution bandwidth, Δf. Correlation data contain 1024 points. Frequency domain data contain 512 amplitude or 512 phase points.

ambient, some temperature gradients near the open end of the tubes must exist. These temperature gradients could introduce some small relative phase shifts between probes. Any such phase shifts, in turn, would show up as time delay between the signals. For the small measured time delays between signals within the engine, then, conclusions regarding the actual speed of the signals are somewhat speculative. Nevertheless, this correlation appears to be evenly symmetric with a positive peak about the acoustic delay time, and the preliminary evidence suggests, that the two pressure probes are detecting an acoustic signal.

Before proceeding with additional results, two points should be made regarding the above conclusion. First, under certain conditions a cross-correlation which has a single peak at a delay time which corresponds to the speed of some identifiable phenomenon, and which meets the symmetry conditions discussed above, does not ensure that that phenomenon alone is, in fact, being measured. The width of the main lobe in the correlation of a broadband random signal is approximately equal to $1/B_w$, where B_w is the bandwidth of the signal (26). Clearly then, unless the difference in time delays being investigated is substantially greater than $1/B_w$, the two separate peaks may not be distinguishable, due to finite signal bandwidth. In the present case the two time delays being investigated differ by about 3.2 msec, which is approximately five times the reciprocal of the signal bandwidth. A second peak should be clearly distinguishable if it were present.

More important is the fact that if the upstream acoustic signal was contaminated by turbulence which decayed before reaching the downstream probe (the signal at which may or may not be contaminated), the resulting correlation would still show a single peak. The conclusion, then, that the pressure signal within the nozzle is a purely acoustic signal can only be tentative. The issue of turbulence contamination on the various pressure signals will be discussed later in this chapter.

Returning to the results, if it is assumed that the nozzle pressure is related to an acoustic wave traveling in the downstream direction, then it is natural to examine the pressures upstream of this region to determine the origin of this acoustic information. The next upstream probe location is the combustor. The two combustor probes, 90° apart circumferentially but at the same axial location, were flush mounted in the combustor liner downstream of the igniter in the region near where the combustion process is completed (see fig. 6).

The normalized cross correlations between the pressure at the in-line combustor probe location and the pressure at each of the two tailpipe positions for the same engine conditions as figure 12, are shown in figures 13(a) and (b). These correlations are seen to be significantly different from that of figure 11. They contain both positive and negative multiple peaks and are more complexly shaped than the cross-correlation shown in figure 12. They clearly do not have, for example, the symmetry and maxima

properties associated with pure propagation or convection (i.e., just time delay).

This result can be clarified considerably by examining the frequency domain information between these pairs of pressure signals.

4.2 Pressure Coherence

The tool which is used here to aid in interpreting these correlations is the ordinary coherence function. The ordinary coherence function is completely analogous to the cross-correlation function, with the information being presented in the frequency domain. It is essentially a normalized cross-spectrum and is defined for random signals as (26):

$$\gamma^2_{ab}(f) = \frac{|G_{ab}(j\omega)|^2}{G_{aa}(\omega)G_{bb}(\omega)} \qquad \omega = 2\pi f;\ j = \sqrt{-1} \tag{29}$$

where $|G_{ab}(j\omega)|^2$ is the square of the ensemble averaged cross-spectral density between a and b; and $G_{aa}(\omega)$ and $G_{bb}(\omega)$ are the averaged autospectral densities at a and b, respectively.

The coherence function must have a value between zero and one, with high (low) coherence at a particular frequency, f, meaning high (low) correlation at that frequency. Of course, here time domain information has been traded for frequency domain information. Subject to certain limitations, the coherence function may also be used to compute quantitative contributions between a source region and a field point. These limitations, and the results of such com-

putations will be presented in the next chapter.

The measured coherence function between the pressure at the in-line combustor station and the pressure at the upstream nozzle station is shown in figure 14. There are three very distinct and separate regions of coherence: one between zero and 250 Hz; another between about 350 Hz and 650 Hz; and a third between about 750 Hz and 950 Hz. The issue of the numerical value of the coherence will be dealt with in the next chapter. Here we are concerned only with the fact that there are three separate spectral regions where the fluctuating pressure in the combustor is coherent with the pressure in the upstream region of the tailpipe.

Particular attention should be paid to the second of these three regions, between about 350 Hz and 650 Hz. This is precisely the region where numerous investigators (refs. 13 to 19, for example) have found the spectral range of core noise to lie. This frequency range has been the demonstrated concern among most investigators of core noise. In fact, at least one of the more widely used prediction schemes considers the spectral peak of core noise to occur at a fixed frequency of 400 Hz, independent of engine geometry or operating conditions (32).

In figure 15, however, which shows the measured coherence between the fluctuating pressure in the combustor and the pressure at the downstream tailpipe station, this central region of coherence has diminished significantly, while the low frequency region of coherence is still clearly present. The highest frequency region of

coherence has vanished completely.

Similarly, figure 16 shows the measured coherence function between the fluctuating pressure in the combustor and the far-field acoustic pressure, at the 120° microphone. This microphone location was selected since data taken by other investigators using more conventional methods appear to indicate that the angle of peak core noise occurs near 120° (see ref. 32, for example). This would improve the likelihood of obtaining a relatively strong coherent relationship between the two measuring stations if the core noise had a significant combustor related component. As can be seen from the figure, the coherence between the combustor pressure and the far-field acoustic pressure is restricted entirely to the same low frequency regions of coherence (0-250 Hz) which prevailed between pressures within the engine.

This result indicates, then, that insofar as combustor associated noise is of interest, the regions of fluctuating pressure coherence above about 350 Hz which are seen in figures 14 and 15 are not associated with sound, or with a linear sound producing or propagating mechanism. Alternatively, as shown in figure 16, if these pressure coherence regions are associated with sound, the energy contained in those spectral regions is not radiating outside the engine. Consequently, for purposes of examining combustor related far-field noise in this engine, attention can be limited entirely to the frequency range below about 250 Hz, which clearly is radiating to the far-field.

4.3 Phase and Amplitude Relations

It is now of interest to reexamine the cross-correlation shown in figure 13(a), allowing the coherence result shown in figure 16 to serve as a guide for filtering the data. The unnormalized filtered cross-correlations between the combustor fluctuating pressure and the nozzle fluctuating pressures (i.e., the filtered versions of figs. 13(a) and (b), respectively) are shown in figure 17. All signals have been low-pass filtered at 240 Hz, the frequency at which figure 16 indicates there is no combustor related far-field sound. The correlations were not normalized since their magnitudes are not important to the present discussion.

As can be seen, these cross-correlations are much better characterized than the broadband versions shown in figure 13. They have clearly defined negative peaks evenly symmetric about delay times of about 5.1 msec in figure 17(a) and 5.7 msec in figure 17(b)[2]. This, of course, is one of the characteristics suggested in the discussion in Chapter 2 which is expected to prevail between the pressure in a combustion noise source region and the acoustic pressure outside such a source region. The difference in these two delay times of 0.6 msec corresponds very closely to the measured acoustic delay time of figure 12, as would also be expected.

---

[2]This kind of precision is obviously not obtainable from the figures, which were drawn on an x-y plotter driven by the DSP. The result was obtained by direct digital readout of the output memory of the DSP.

No conclusions regarding the absolute delay times, however, can be made. The flow path between the combustor probe and the upstream tailpipe probe is exceedingly complex as can be seen from figures 4 and 6. Furthermore, neither the temperature distribution nor flow velocities throughout this region were known. Consequently, whether the observed 5 msec delay time corresponds to an acoustic propagation time or a turbulent convection time is not at this point, obvious. In either case, however, because of the negative peaks, these correlation functions cannot be associated with pure time delay. This reasoning is based on the notion that if only pure time delay prevails between two signals then the cross-correlation should be shaped like the autocorrelation, which must have a positive peak, translated in time.

The nature of the relationship between the combustor and tailpipe pressures in this low frequency range of combustor associated far-field noise can be further explored by examining the relative phase difference between the two signals. The phase shift between combustor and upstream tailpipe pressures, as measured directly with the DSP, is shown in figure 18, for the signals low pass filtered at 240 Hz. The plot shows a phase shift between the two signals which is linear with frequency, and which is characteristic of the phase relationship between two signals with time delay between them.

The shape of a cross-correlation function is entirely determined by the amplitude relationship between the two signals and by

that part of the phase relationship which is not due to time delay. Time delay causes a phase shift which is linear with frequency and which serves only to translate the correlation function. What is desired, in this case, is the phase difference unobscured by time delay.

This zero time delay phase shift corresponding to figure 18 was obtained by removing the time delay associated with the filtered correlation function between combustor and upstream tailpipe pressure (fig. 17(a)) via the editing feature of the DSP described in Chapter 3 and Fourier transforming the translated correlation. The real and imaginary parts were then combined in polar form to produce the desired phase information (as well as the amplitude of the cross spectrum). However, there are some subtle, but important, features associated with such an operation.

The correlations which have been presented to this point have been computed by low pass filtering the signals at some appropriate frequency but sampling at a much higher frequency. For example, figure 18 was obtained by filtering the data at 240 Hz but selecting an analysis range of f_m = 7000 Hz. Since the memory period for this DSP is $500/f_m$ the equivalent time scale for the resulting cross-correlation is 500/7000 Hz = 71.4 msec. Hence each of the 1024 points in the correlation represents a time interval of 0.0698 msec. Sampling the data at a frequency much higher than the filter frequency, as in this case, has the effect of expanding the time scale and presenting the correlation function in great detail, so

that any symmetry properties can be easily observed and the time delay precisely located.

However, since the DSP uses a fixed number of points (1024) in performing an FFT on the data, if this expanded correlation is Fourier transformed, the 240 Hz information would be compressed in the frequency domain. This compression factor would be, in this case, 240 Hz/7000 Hz = 0.0342, so only about 3.4 percent of the resulting information would be useable, or 17 phase points (and 17 amplitude points). This makes the data difficult to interpret and also increases the effective resolution bandwidth with the possible introduction of bias errors. Consequently, the correlation function must be recomputed at a lower sampling rate, and then edited (i.e., rotated in memory) to remove the time delay.

The result of this computation at a lower sampling rate (but still low-pass filtered at 240 Hz) for the combustor to upstream correlation function is shown in figure 19. Comparing this with figure 17(a), it is clear that now the time domain information has been compressed with some loss of detail. However, the symmetry properties which suggested that it is the time delay to the negative peak which is relevant, as well as the value of the time delay was obtained from figure 17(a). This compressed correlation was computed using an analysis range of 1000 Hz, so now the compression factor is 240/1000 = 0.24. Now if the time delay to the negative peak is removed and the result Fourier transformed, some 24 percent of the resulting frequency domain information will be useable.

The phase shift obtained by translating the negative peak of the correlation in figure 19 to zero time delay, and Fourier transforming is shown in figure 20. It is seen here, that with time delay removed, the phase shift between combustor pressure and upstream tailpipe pressure is essentially 180°, independent of frequency, for the 240 Hz low pass band of interest.

The relative amplitude relationship between the combustor pressure and the upstream tailpipe pressure can be obtained via the transfer function. The relative amplitude of the measured transfer function (not the cross spectrum) between these two pressure, computed directly by the DSP is shown in figure 21. In the present context, this transfer function is defined as the ratio of the cross-spectrum between the two pressures, normalized with respect to the auto-spectrum of the upstream pressure. That is, it is precisely the transfer function of equation (25). Comparing the result with the dashed line sketched on the figure, it is seen that the transfer function between combustor pressure and upstream tailpipe pressure varies approximately as the square of the frequency (6 dB/octave), over most of the range of interest.

A least squares linear curve fit of the transfer function shown in figure 21 between 10 and 150 Hz yielded an actual frequency exponent of 1.7 (∿5.2 dB/octave). There are several possible reasons why an exponent of precisely 2.0 was not obtained, but the most likely is the presence of some "scrubbing" noise within this frequency range. As discussed earlier, scrubbing, or

surface interaction, noise would be characterized by a transfer function proportional to frequency to the first power. A small amount of scrubbing noise, then, would serve to reduce the combustion noise frequency exponent somewhat. In fact, all of the transfer functions to be shown between the combustor pressure and downstream pressures, including far-field, have actual frequency exponents somewhat less than 2.0. However, all of the corresponding cross-correlations and time delay removed phase shifts to be shown between combustor and tailpipe pressures and between combustor and far-field pressures exhibit the symmetry properties and 180° phase shift, respectively, as discussed earlier for combustion noise.

Beyond about 150 Hz, figure 21 shows a sharp decrease in the transfer function. Similar behavior in all the transfer functions measured with respect to the combustor pressure was observed, as will be seen shortly. This would indicate an attenuation mechanism downstream of the combustor strongly dependent on frequency, and beginning near 150 Hz. Such a result was reported in reference 12 at frequencies only slightly higher than the 150 Hz shown here, and was attributed to turbine attenuation. It is concluded, therefore, that although an exact frequency squared relationship is not observed in figure 21, there is adequate evidence to support the contention that the dominant behavior is consistent with equation (24) for the combustor as an acoustic source region.

Similar measurements were made to obtain the phase and ampli-

tude relationships between the combustor pressure and the downstream tailpipe pressure. The broadband cross-correlation was shown in figure 13(b). The filtered cross-correlation over the 240 Hz low pass band of interest was shown in figure 17(b). The phase, before time delay removal, as obtained by direct measurement on the DSP is shown in figure 22(a). Again we see a phase shift linearly proportional to frequency. The phase shift after time delay removal, obtained by Fourier transforming the compressed correlation function (not shown) is shown in figure 22(b), and here we also see a phase shift of 180°, essentially independent of frequency, over most of the frequency range of interest. Finally, the magnitude of transfer function between the combustor pressure and the downstream tailpipe pressure was also measured with the DSP and this is shown in figure 23. The result, once more, is a relative amplitude difference approximately proportional to frequency squared.

At this point, it is worth summarizing the results obtained so far. It has been shown by coherence measurements that the fluctuating pressure in the combustor correlated with the pressures in the tailpipe over several distinct spectral ranges. However, the coherence between the fluctuating combustor pressure and the far-field acoustic pressure is restricted entirely to a single region below about 250 Hz, and peaking near 125 Hz. That is, only the low frequency range of the fluctuating combustor pressure is related to far field noise, the subject of interest.

Using this result as a guide, filtered cross-correlation functions between the combustor pressure and the tailpipe pressures have been measured. These filtered correlation functions exhibit the property of being evenly symmetric about negative peaks and hence cannot be associated with pure time delay (either acoustic or convective). The time delays to these negative peaks were removed and Fourier transforms of the translated correlations computed, to obtain that part of the phase shift not due to time delay. The results indicated, in both cases, a 180° phase shift, independent of frequency. Similarly, the transfer functions between the combustor pressure and tailpipe pressures were measured, and their magnitudes were proportional to frequency squared.

What we have seen, then, is that in the range of frequencies where the fluctuating combustor pressure is related to far-field noise, the tailpipe pressures behave approximately as the second time derivative of the combustor pressure.

In a similar manner, we can now show that in this frequency range (0-240 Hz), pure propagation exists within the tailpipe. The broadband (0-1600 Hz) cross-correlation between the fluctuating pressures at the two tailpipe stations was shown in figure 12. The low pass filtered version of this correlation is shown in figure 24. Here the even symmetry properties with respect to a positive peak at a delay time corresponding to the acoustic delay prevails.

The compressed version of this correlation was translated to remove this time delay and then Fourier transformed on the DSP. The phase part of the result, shown in figure 25, exhibits essentially a zero degree phase shift, independent of frequency. (The "spike" is sixty cycle noise.) The amplitude of the transfer function between these two pressures, as measured directly by the DSP is shown in figure 26, for the low frequency range of interest. In contrast to the frequency squared relation which exists between the combustor pressure and the tailpipe pressures, here the amplitude of the transfer function is flat and relatively independent of frequency. These two properties, zero degree phase shift (after time delay removal) and flat transfer function, combined with a delay in the time domain corresponding to acoustic propagation, indicate pure acoustic propagation.

We can now complete the picture by examining the phase and amplitude relationships between the combustor pressure and the far-field acoustic pressure, and between the tailpipe pressures and the far-field acoustic pressure. The corresponding low-pass cross-correlations, phase shifts with and without time delays, and transfer function amplitudes are shown in figures 27 through 35.

The combustor to far-field relations (for the 120° far-field angle) are shown in figures 27 through 29 and here we see a 180° phase shift (fig. 28(b)), frequency squared relationship (fig. 29). The far-field acoustic pressure, then, is also

behaving as the second time derivative of the fluctuating pressure in the combustor. The upstream tailpipe to far-field relations and the downstream tailpipe to far-field relations are shown in figures 30 to 32 and 33 to 35, respectively. In both cases, a zero degree phase shift and flat amplitude transfer function prevail, and these are indicative of pure time delay.

The picture which emerges then, is the following: For the frequency range where the far-field acoustic pressure is coherent with the fluctuating combustor pressure, the far-field acoustic pressure, as well as the pressures within the tailpipe, behave as the second time derivative of the combustor pressure. This behavior is consistent with a combustion noise generating mechanism wherein the fluctuating pressure due to entropy fluctuations acts as a source for acoustic energy, as discussed in Chapter 2. Within the tailpipe and between the tailpipe and far-field, for the same low frequency range, the evidence indicates pure acoustic propagation. The nozzle, then, is acting as a transmission line for the acoustic energy generated in the combustor, at least for frequencies up to about 250 Hz.

4.4 Variation of Data with Engine Operating Conditions and Far-Field Microphone Data

The results presented so far in this chapter have been limited entirely to an engine operating speed of 43 percent of maximum, and a far-field microphone angle of 120°. These data, however, are typical of the results obtained at all microphone angles (40°

through 160°) and at operating speeds from 30 percent (less than ground idle conditions) through 60 percent (approach conditions) of maximum fan speed. The conclusion, therefore, that there is a measurable contribution to overall engine noise from the combustor holds true throughout the forward and rearward arcs of the engine, and for a substantial portion of the static operating conditions. The spectral range of this contribution, with only minor variations, peaks near 125 Hz and is limited entirely to frequencies below about 250 Hz.

For the purpose of presenting supporting evidence for this, the results for the pair-wise relations between combustor pressure and far-field acoustic pressure at a forward arc angle of 60° are shown in figures 36 through 38. The coherence function, amplitude transfer function, and time delay removed phase shift are contained in figures 36, 37, and 38, respectively. The coherence, though not as strong as at the 120° microphone is seen to be limited to frequencies below 250 Hz, although the spectral peak is not as distinct. This coherence function is shown in appendix C to produce an unusual directivity pattern for combustion noise at certain frequencies. Unfortunately, as is shown in appendix A, its reduced numerical value at some frequencies decreases the statistical confidence in the data and establishes a relative broad uncertainty band in the resulting coherence spectrum. Figure 37 shows a transfer function which, although not as clean as those shown earlier, still exhibits a frequency squared behavior. Finally, the time

delay removed phase shift, figure 38, indicates a phase shift of approximately 180°, over the frequency range of interest. Here again, however, the result is not as clean as at the 120° angle, but the trend is obvious. All these results at the 60° (forward arc) far-field angle, are for the same operating conditions as earlier in this chapter: 43 percent of maximum speed.

Figures 39 to 42 show similar results between combustor and far-field at a different operating condition, 30 percent speed, but at the same rearward arc position of 120° shown earlier. The coherence, amplitude transfer function, and zero time delay phase shift are depicted in figures 39, 40, and 41, respectively[3]. The coherence result shows essentially the same low frequency correlating region seen in the previous two sets of data.

The amplitude transfer function (fig. 40) again shows a frequency squared behavior, and the zero-time delay phase shift (fig. 41) is near 180° at all frequencies within the range of interest.

4.5 Discussion of the Diagnostic Results

As indicated earlier, most previous investigators studying core noise have found the dominant spectral peak to occur in the range of 400 to 500 Hz. The present investigation indicates a lack of any coherent relationship between combustor pressure and far-field

---

[3]The tone at 380 Hz in fig. 39 was also observed in the combustor pressure spectrum and at almost all far-field microphones. It only occurred at 30 percent engine speed, which is an off-design operating point.

acoustic pressure beyond about 250 Hz. Some question arises, therefore, as to the validity of the coherence measurements.

Reference 18, for example, presents the results of coherence measurements between the pressure measured in a gas turbine combustor installed in a specially designed test apparatus (i.e., non-engine installation) and far-field acoustic pressure. The authors distinguish between acoustic pressures in the combustor and non-propagating hydrodynamic pressure fluctuations (i.e., pseudosound). It is then pointed out that the presence of this pseudosound would serve to reduce the pressure coherence between the combustor and the acoustic far-field. The conclusion in reference 18 is that this reduced coherence is not necessarily indicative of a correspondingly reduced combustion noise contribution to the far-field. Based on these results, therefore, it may be argued that this pseudosound "contamination" is responsible for the lack of any pressure coherence between combustor and far-field beyond 250 Hz.

It is the view of the present author, however, that in a source region this distinction between acoustic pressures and non-acoustic pressures loses its meaning. In the present work the causal relationships between the fluctuating pressure in the source region and the acoustic far-field are being investigated. As such, we are interested in the entire pressure field in the combustor, whatever its nature, and not just those pressures which can be specifically identified as being locally acoustic in their character. The issue of turbulence "contamination" in the combustor pressure mea-

surement, therefore, is not meaningful in the present context.

The strongest supporting evidence for the spectral results reported in this chapter may be found in reference 33. Here the authors reported the results of a combustion noise investigation by far-field acoustic measurements alone conducted on a small aircraft auxiliary power unit (APU). The APU is basically a small gas turbine engine used for auxiliary power generation while the aircraft is on the ground. As such, there is no fan or convergent nozzle to generate additional noise.

The results reported in this reference, with the turbine removed, clearly indicate a combustion noise peak at 125 Hz. Furthermore, at 250 Hz the measured sound power level is down approximately 10 dB.[4] This is consistent with the results to be shown in the next chapter, where the combustor-associated far-field power level spectra are presented.

Finally, the authors of reference 33 indicate that this peak frequency remained fixed for all combustors tested in the small gas turbine class, even the reverse flow configurations such as investigated here. It will be recalled from the description of the YF-102 in Chapter 3, that the core of this engine is basically a small gas

---

[4]The data in ref. 33 are reported in full octave bands, and the actual results show about a 7 dB reduction in combustor sound power between 125 and 250 Hz. The data reported herein is for constant bandwidths. The conversion from proportional bandwidth data to constant bandwidth data can easily be accomplished by subtracting 10 dB/octave ($\sim$3 dB/octave) from the proportional bandwidth data. This conversion holds regardless of the precise width of the constant bandwidth data.

turbine in comparison with the cores of the turbofan engines in commercial service, and on which much of the combustion noise testing has been done. It would appear, then, that viewed with respect to the results reported in reference 33, the present results are relatively consistent.

The results of reference 33 also prove useful in interpreting a portion of the diagnostic measurements which have not been presented yet. In the previous sections of this chapter, all the coherence results reported were with respect to the combustor pressure. Pressure coherence measurements were also made, however, between each of the tailpipe measuring stations, as well as between the tailpipe stations and the acoustic far-field. The results are shown in figures 42 to 44. Figure 42 shows the pressure coherence between the two tailpipe stations. Figures 43 and 44 show the coherence between the upstream tailpipe station and the 120° far-field microphone, and between the downstream tailpipe station and the 120° far-field microphone. These data are for an engine speed of 43 percent of maximum, as before.

These data show the same region of relatively high coherence in the 0 to 250 Hz region as prevailed with respect to the combustor. Now, however, there are additional broad regions of lower, but not insignificant, coherence at frequencies up to about 1 kHz. An attempt was made to analyze these higher frequencies regions with the same technique as was used for the low frequency combustor associated noise. No simple result, however, emerged.

Figure 45(a), for example, shows the 250 to 1000 Hz band-pass filtered correlation between the downstream tailpipe pressure and the 120° far-field microphone. The correlation is seen to oscillate rather strongly at a delay time of about 87 msec, the acoustic travel time between the engine and the far-field microphone. Some of this oscillation, or "ringing" is characteristic of the correlation functions of band-pass random signals and gets worse as the pass band narrows, or the center frequency increases (26). To some extent, then, it is an unavoidable result of the filtering process. The result, however, is that it is extremely difficult to determine which peak (positive or negative), or which zero crossing corresponds to the delay time between the two signals.

As described earlier, to obtain the zero time delay phase shift by Fourier transforming a translated cross-correlation function, it was necessary to recompute the correlation at a slower sampling rate. This is necessary to increase the percentage of useful points in the resulting frequency domain representation, and to decrease the resolution bandwidth to minimize bias error. This correlation compression, of course, produces reduced time domain resolution.

The result of recomputing this correlation at a slower sampling rate is shown in figure 45(b). Clearly, a substantial amount of detail has been lost. The DSP used in this investigation permitted continual visual monitoring of the phase roll on a CRT while this correlation was translated in time and Fourier transformed. No identifiable phase information was found through a complete rota-

tion of this correlation. In a similar manner, the transfer function in this pass band did not exhibit any simple properties which could be identified with either pure time delay (flat), surface interaction noise (proportional to frequency), or combustor related noise (proportional to frequency squared).

Nevertheless, figures 43 and 44 demonstrate that a broad range of frequencies beyond 250 Hz is propagational and is contributing to overall engine noise. Alternatively, these higher frequency regions of pressure coherence within the tailpipe and between tailpipe and far-field could result from external noise, especially jet noise, propagating back into the tailpipe. This may be ruled out in view of figure 12, which shows the correlation between the two tailpipe stations to have a single, positive peak, indicating downstream travel only.

The results reported in reference 33 suggest a possible explanation. In addition to reporting data on the APU without the turbine, the authors also show data with the turbine installed. For this case, there is an additional region of core noise extending to beyond 1 kHz.[5] The additional acoustic energy must, then have the

---

[5]As shown in ref. 33, this added noise with the turbine in place extends to about 10 kHz. The data is shown in full octave bands. The high frequency information, say beyond several kHz, is likely associated with the rotational speeds of the turbine. It does not show up as sharp peaks, or tones, because of the very wide bandwidth (approximately 2800 Hz at a center frequency of 4 kHz) of an octave analysis. In the region we are concerned with, less than 1 kHz, the data in ref. 33 are either flat or increasing slowly. This would correspond to a flat or slowly decreasing spectrum for the constant bandwidth analysis used here.

turbine as its source, and this appears likely in the present case. Whether it is a result of surface interaction as the gases flow across the turbine surfaces, or the so-called "indirect" combustion noise (see ref. 34, for example) caused by entropy spots convecting through the turbine expansion passages is not evident. Nevertheless, it may certainly be classified as core noise. However, the emphasis in the present study is on direct combustion noise, and it will not be further investigated.

An additional point for discussion involves the possibility that at least some of the combustor-associated noise results from the interaction of the very turbulent combustion gases with the surfaces of the combustor. The actual surface geometry of a combustor is rather complex with numerous holes for the admission of compressor discharge air, and the promotion of more efficient combustion. In many studies of gas turbine combustion noise, baseline tests are conducted in which heated or unheated air is passed through the combustor, but without the addition of fuel, so that no combustion actually occurs. The mass flow rates used are normally the same as would exist with combustion, and these types of tests are generally performed in specially designed test apparatus (i.e., no engine).

These tests are normally conducted to determine that part of combustion noise which is flow-related only; that is, scrubbing noise. As shown in reference 25, however, and briefly described in Chapter 2, if the flow passes over a finite surface (i.e., one with a leading or trailing edge), the correlation between source pressure

and far-field acoustic pressure should have an anti-symmetric shape. It should be an odd function, and the associated phase and amplitude relations should be first derivative in nature: 90° phase shift and transfer function amplitude linearly proportional to frequency. The results shown here do not exhibit these properties. Consequently, it must be concluded that any scrubbing noise when actual combustion is present is negligible compared to the noise directly associated with combustion.

The final remarks to be made in this chapter address the issue of a very important requirement for proper interpretation of correlation and coherence measurements, and the meaningfulness of a transfer function: the system being studied with these random data analysis techniques must be linear. This, of course, has been an implicit assumption in all that has preceded. If the acoustic propagation mechanism between any pair of points being investigated is non-linear, then the interpretation of the measured transfer functions is, at very least, questionable. Furthermore, non-linear propagation would certainly serve to reduce the value of the coherence between pressure measurements. This may be advanced as a possible reason for the virtual vanishing of any pressure coherence between the combustor and far-field acoustics beyond 250 Hz.

It is likely that if a nonlinear propagating mechanism were present, it would result from high pressure levels present in the combustor. The spectrum of the fluctuating combustor pressure up to 1 kHz, at 43 percent operating speed, is shown in figure 46. The

level at 250 Hz, where the coherence has essentially gone to zero (see fig. 16) is about 118 dB (approximately 0.0023 psi, rms). This is certainly not excessively high, even by acoustic standards. It does not seem reasonable that this pressure level is sufficiently high to result in such predominantly non-linear propagation as to decorrelate the pressure signals. Nevertheless, without a detailed knowledge of the precise propagation mechanism the presence of non-linear effects must be admitted as at least being possible. In view of the previously cited evidence from reference 33, however, the assumption of negligible nonlinear effects is still felt to be valid.

5. MEASUREMENT OF COMBUSTION NOISE

5.1 Introduction

The previous chapter described the results of a series of diagnostic pressure measurements conducted on an AVCO-Lycoming YF-102 turbofan engine. The measured ordinary coherence functions between the fluctuating pressures at several locations within the core of the YF-102 and between these pressures and the acoustic pressures in the far-field were used only as a frequency domain guide for measuring filtered cross-correlation functions. The shapes of these filtered correlation functions were then used to make a qualitative judgement that the local fluctuating combustor pressures were acting as sources for low frequency acoustic waves propagating through the tailpipe and out to the far-field. The phase and amplitude information obtained from the appropriate Fourier transforms of these correlations were shown to be consistent with these conclusions. In this chapter, the ordinary coherence function will be used to obtain quantitative results on the far-field acoustic contribution of combustor generated noise.

At any given frequency, for the idealized case of a perfectly linear system with one noise-free input and one noise-free output, the ordinary coherence function between input and output has a value of unity. Conversely, if the input and the output of the system are

completely unrelated, then the ordinary coherence function must have a value of zero. The ordinary coherence function may have a value between zero and one if one or more of the following three cases exist (26):

(a) Contaminating (i.e., noncorrelating) "noise" is present in the measurements of input or output.

(b) The output is due to inputs other than, or in addition to, the input being measured.

(c) The system relating the output to the input is nonlinear.

In the present context, the fluctuating pressure in the combustor is considered to be the "input" and the far-field acoustic pressure is considered as the "output." The "system" is the generating mechanism and propagation path between the combustor and the far-field microphones, including any path within the engine through which the pressure signal travels. It has been assumed throughout the present investigation that this system is, in fact, linear. A brief argument supporting this view was presented in the previous chapter. It was also argued that the "pseudosound" pressures within the combustor could not be considered as a signal contaminant when investigating casual relations with the combustor as a source region. On this basis, then, the value of the ordinary coherence function may be considered a measure of the far field acoustic energy which is due to the fluctuating pressure within the combustor. Conversely, the quantity one minus the coherence function is a measure of the acoustic energy not due to the fluctuating combustor pressure. It must, therefore, be a measure of the far-field noise due to "inputs" such

as fan noise, jet noise, and other internal noise sources which do not correlate with the fluctuating combustor pressure. In equation form, then:

$$C(f) = \gamma^2_{CF}(f)G_{FF}(f) \qquad f = \text{frequency} \qquad (30)$$

Here, C(f) is the combustor coherence spectrum; that is, it is that portion of the far-field spectrum which is combustor related, and is therefore the combustion noise contribution to the far-field. $\gamma^2_{CF}(f)$ is the coherence function between fluctuating combustor pressure and far-field pressure; and $G_{FF}(f)$ is the far-field acoustic spectrum.

We note, however, that it is possible that the single point pressure measurement within the combustor is not adequate to characterize the entire combustor source region. That is, there may be several (or perhaps, many) independent source regions within the combustor, each contributing to the far field acoustics. If such is the case, then the combustor coherence spectrum as computed from equation (30) will not include the contributions from the other combustor source regions and hence will be an underestimate of the true combustion noise contribution. (Note that this is an extension of case (b) above.) Evidence will be presented shortly, though, that this single point combustor pressure measurement is sufficient to make at least a reasonably accurate estimate of the actual combustion noise contribution to the far-field, and is entirely sufficient to characterize the spectral content and directivity of the combustor associated far-field noise.

5.2 Statistical Considerations

Since the techniques used here to measure the combustion noise utilize the tools of random data analysis, statistical errors, which are an inevitable byproduct of such techniques, are an important consideration. A discussion and computation of the confidence limits associated with the results to be shown are presented in appendix A. However, one particular source of error in the measurement of the coherence functions is related to the question of whether or not the single point combustor pressure measurement is sufficient to characterize the entire combustor source region, and so will be discussed here.

As shown in reference 30, and briefly mentioned in Chapter 3, an important bias error occurs when examining pairwise relations between signals with significant time delay between them. The proper way to eliminate, or at least minimize, this bias error is to remove this delay before processing, by shifting the appropriate signal in time. This shifting can be readily accomplished if the digitized data is being processed on a user-programmable digital computer. However, the digital signal processor used in this study did not have a provision for implementing this precomputation delay when computing coherence functions. Consequently this source of bias error could not be removed from the raw measurements.

In reference 30, the bias error due to the time delay is shown to be given by

$$\hat{\gamma}^2(f) = \gamma^2(f)\left(1 - \frac{\tau}{T}\right)^2 \qquad (31)$$

where

$\hat{\gamma}^2(f)$ is the coherence function estimate (i.e., the measured value)

$\gamma^2(f)$ is the true value of the coherence function

τ is the delay time between the two signals

and

T is the processor memory period (i.e., the sampling period for a single record) (See appendix A.)

In appendix A it is shown that for the computation scheme utilized by the DSP, the memory period is inversely proportional to the analysis frequency range f_m, and is given by $T = 500/f_m$. With this brief discussion, we can now return to the issue of the adequacy of a single point pressure measurement within the combustor in computing the combustor coherence spectra.

5.3 The Combustor as a Single Source Region

The first point to be made here is that one relative straightforward way of determining whether or not the combustor consists of a multitude of individual sources is to make a series of space-time cross-correlation measurements around the periphery of the combustor. The zero time delay value of these correlation functions can then be cross-plotted as a function of circumferential separation with respect to some fixed position and the result will be a two point correlation with separation distance as the independent variable, rather than time. From this result we could then estimate the circumferen-

tial correlation length of a single source region, and hence obtain the number of independent source regions within the combustor. However, only two fixed pressure measuring stations were available within the combustor and this approach could not be used.

Alternatively we can examine the pressure coherence between the two measuring stations available. If this results in a uniformly high coherence over the frequency range of interest (approximately 0 to 250 Hz), then this would at least suggest that a 90° sector is the minimum size of the correlating region and that, at most, there are about four independent source regions. This coherence function between the pressure signals 90° apart in the combustor is shown in figure 47. The result shows that uniform coherence does not prevail. The coherence between the two is relatively uniform and high from about 0 to 100 Hz or so, but drops substantially beyond 100 Hz. This result is consistent with the notion that low frequencies tend to correlate over longer distances than high frequencies. It suggests that up to about 100 Hz, the correlating (i.e., source) region extends to at least 25 percent of the combustor annulus. At frequencies beyond about 100 Hz, however, the results seem to indicate that the correlating regions are smaller and therefore more numerous.

This issue can be at least partially resolved by reexamining the coherence function between the pressure in the combustor and the acoustic pressure in the far-field. This function was originally shown in figure 16. There, however, we were concerned with diagnostic measurements only and the numerical values of the coherence were not of immediate concern. To illustrate more graphically the

fact that there is virtually no acoustic contribution from the combustor to the far field beyond about 250 Hz, a relatively broad analysis range of 1500 Hz was chosen to present the data. The memory period for the DSP at 1500 Hz is $T = 500/f_m = 500/1500 = 0.333$ seconds. From figure 27(a), the time delay, τ, between combustor and far field is about 87 msec. So, from equation (31), the bias error due to time delay is:

$$\hat{\gamma}^2(f) = \gamma^2(f)\left(1 - \frac{\tau}{T}\right)^2$$

or

$$\frac{\hat{\gamma}^2(f)}{\gamma^2(f)} = \left(1 - \frac{0.087}{0.333}\right)^2 = 0.545$$

The coherence estimate in figure 16 then is only about 54.5 percent of the true value.

To show the effect of this time delay bias, the coherence between combustor and 120° far-field pressures was recomputed at a lower frequency range (at the expense of increased random error, as is shown in appendix A). The result, for an f_m of 400 Hz is shown in figure 48. Now the peak coherence has risen to a value of about 0.62, in contrast to the value of 0.33 in figure 16. We could recompute this coherence function once again at a still lower frequency of 200 to 250 Hz, the maximum frequency of interest. Here, however, the random error gets too large (see appendix A), so a calculated bias correction will be applied to the results of figure 48. For this case, the memory period of the DSP is $T = 500/400 = 1.25$ seconds. (The time delay, τ, is still 87 msec.)

$$\gamma^2(f) = \frac{\hat{\gamma}^2(f)}{\left(1 - \frac{0.087}{1.25}\right)^2} = \frac{0.62}{0.869} = 0.72$$

The true value of the coherence, then, is nearer to 0.72. So, at the peak frequency, approximately 72 percent (i.e., within 1.5 dB) of the far-field signal can be accounted for by a single point pressure measurement in this combustor. Considering the fact that at least part of the far-field noise at this frequency must contain contributions from the other engine noise sources, the assumption that a single point pressure measurement in the combustor is sufficient to characterize the source region appears reasonable. This argument applies only to frequencies near the peak. However, again considering the notion that low frequency information should correlate over larger distances than high frequency information, the assumption is probably valid at frequencies below the peak also, when even larger correlation volumes could be expected.

We are now left only with the question of the reduced coherence at frequencies between about 125 Hz and 200 to 250 Hz. With the information obtained to this point, no firm conclusions can be reached as to whether this results from multiple, independent source regions within the combustor at the higher frequencies (i.e., above 125 Hz) or is a true indication of the combustor-associated far-field noise. The overall combustor noise power levels in the far-field, which are presented in a later section, will be seen to be somewhat low when compared with most of the empirical predictions, although not excessively low. The possibility is admitted, therefore, that

additional measuring stations within the combustor may be required to account for all the source regions within the combustor. Their exact number, however, could not be determined without a comprehensive analysis or experimental program to completely characterize the combustor as a source region.

The possibility of different azimuthal regions within the combustor contributing to different spectral ranges in the far-field acoustics may be ruled out on simple geometric symmetry considerations. Figure 49, which shows the coherence function between the second combustor probe and the 120° far-field microphone is adequate evidence for this conclusion. The spectral range of coherence, and the shape of the coherence function, is virtually identical to that of the in-line combustor probe, shown in figure 16.

5.4 Combustor Coherence Spectra; Radiation Patterns

From equation (30), the combustor coherence spectrum is defined, for the present case, as:

$$C(f) = \gamma^2_{CF}(f) G_{FF}(f)$$

This can be computed directly through a frequency by frequency multiplication of the measured pressure coherence function between combustor and far-field and the measured auto-spectrum of the far-field acoustic pressure[1]. This multiplication could be implemented

---

[1]The result of this multiplication is often referred to as the coherent output power in literature on random data analysis. However, to avoid confusion with the physical quantity of acoustic power, which will be calculated later, the term combustor coherence

directly on the DSP.

The data to be shown were all computed with an analysis range, f_m, of 400 Hz. In addition to the bias error in the estimate of $\hat{\gamma}^2$ due to time delay, as described earlier, there are random and bias errors in the estimate due to finite sample records. As shown in appendix A, for the computational scheme utilized by the DSP, the criteria for minimizing all these errors are in conflict. The choice of 400 Hz, therefore, represents a compromise.

The bias error due to time delay for $f_m = 400$ Hz was calculated earlier, and found to underestimate the true coherence by a factor of 1/0.869. Expressed in decibels this error is seen to be $\Delta = 10 \log 0.869 = -0.65$ dB. The computed combustor coherence spectra, then, will be biased low by about 0.6 dB. This small correction is not made in the data to be shown in this section, but is accounted for when the acoustic power results are presented. Confidence limits for the combustor coherence spectra are described in appendix A and are tabulated in appendix B.

Additionally before presenting the data, we note that corrections to the far-field spectra due to atmospheric absorption have not been made. At the low frequencies of interest here, this correction is entirely negligible (35). The data have also not been corrected to free-field to account for the pressure doubling due to the ground mounted microphones (+6 dB). Again, however, these

---

spectrum will be used here. This is in keeping with the idea that it represents that portion of the far-field acoustic spectrum which is coherent with the fluctuating pressure in the combustor.

corrections were applied to the acoustic power results, shown later. Also, no corrections were made to standard-day conditions. The data to be presented in this section, therefore, are "as-measured." Finally, all the data to be shown in this section have been normalized to a spectral density basis, so that the results are presented in dB/Hz.

Some representative far-field sound pressure level spectral densities at angles of 60°, 120°, and 160° are shown in figures 50(a), (b), and (c) (dashed curves), respectively, for an engine operating speed of 43 percent. The resulting combustor coherence spectra at these angles are shown by the solid curves on the same figure. These were obtained by a direct frequency by frequency multiplication of the far-field spectra by the appropriate coherence functions. The primary observation to be made is that because the far-field acoustic spectra are relatively flat over the relevant frequency range, the combustor coherence spectra peak approximately at the same frequency as the coherence functions themselves, around 125 Hz as shown earlier. Also, as first suggested from the coherence functions, the results indicate that there is virtually no combustor associated noise at frequencies above about 200 to 250 Hz.

Results similar to above were obtained for each of the far-field microphones (40° through 160°) and for each of the engine operating conditions through 60 percent. Since the resultant combustor coherence spectra were all normalized on a spectral density basis, the area under any given combustor coherence spectrum represents the overall sound pressure level (OASPL), over the frequency

range 0 to 400 Hz (although the contribution beyond about 200 to 250 Hz is negligible, as shown above). However, because the DSP was not interfaced with a computer this integration was performed manually for each combustor coherence spectrum. Eleven points on each spectrum, in intervals of 20 Hz, from 40 to 240 Hz were selected for the summation. These eleven points were anti-logarithmically summed. The result was then multiplied by 20 Hz (i.e., 10 log 20 = 13 dB was added) to account for the effective 20 Hz bandwidth. The final result for each combustor coherence spectrum, then, represents an approximation to the OASPL up to a frequency of 240 Hz. For smoothly varying spectra, the approximation is adequate.

This procedure was repeated for each microphone angle. The result may be plotted as a function of angle to produce the radiation pattern of the combustor associated far-field noise. The results are shown in figure 51, for three engine power settings of 30, 43, and 60 percent. As would be expected, there is a slow increase in combustor associated far-field noise at all angles as engine power is increased. The radiation patterns, however, remain constant, with a slight peak near 120°. The peak angle is consistent with that found by other investigators (ref. 35, for example). Similar results were found to prevail at the intermediate engine power settings of 37 and 50 percent, but are not shown on figure 51 in the interest of clarity.

Because the radiation patterns remain invariant with engine power setting, they may be normalized, for convenience purposes, into a single directivity index curve. The directivity index is

defined as the difference (in decibels) between the measured sound pressure level at a point and the sound pressure level that would exist at the same point from a simple monopole source emitting the same acoustic power. The simple-source sound pressure levels were computed by area weighting the combustor-associated OASPL, as described in reference 36. The computations were performed by using a slightly modified version of a standard computer program in use at the Lewis Research Center for handling acoustic data, also described in reference 36. The result, arithmetically averaged over the five engine operating speeds between 30 and 60 percent, is shown in figure 52 (symbols).

For comparison purposes, the directivity index as obtained from the empirical prediction schemes outlined in references 19, 32, and 37 are also shown. The present results are seen to be in remarkably close agreement with the empirical prediction scheme of (37). The recommended prediction procedure of reference 19 appears to overpredict the results found here at forward and rearward angles near the engine axis. The procedure of (32) produces results which somewhat overpredict the measured data at the rearward angles. However, in the range between about 60° and 130°, the results found here agree reasonably well with all three prediction schemes.

5.5 Combustor Associated Far-Field Acoustic Power

The combustor associated far-field acoustic power spectra and total power may also be obtained from the combustor coherence spec-

tra. For each of the 11 frequencies selected from the combustor coherence spectra, a point on the combustor far-field acoustic power spectrum was computed for a given engine power setting. The basic equation used was (36):

$$\text{Power} = W = \frac{1}{\rho c} \sum_{i=1}^{N} p_{f,i}^2 \, \Delta A_i$$

Here, ρ and c are the ambient density and speed of sound, respectively; $p_{f,i}^2$ is the mean-squared pressure at the selected frequency f, i is the summation index corresponding to each microphone location and the ΔA_i are finite incremental areas on which the corresponding $p_{f,i}^2$ are presumed constant. Any set of consistent units may be used for ρ, c, and p. Again, a standard computer program described in reference 36, was adapted for implementing the computation.

The results, on a spectral density basis, (dB/Hz, referenced to 10^{-13} W) are shown in figure 53, for three engine speeds of 30, 43, and 60 percent of maximum. The spectral shapes are seen to vary somewhat as operating speed increases with the primary differences occurring at frequencies beyond the peak. There appears to be a trend towards a slightly increasing peak frequency with engine operating speed, but this may be an artifact of the relatively large bandwidth (20 Hz) chosen for the numerical integration.

The integrated overall sound power level (OAPWL) (re 10^{-13} W) are shown adjacent to each curve in figure 53 (corrected for time delay bias). Table I presents a comparison of the present results with the empirical prediction schemes of references 19, 32, and 37.

The coherence results are seen to agree reasonably well with the prediction of reference 19, but are considerably less than those of references 32 and 37. This suggests the possibility of the inadequacy of a single point combustor measurement in characterizing the source region, as discussed in section 5.2.

Table I

Overall Power Level
(dB, re: 10^{-13} W)

Engine speed, percent of max.	Ref. 19	Ref. 32	Ref. 37	Coherence results
30	120.9	127.0	128.7	120.0
43	122.7	131.5	133.2	123.5
60	126.3	136.0	137.7	126.2

The final comparison to be made is the peak frequency found by the coherence results here with the peaks predicted, for this engine, by the procedures outlined in references 19, 32, and 37. For the most part these are independent of operating condition (as found here) within about 5 Hz. The results are:

Ref.	Predicted peak frequency, Hz
19	260
32	400
37	330
Present	125

At engine speeds beyond 60 percent of maximum the numerical value of the coherence function between the combustor pressure and

the far-field pressure diminished significantly. This is shown in figure 54 for an engine speed of 75 percent, the next highest power setting which was tested. The low numerical value of the coherence results primarily from the rapid increase in jet mixing noise which, as will be recalled from the INTRODUCTION, increases as the eighth power of jet velocity. Beyond 75 percent speed, no measurable coherence between the pressure in the combustor and the far-field was observed. This does not mean, of course, that the combustor is no longer contributing to overall engine noise, but that its proportional contribution at these higher engine speeds is extremely small.

In principal this contribution, however small, can be extracted through the coherence function. However, as shown in appendix A, as the estimated value of the coherence function becomes small, the variance of the estimate becomes very large, for a fixed number of sample records. To reduce this variance requires the availability of large amounts of data. The 120 second record lengths used here are not sufficient to provide adequate statistical confidence when the numerical value of the estimated coherence function falls below about 0.05. This corresponds to a contribution of the combustor associated far-field noise some 13 dB below the overall level. As is shown in the tabulated confidence limits in appendix B, for a 90 percent confidence limit of about ±3 dB, this would require approximately five times more data than was used in this investigation, or record lengths of approximately 10 minutes.

Before concluding this chapter, two additional points regarding the numerical results found here should be discussed. First, it is clear that there is a significant discrepancy between the combustion noise spectral peak found here compared with that predicted by the empirical procedures of other investigators. It should be pointed out that the data used to develop those empirical equations were obtained from engines and combustors quite different than the YF-102, with its reverse flow combustor (although the YF-102 operating and geometric parameters were used to arrive at the predicted peak frequencies shown earlier). Since it is not unreasonable to expect geometry to play a significant role in determining spectral characteristics, it is not surprising to find such discrepancies between the measured and predicted spectral peaks. Clearly, the investigation of scaling relationships may prove a fruitful avenue for future research.

Finally, we address the issue of the basic numerical accuracy of the data shown in this chapter. As pointed out in Chapter 3 the measurement errors, being associated entirely with the microphones, may be considered quite negligible when considering the accuracy of present day microphone and amplifier systems (± 1 dB). The largest area for inaccuracy results from the statistical errors associated with the data processing. A thorough discussion of these is presented in Appendix A. Briefly, it is shown that the error in the integrated results (i.e., OASPL and OAPWL) are dominated by the errors near the corresponding peak spectral values, where the measured coherence is

quite high, resulting in relatively small errors. For example, at 43% of maximum speed, the 90% confidence limits on the calculated OAPWL is -1.7 dB to 1.0 dB, with virtually identical results at the other speeds. By contrast, the errors at the extremes of the spectrum are quite large due to low coherence. For 43% of maximum speed, the 90% confidence limit on the power level is about -3 dB to +2 dB at 40 Hz and about -10 dB to +4 dB at 240 Hz. Similar results prevail at the other engine speeds.

6. SUMMARY AND CONCLUDING REMARKS

6.1 Summary

Chapter 1. In chapter 1, the motivation for the experimental program described in this thesis was established. Specifically, it was indicated that recent evidence suggests that the reduction of fan and jet noise under flight conditions results in core associated noise becoming a significant contributor to overall turbofan engine noise. Furthermore, current research has shown the duct-burning turbofan to be a promising candidate for possible supersonic transport applications. In both cases above, the identification and measurement of combustion-associated far-field noise is required to characterize the overall engine noise. Such a step is necessary before further major reductions in aircraft propulsion system noise can be accomplished.

Chapter 2. In chapter 2, a review of Lighthill's governing equation for aerodynamic noise generation was presented. It was shown that in a combustion region, a slight modification in the basic source term of Lighthill's equation enabled the fluctuating pressure in the combustor to be related to the far-field acoustic pressure. It was further shown that this relationship was uniquely determined by the phase and amplitude information contained in the

transfer function between combustor pressure and far-field pressure. Specifically, for the model proposed, the far-field acoustic pressure was related to the combustor pressure by a transfer function proportional to frequency squared, and a 180° phase shift. Furthermore, for the model proposed, it was shown that the corresponding time domain relation between combustor pressure and far-field acoustic pressure, the cross-correlation function, could be expected to have an evenly symmetric shape with a negative peak at a time delay corresponding to the acoustic propagation time between the combustor source region and the acoustic observation point.

These relations were contrasted to the corresponding information which would be expected for "scrubbing" noise (i.e., surface interaction noise), or pure time delay.

Chapter 3. This chapter described the experimental hardware and instrumentation. Briefly, the engine on which the measurement program was conducted was an AVCO-Lycoming YF-102 turbofan engine with a bypass ratio of six to one. The fluctuating pressure measurements within the engine core were accomplished with specially constructed "semi-infinite" waveguide probes, with conventional microphones being used as the pressure transducers. The data obtained from these probes, as well as from an array of far-field microphones, were off-line processed on a Fast Fourier Transform (FFT) digital signal processor (DSP). The DSP was used to obtain the time and frequency domain relations described in chapter 2, as well as the ordinary coherence functions, between the fluctuating

pressures within the engine core and between these pressures and the far-field acoustic pressures.

Chapter 4. The results of a series of diagnostic measurements were presented in this chapter. The measured coherence function between the fluctuating combustor pressure and the far-field acoustic pressure indicated that the fluctuating combustor pressure was not related to the far-field acoustic pressure at frequencies beyond about 250 Hz. Using this as a guide, low-pass filtered cross-correlation functions were computed between combustor pressure and tailpipe pressure, between combustor pressure and far-field acoustic pressure, and between tailpipe pressure and far-field acoustic pressure.

The shapes of these functions as well as the corresponding frequency domain information (transfer function magnitude and phase) obtained by Fourier transforming them after removing the time delays, were consistent with the behaviour modeled in chapter 2. Specifically, the transfer functions between combustor pressure and nozzle pressure, and between combustor pressure and far-field acoustic pressure were found to have a magnitude approximately proportional to frequency squared. Similarly, the corresponding phase shifts were found to be approximately 180° independent of frequency, after time delay removal. By contrast, the transfer functions between nozzle pressure, and between nozzle pressures and far-field pressure were found to have a magnitude independent of frequency (i.e., flat) and a phase of 0° after time delay removal. From these

results it was concluded the combustor was a source region for low frequency noise (less than 250 Hz) which propagated through the nozzle and out to the far-field.

Chapter 5. Having identified the combustor as a source region for far-field noise in the previous chapter, its quantitative contribution was determined in chapter 5. The tool used for this was the ordinary coherence function between combustor pressure and far-field pressure. A frequency by frequency multiplication of this ordinary coherence function by the corresponding far-field spectrum produced the combustor coherence spectrum. Under the appropriate assumptions, the combustor coherence spectrum may be interpreted as the spectral contribution of the combustor to overall engine far-field noise. These spectra were obtained for each microphone angle and over a broad range of engine operating conditions. These results were, in turn, used to obtain the directivity patterns of the combustor associated far-field noise, acoustic power spectra, and total acoustic power.

The directivity patterns were found to be relatively independent of engine operating speed, and agreed well over most angles with two existing prediction schemes, and remarkably well over all angles with a third. The power spectra were found to peak near 125 Hz, relatively independent of engine speed, with greater amounts of energy at frequencies beyond the peak as engine speed increased. In all cases, however, there was virtually no combustor associated noise at frequencies above about 250 Hz. The total acoustic power was

found to agree very closely with that predicted by one of three existing prediction schemes with which it was compared, but somewhat low when compared with the other two. The peak frequency of 125 Hz was found to be approximately one to two octaves below the results obtained from all three prediction schemes. Reference evidence was cited, however, to support this result for gas turbine combustion noise peak frequencies for the size class of this engine.

6.2 Concluding Remarks

With respect to the specific problem of combustion noise from turbofan engines, clearly there is much work still required to enable the development of techniques for its suppression to be accomplished on a rational basis. For example, the design of liners or suppressors for combustion noise reduction obviously requires knowledge of its spectral content. As was shown in the previous chapter, however, the existing empirical schemes for predicting turbofan combustion noise characteristics are certainly not adequate for predicting spectral content. Yet, extensive parametric testing of suppressor hardware or new combustor designs in full scale operational turbofan engines using the techniques described in this investigation would be prohibitively expensive. Clearly, it would be desirable to implement such testing on less expensive, more adaptable apparatus specifically designed for such purposes. However, as pointed out earlier, it is not yet clear how the results of combustion noise tests in such apparatus can be related or applied to

actual engines. Here, it would seem, the techniques and procedures described in earlier chapters may be used or extended to enable a fuller understanding of combustion noise phenomena in such combustor rigs.

Finally, as stated in the INTRODUCTION, one of the primary objectives of the present investigation has been to specifically identify combustion noise as a component of core associated far-field noise from a turbofan engine. As described in chapter 4, this identification has been made. Furthermore, in contrast to procedures which rely solely on far-field acoustic measurements, the identification of the combustor as a source for low frequency core associated noise is unambiguous. Of equal significance, however, has been the demonstration that the techniques of random data analysis can be successfully applied to full scale, operational turbofan engines for both diagnostic and measurement purposes. This success, clearly, depends to a large extent on having a physical model of the acoustic generating mechanism available. The measurement techniques described herein, as well as the physical models for aerodynamic noise generation have been available for many years. It is the bringing together or both in a unified experimental program with practical engineering objectives which the present author feels is the major contribution of this work.

FIGURES

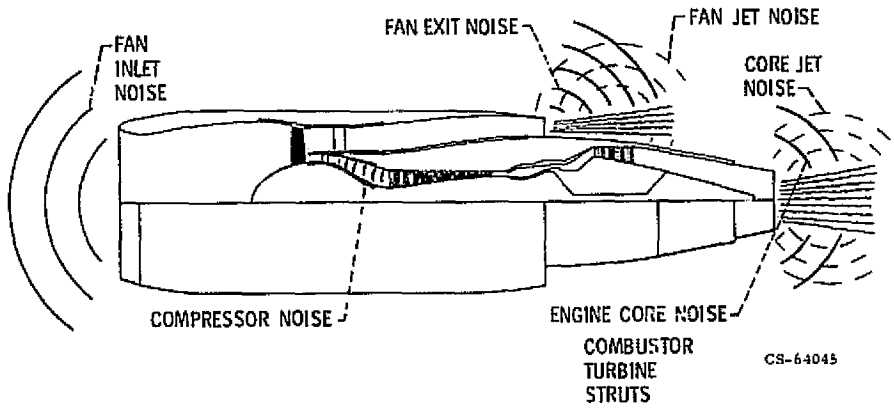

Figure 1. - Turbofan Engine Noise Sources.

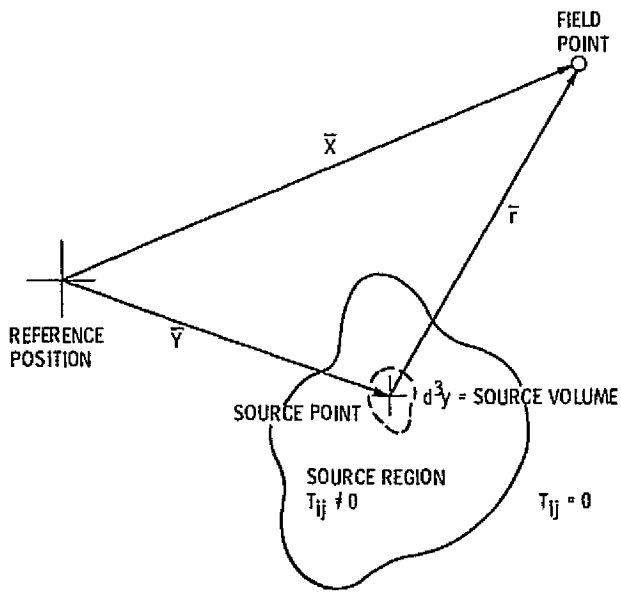

Figure 2. - Source-field Geometry.

$$\frac{d^m}{dt^m} f_1(t) \frac{d^n}{dt^n} f_2(t+\tau) = (-1)^m \frac{d^{n+m}}{d\tau^{n+m}} \overline{f_1(t) f_2(t+\tau)}$$

WHITE NOISE

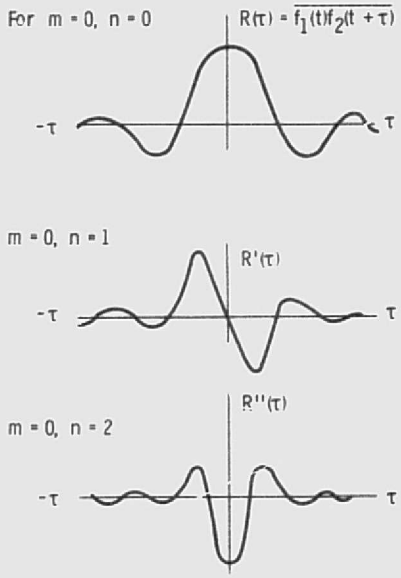

Figure 3. - Derivative Theorem For Correlations.

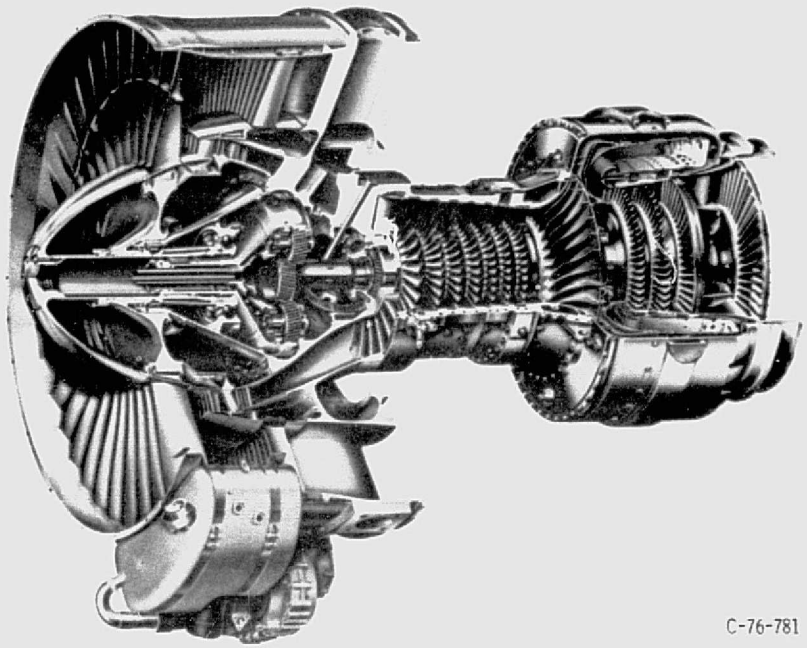

C-76-781

Figure 4. - Cutaway Illustration of YF-102.

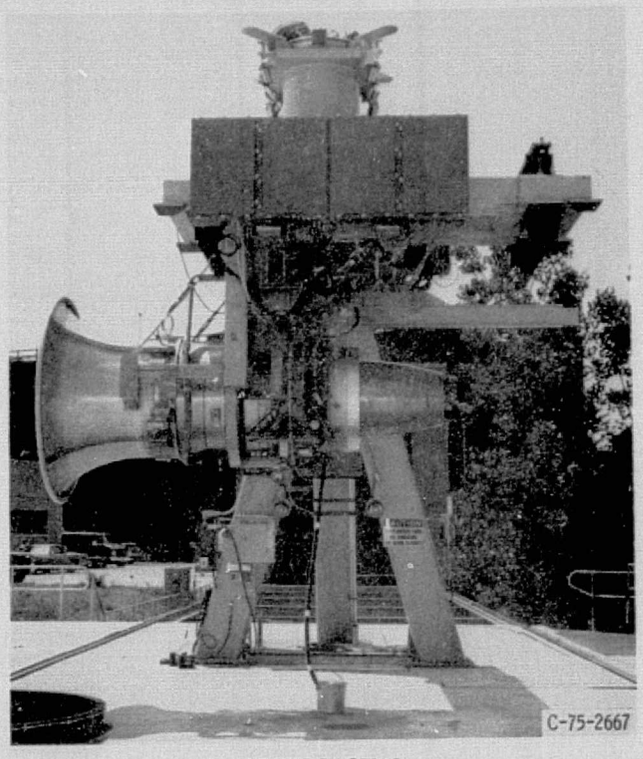

ENGINE ON STAND.

Figure 5.

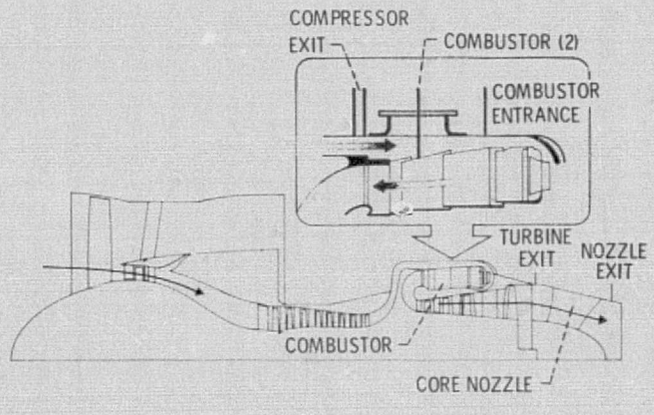

Figure 6. - Core Pressure Probe Locations.

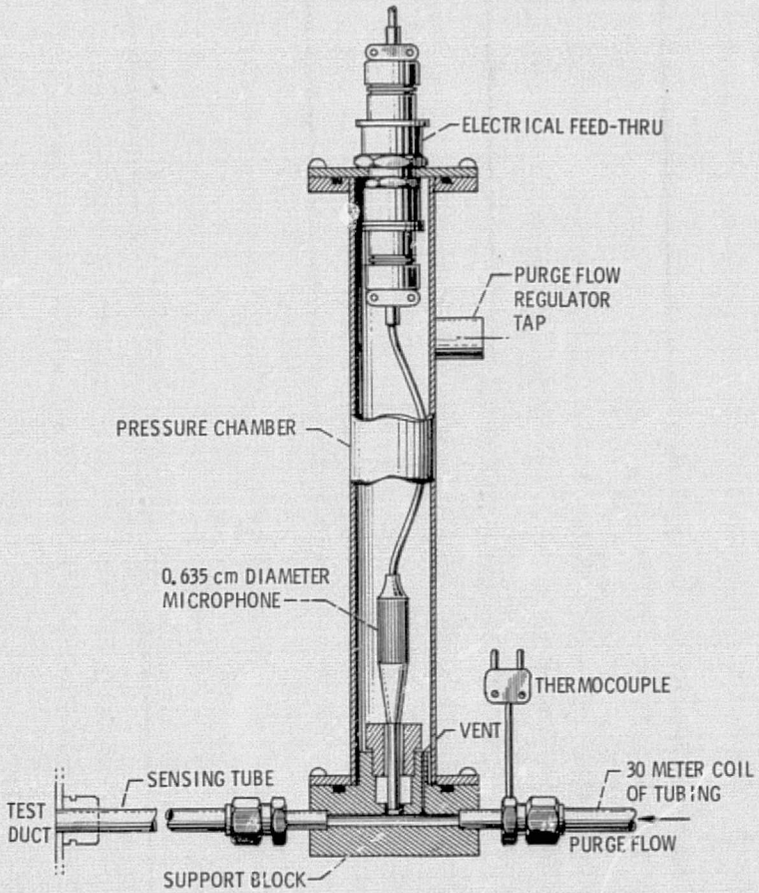

Figure 7. - Core Pressure Probe.

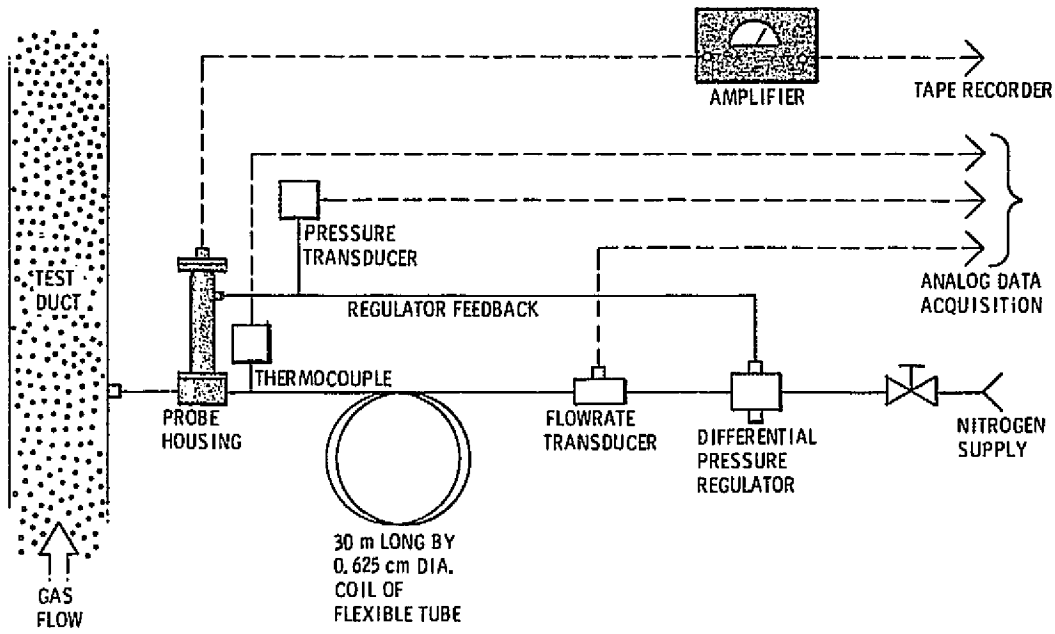

Figure 8. - Schematic Of Core Probe Installation.

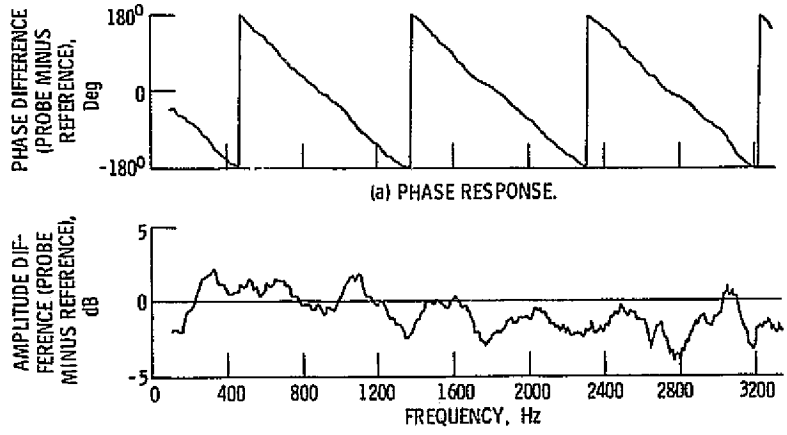

(a) PHASE RESPONSE.

(b) AMPLITUDE RESPONSE.

Figure 9. - Frequency Response For A Typical Acoustic Waveguide Probe.

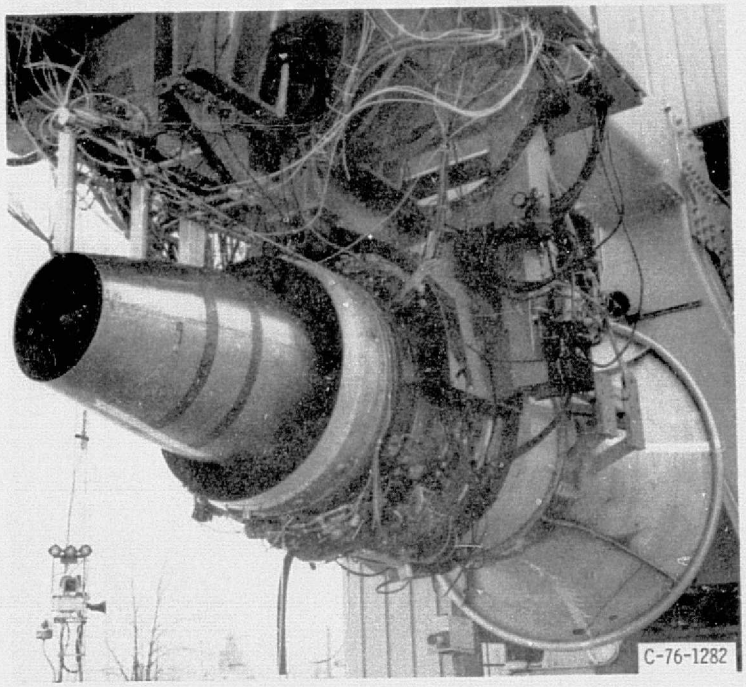

Figure 10. - YF-102 Turbofan Engine With Mounted Probes.

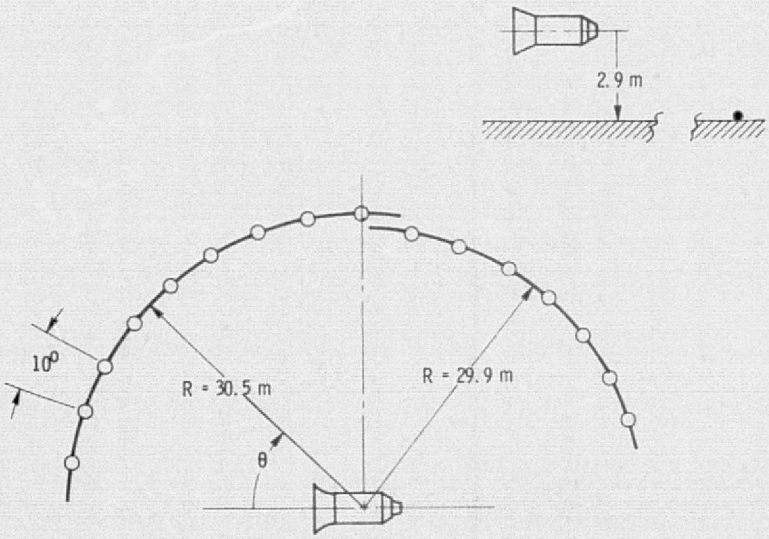

Figure 11. - Test Arena Geometry.

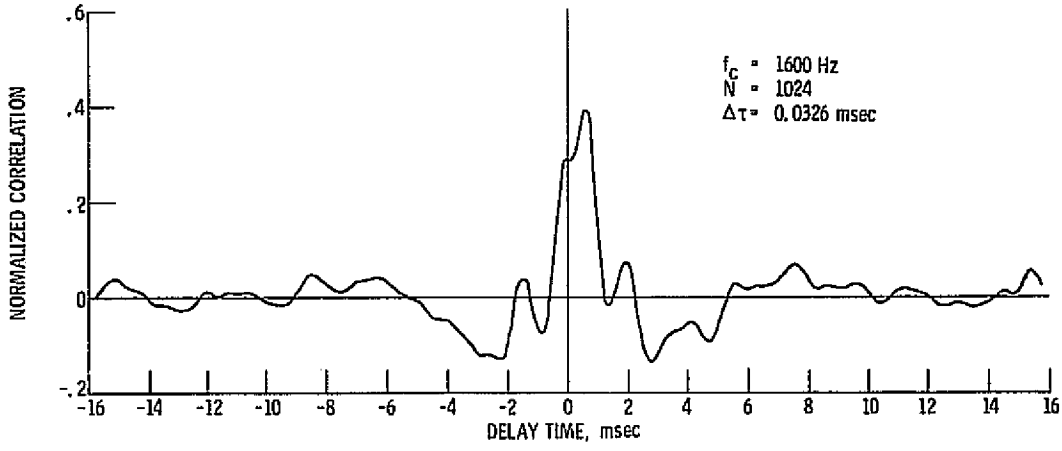

Figure 12. - Cross-Correlation Between Tailpipe Pressures (43% Speed).

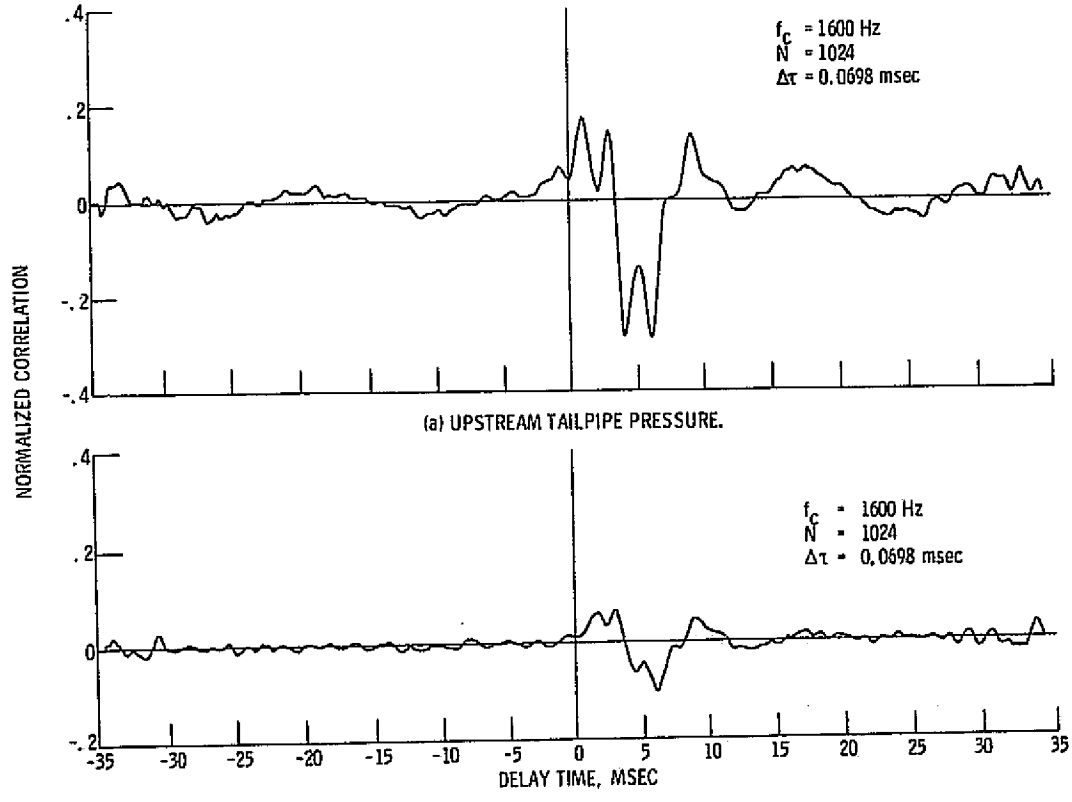

Figure 13. - Cross-Correlation Between Combustor Pressure and Tailpipe Pressures (43% Speed).

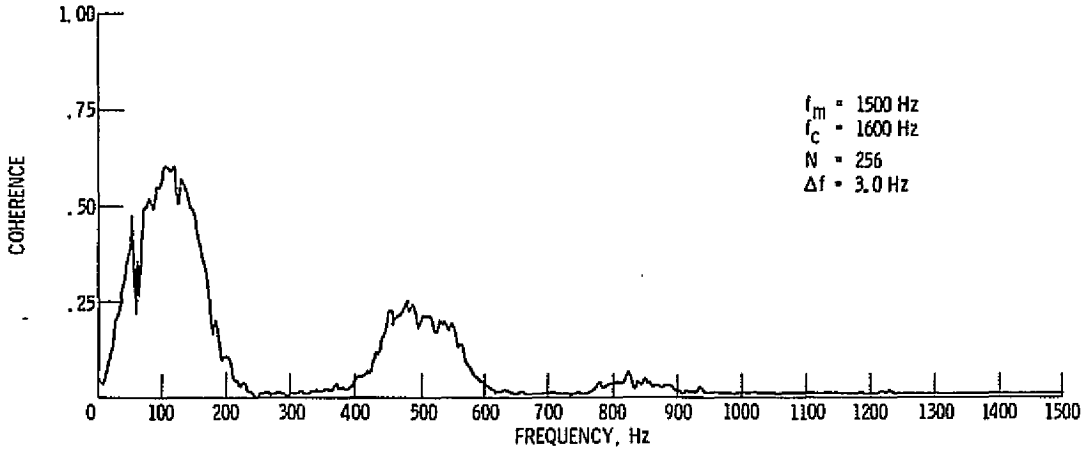

Figure 14. - Coherence Between Combustor and Upstream Tailpipe Pressures (43% Speed).

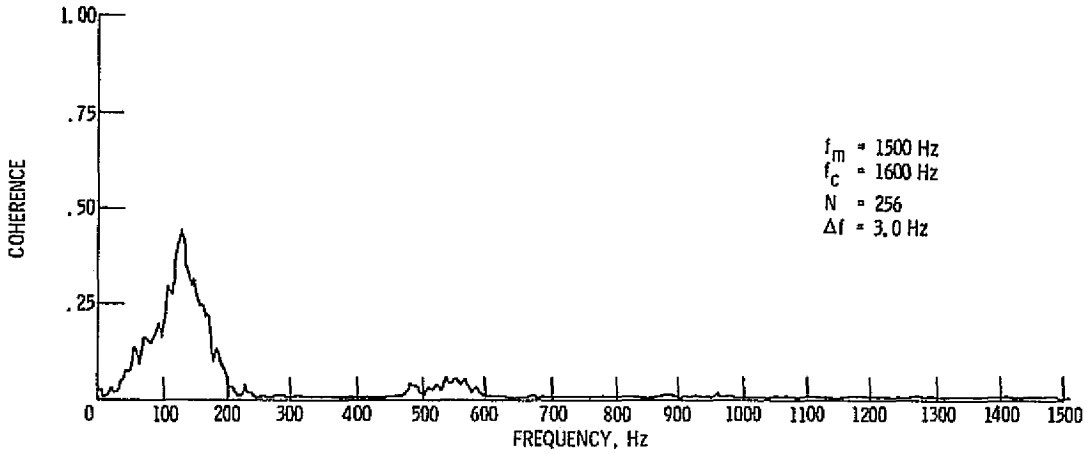

Figure 15. - Coherence Between Combustor and Downstream Tailpipe Pressures (43% Speed).

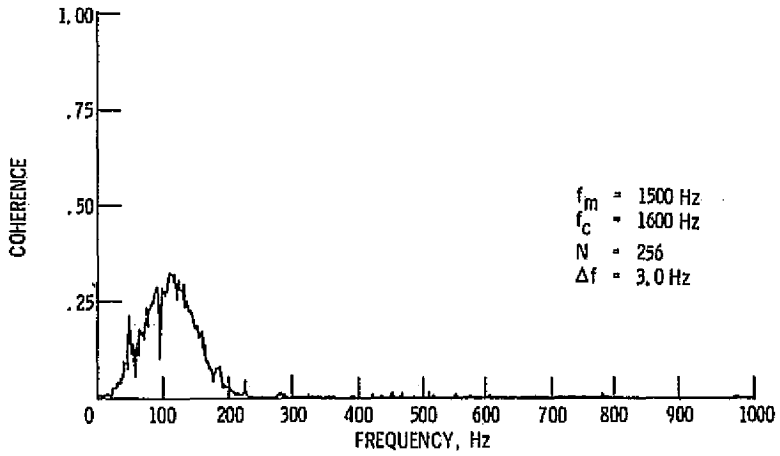

Figure 16. - Coherence Between Combustor Pressure and 120° Far-Field Acoustic Pressure (43% Speed).

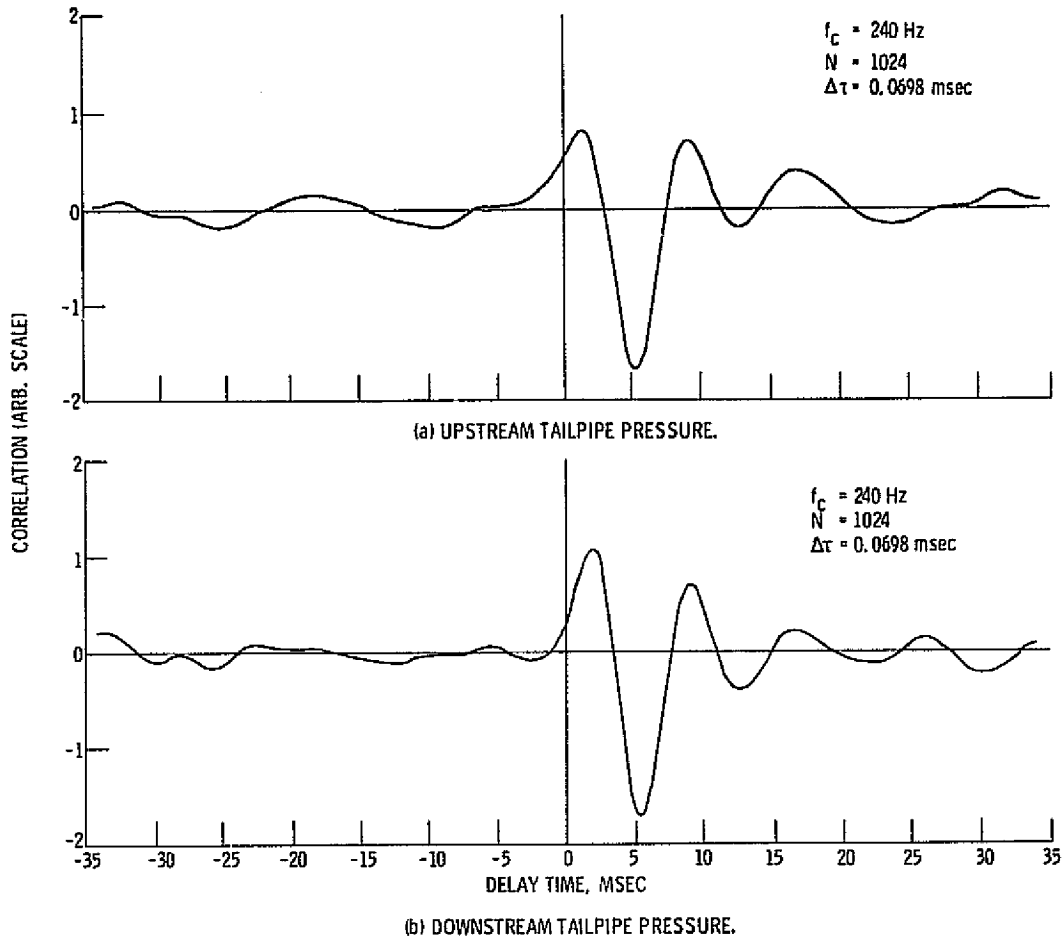

Figure 17. - Low-Pass Filtered Cross-Correlation Between Combustor and Tailpipe Pressures (43% Speed).

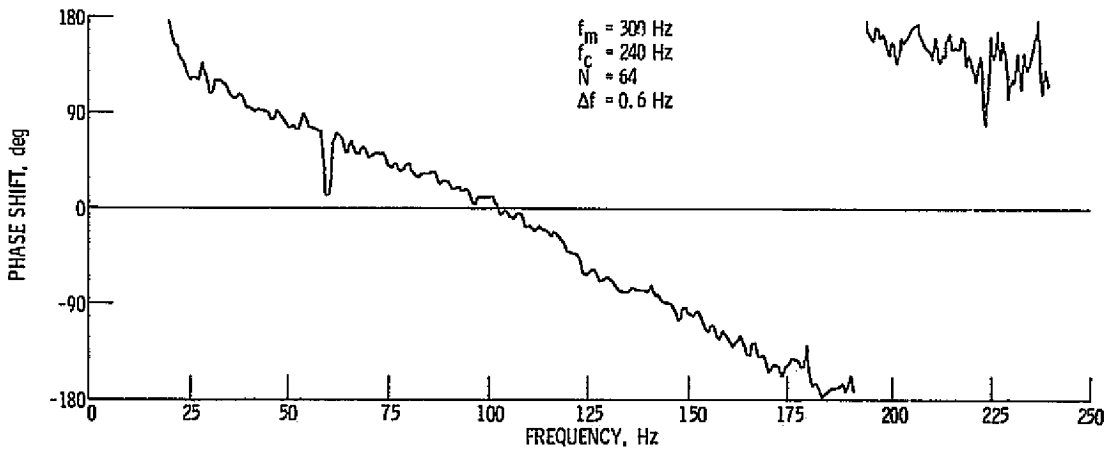

Figure 18. - Phase Shift Between Combustor And Upstream Tailpipe Pressures (43% Speed).

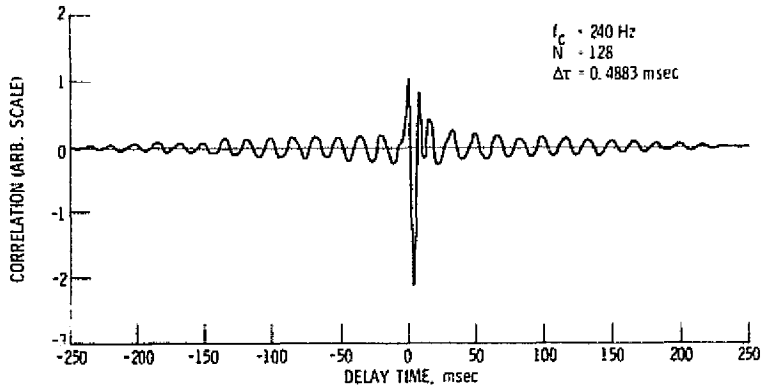

Figure 19. - Compressed Cross-correlation Between Combustor And Upstream Tailpipe Pressures (43% Speed).

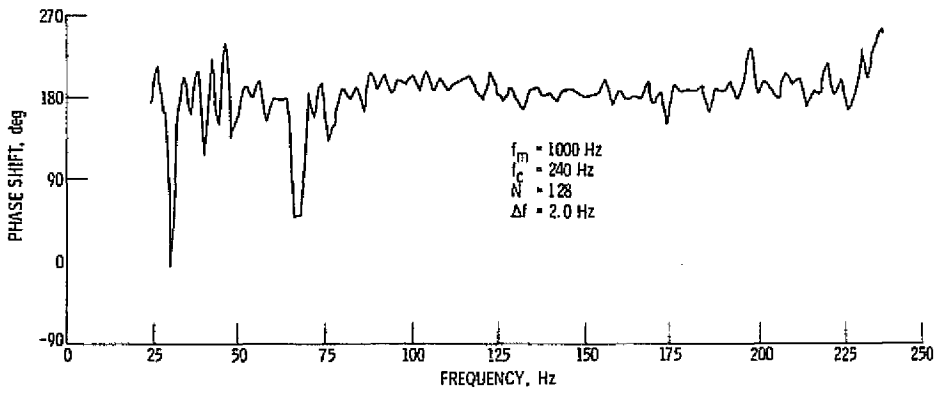

Figure 20. - Phase Shift Between Combustor And Upstream Tailpipe Pressures, Time Delay Removed (43% Speed).

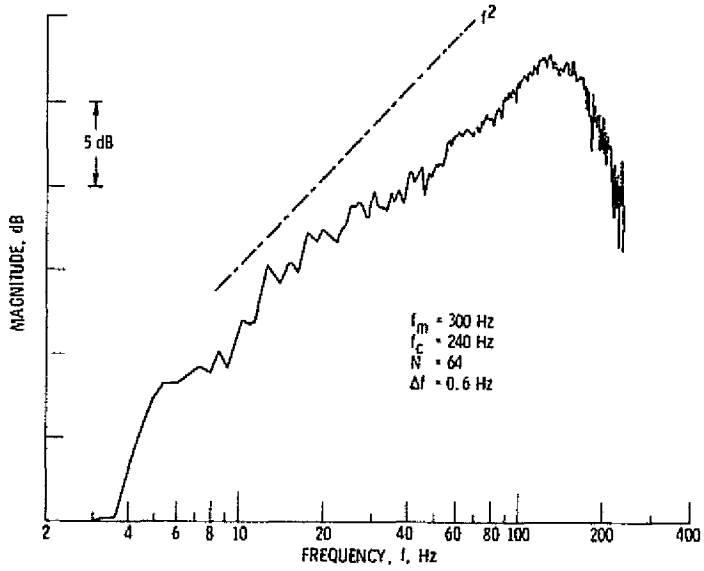

Figure 21. - Transfer Function Magnitude Between Combustor And Upstream Tailpipe Pressures (43% Speed).

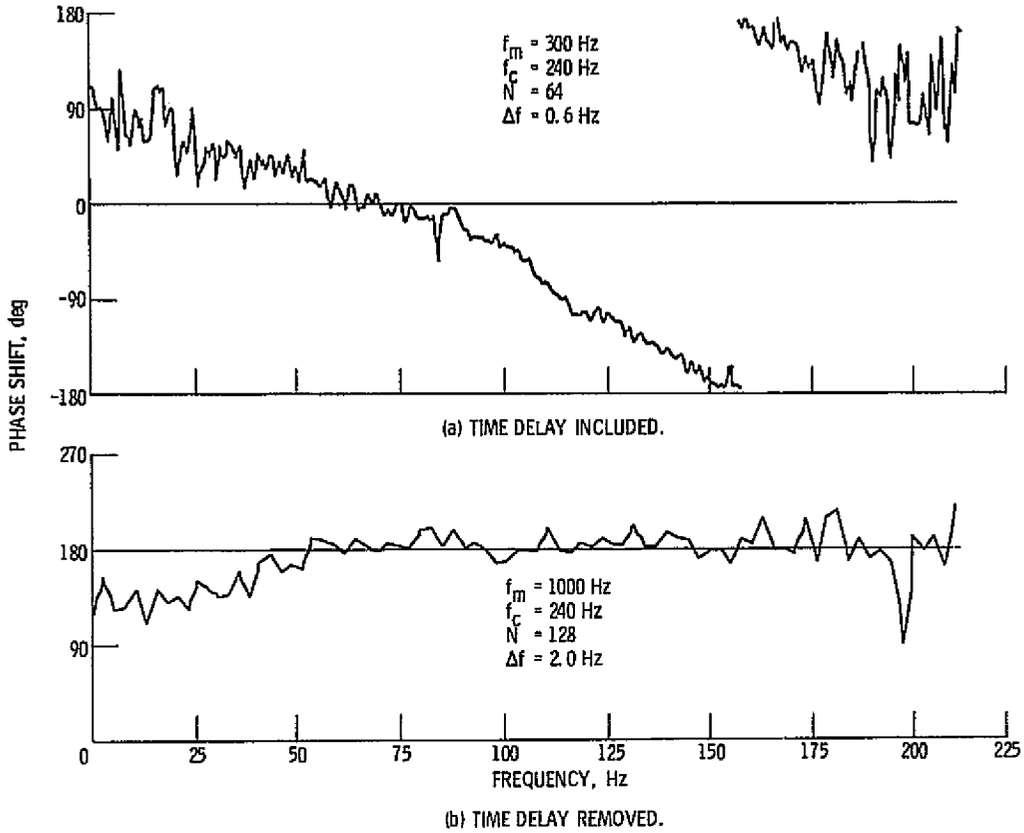

Figure 22. - Phase Shift Between Combustor And Downstream Tailpipe Pressures (43% Speed).

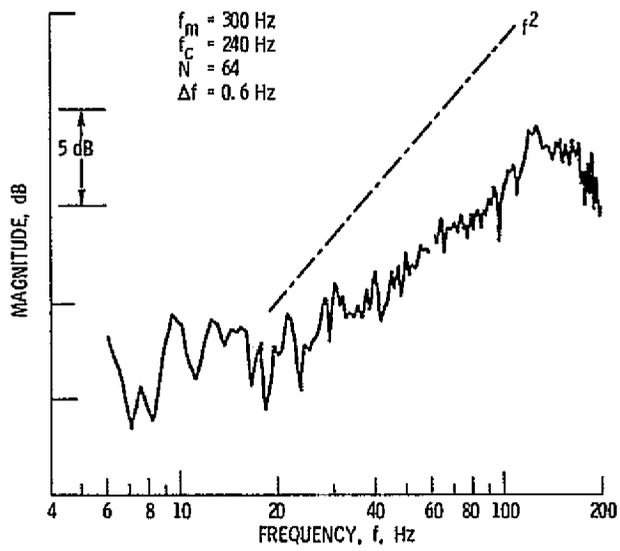

Figure 23. - Transfer Function Magnitude Between Combustor and Downstream Tailpipe Pressures (43% Speed).

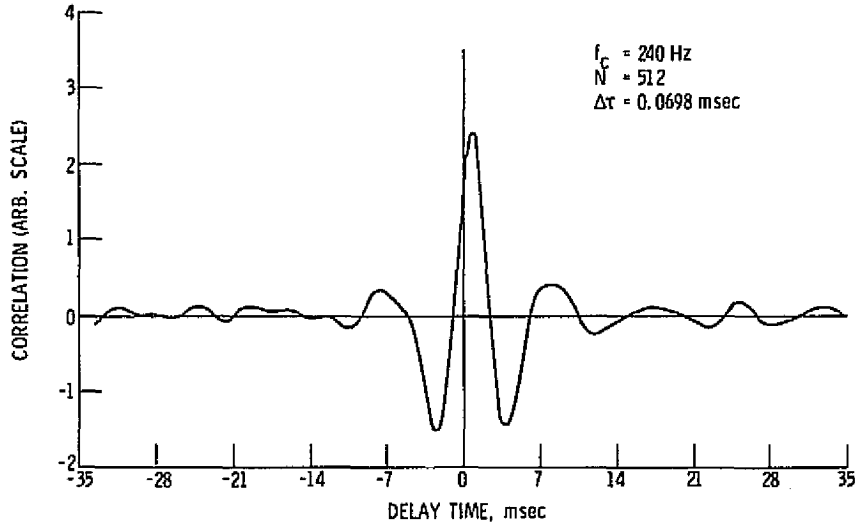

Figure 24. - Low Pass Filtered Cross-correlation Between Tailpipe Pressures (43% Speed).

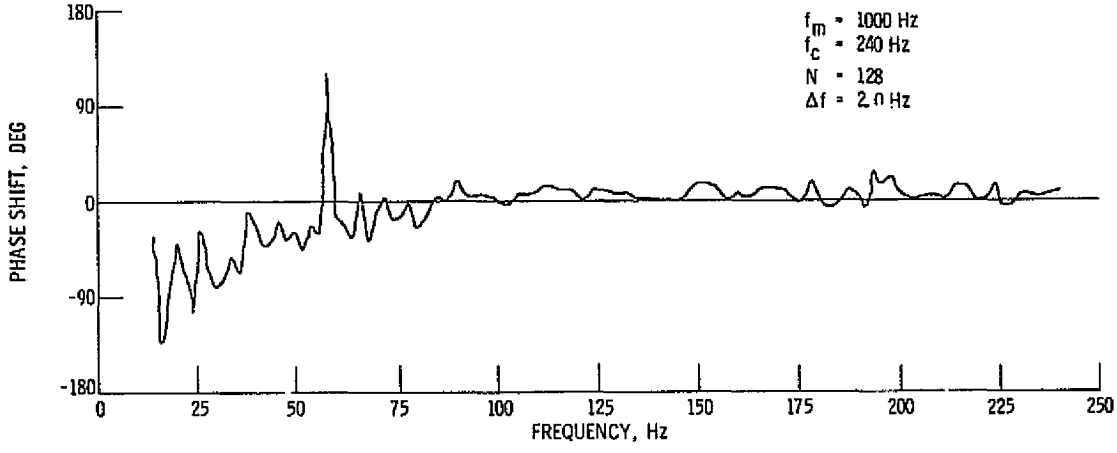

Figure 25. - Phase Shift Between Tailpipe Pressures, Time Delay Removed (43% Speed).

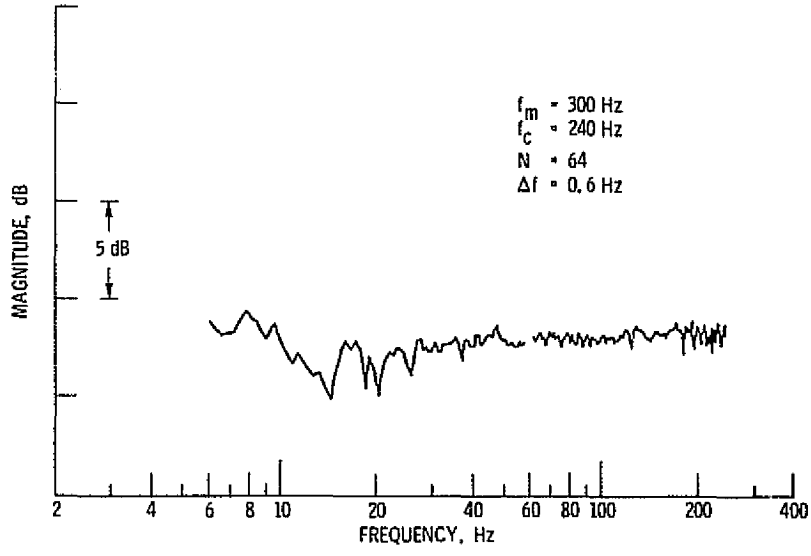

Figure 26. - Transfer Function Magnitude Between Tailpipe Pressures (43% Speed).

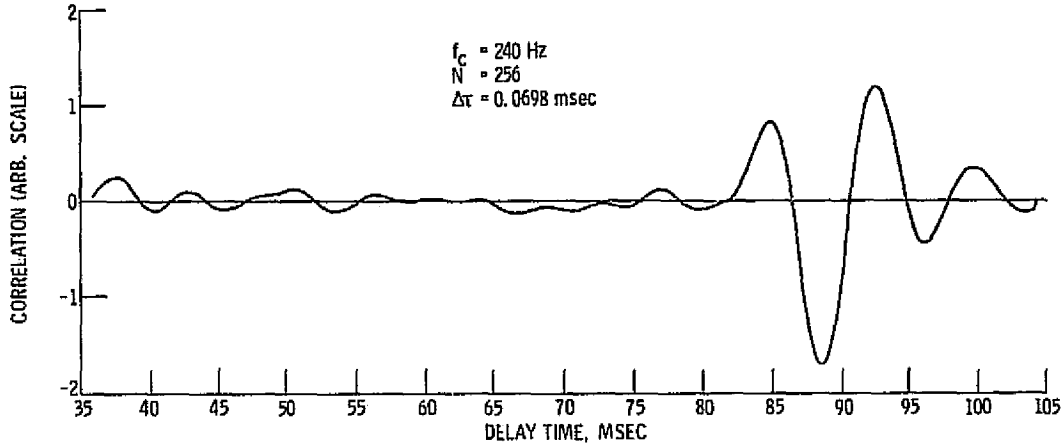

Figure 27. - Low-pass Filtered Cross-correlation Between Combustor Pressure And 120° Far-field Acoustic Pressure (43% Speed).

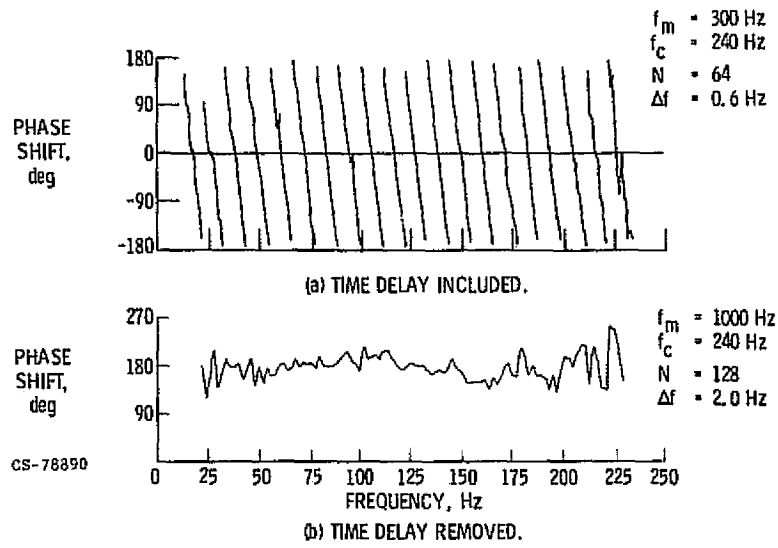

Figure 28. - Phase Shift Between Combustor Pressure and 120° Far-Field Acoustic Pressure (43% Speed).

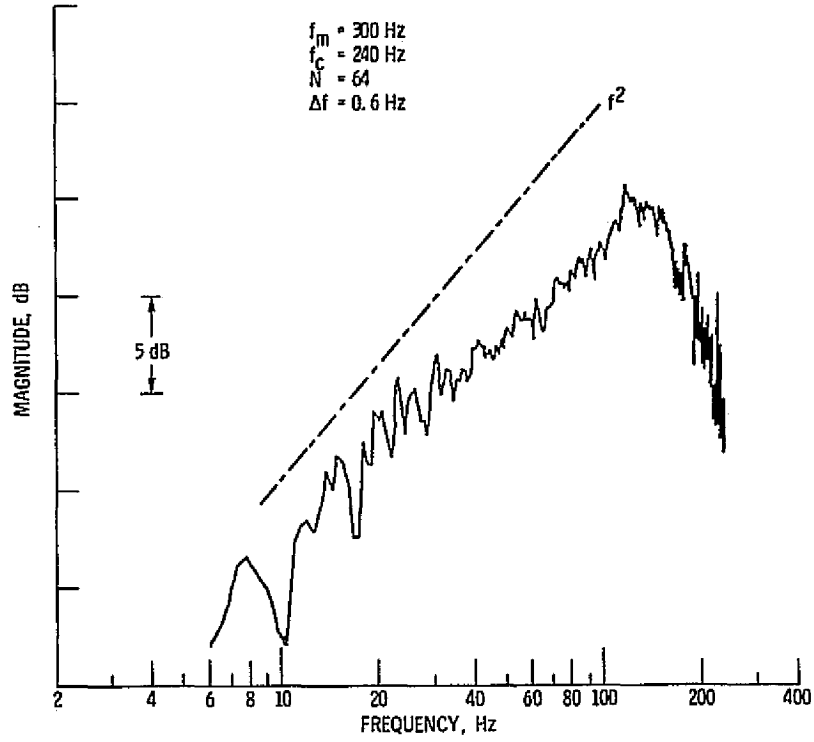

Figure 29. - Transfer Function Magnitude Between Combustor Pressure And 120° Far-field Acoustic Pressure (43% Speed).

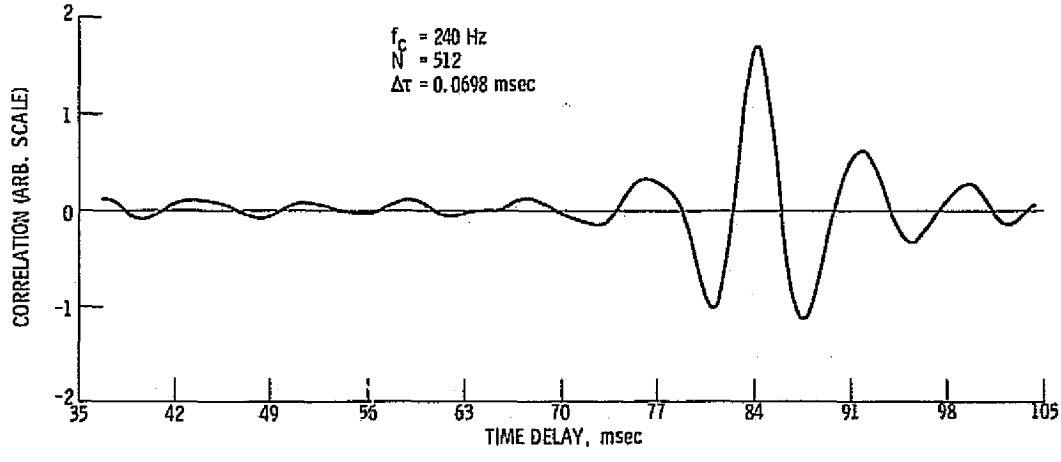

Figure 30. - Low Pass Filtered Cross-correlation Between Upstream Tailpipe Pressure and 120° Far-field Acoustic Pressure (43% Speed).

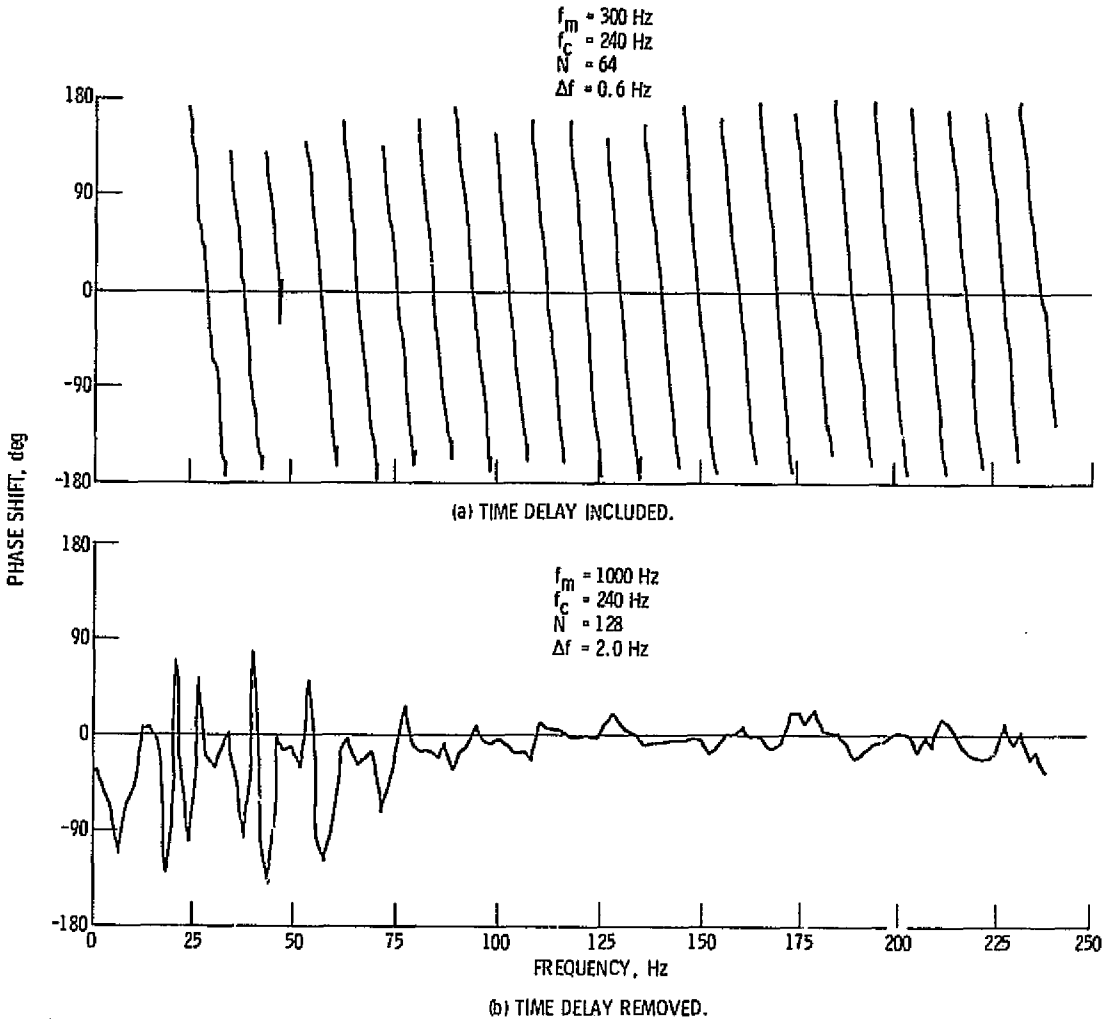

Figure 31. - Phase Shift Between Upstream Tailpipe Pressure And 120° Far-field Acoustic Pressure (43% Speed).

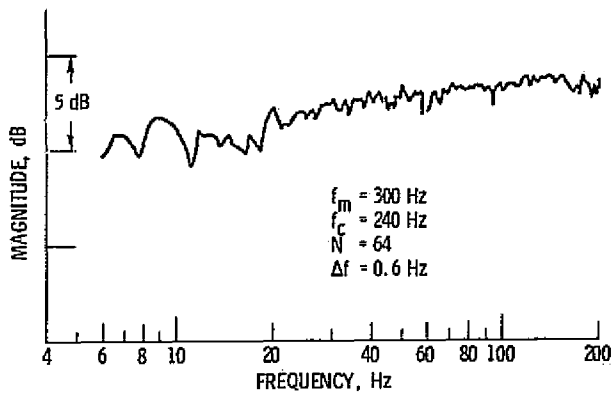

Figure 32. - Transfer Function Magnitude Between Upstream Tailpipe Pressure And 120° Far-field Acoustic Pressure (43% Speed).

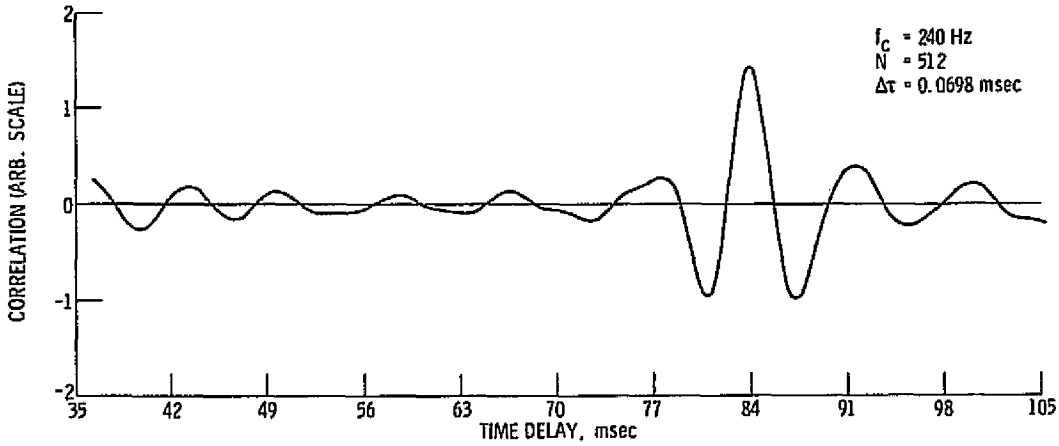

Figure 33. - Cross-correlation Between Downstream Tailpipe Pressure And 120° Far-field Acoustic Pressure (43% Speed).

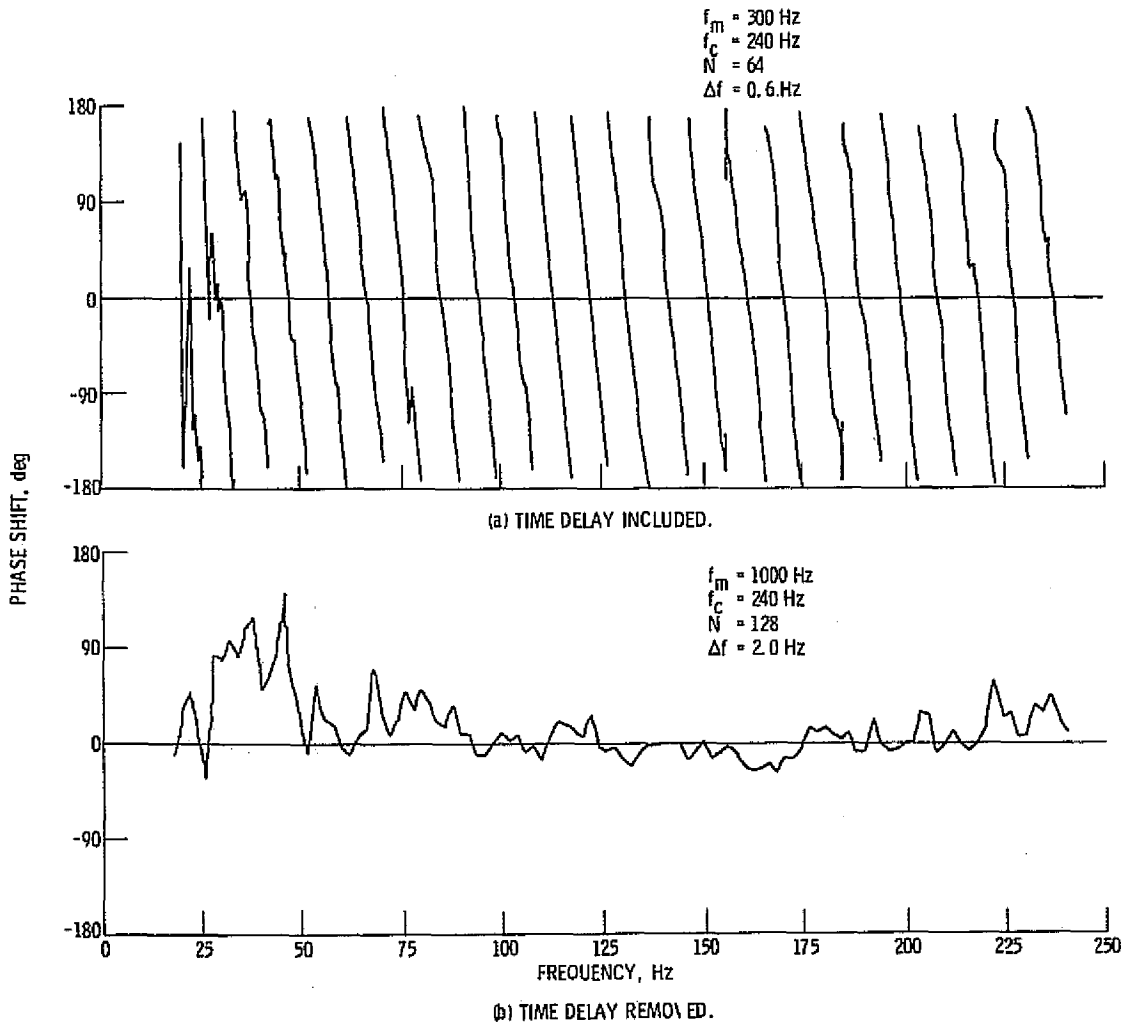

Figure 34. - Phase Shift Between Downstream Tailpipe Pressure And 120° Far-field Acoustic Pressure (43% Speed).

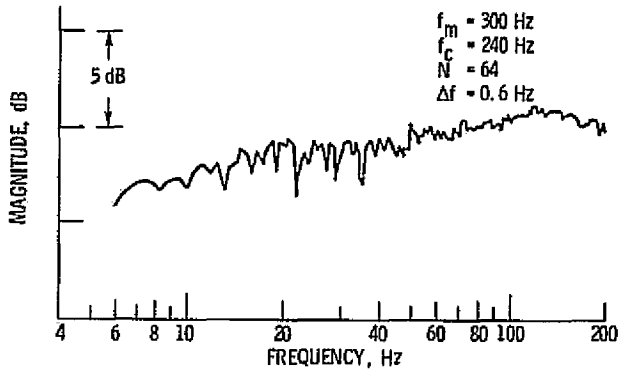

Figure 35. - Transfer Function Magnitude Between Downstream Tailpipe Pressure And 120° Far-field Acoustic Pressure (43% Speed).

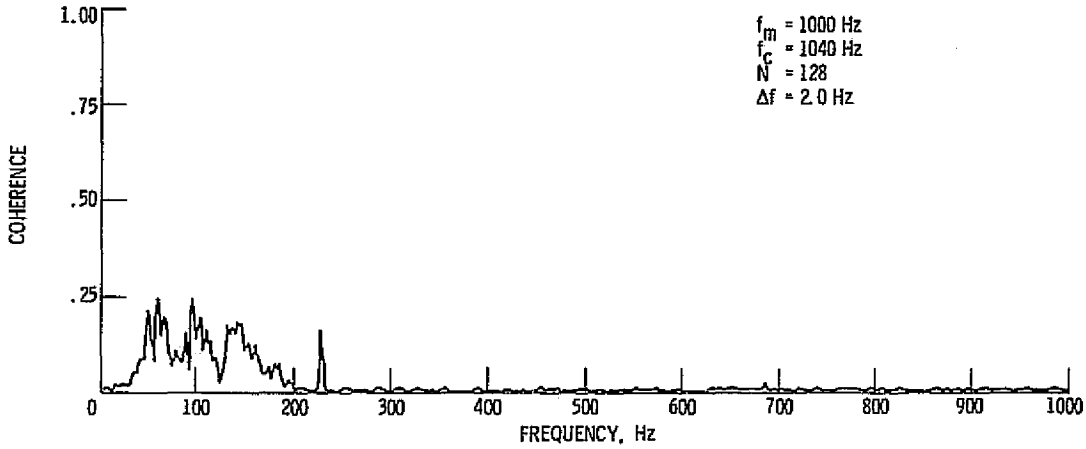

Figure 36. - Coherence Between Combustor Pressure And 60° Far-field Acoustic Pressure (43% Speed).

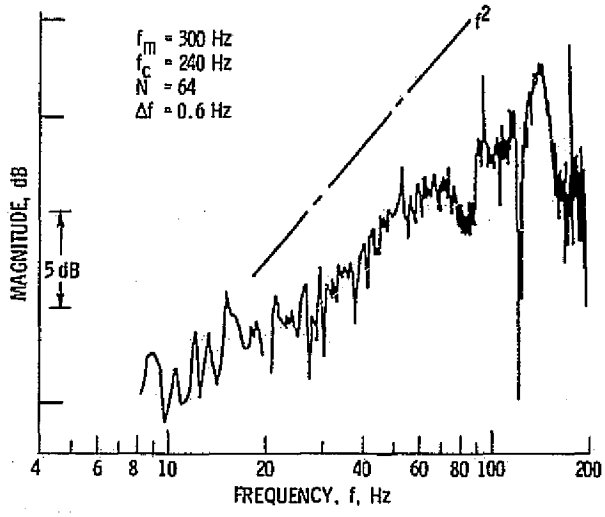

Figure 37. - Transfer Function Magnitude Between Combustor Pressure And 60° Far-field Acoustic Pressure (43% Speed).

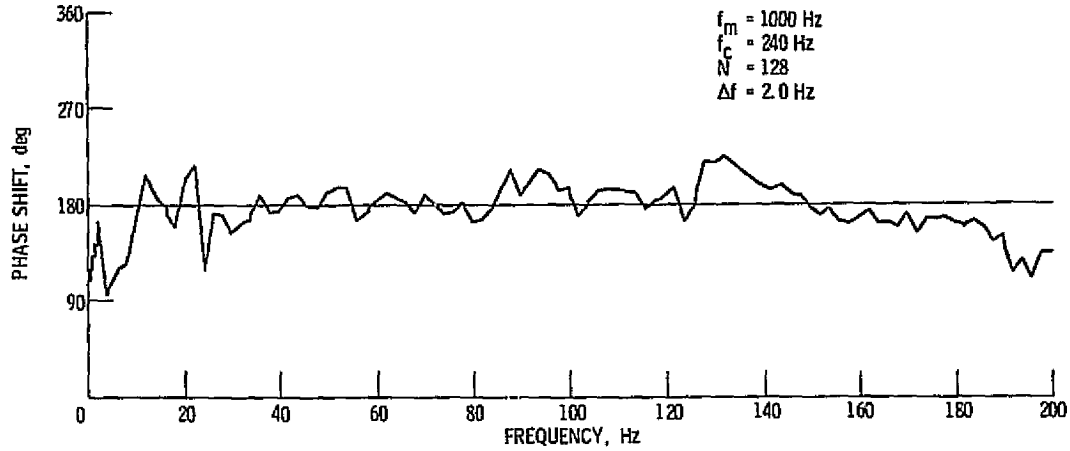

Figure 38. - Phase Shift Between Combustor Pressure And 60° Far-field Pressure, Time Delay Removed (43% Speed).

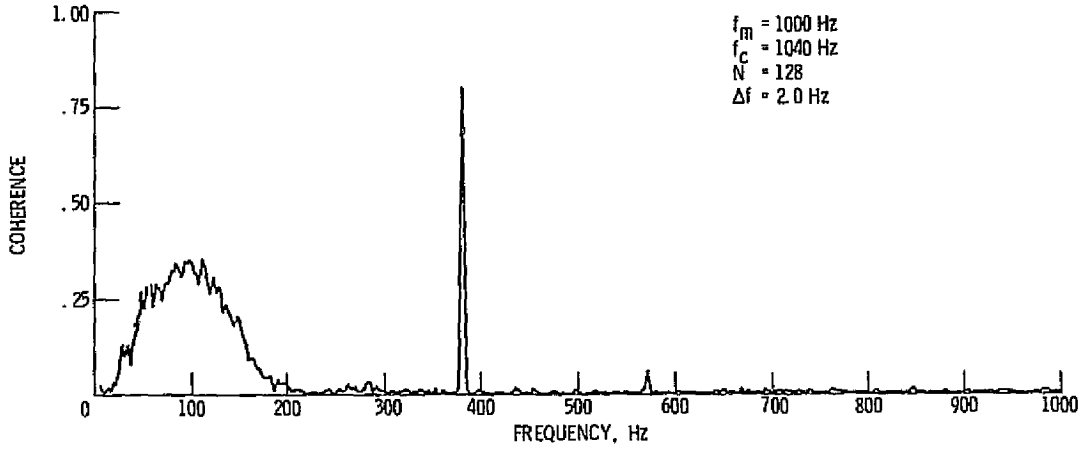

Figure 39. - Coherence Between Combustor Pressure And 120° Far-field Acoustic Pressure (30% Speed).

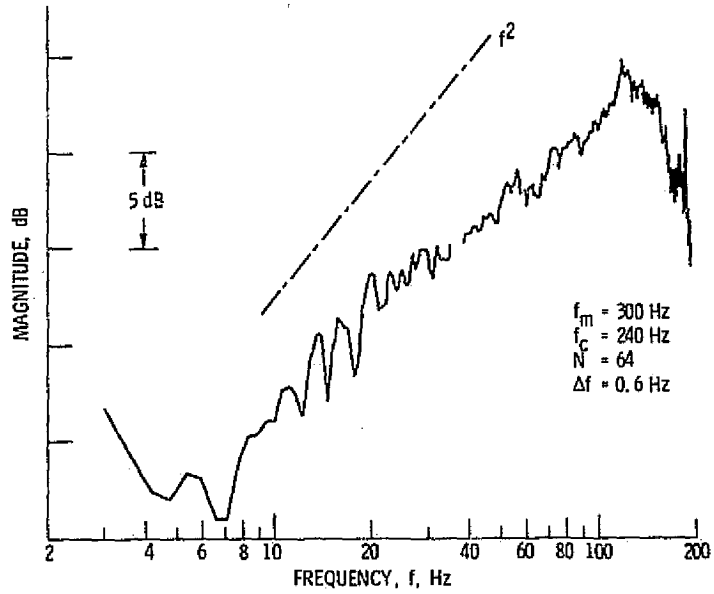

Figure 40. - Transfer Function Magnitude Between Combustor Pressure And 120° Far-field Acoustic Pressure (30% Speed).

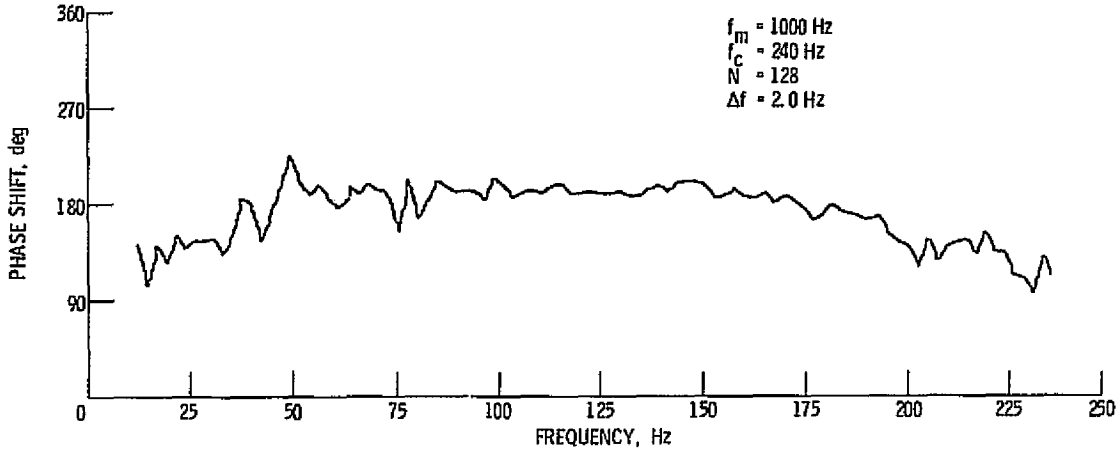

Figure 41. - Phase Shift Between Combustor Pressure and 120° Far-field Acoustic Pressure, Time Delay Removed (30% Speed).

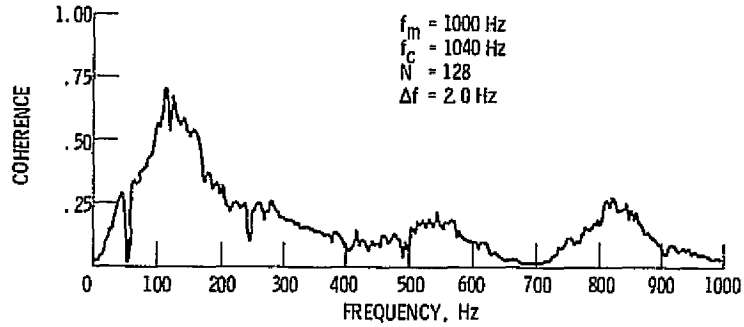

Figure 42. - Coherence Between Tailpipe Pressures (43% Speed).

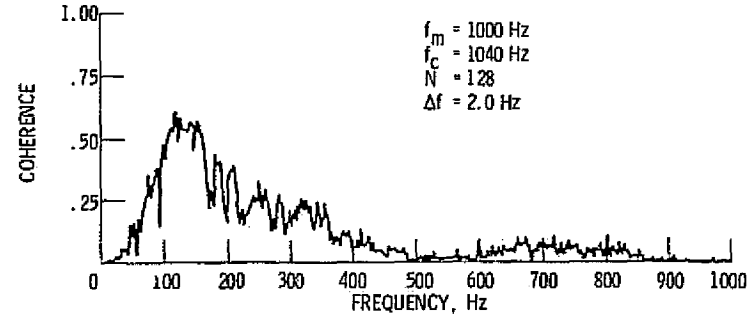

Figure 43. - Coherence Between Upstream Tailpipe Pressure And 120° Far-field Acoustic Pressure (43% Speed).

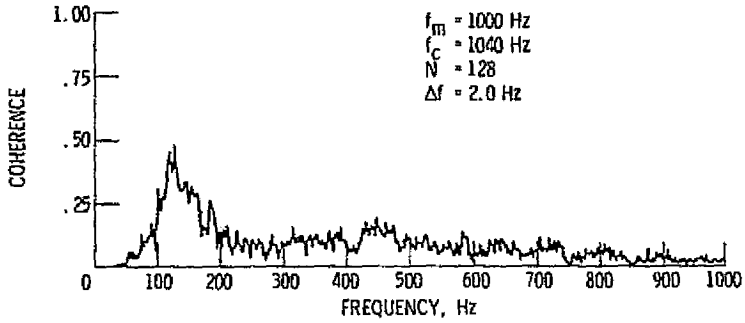

Figure 44. - Coherence Between Downstream Tailpipe Pressure And 120° Far-field Acoustic Pressure (43% Speed).

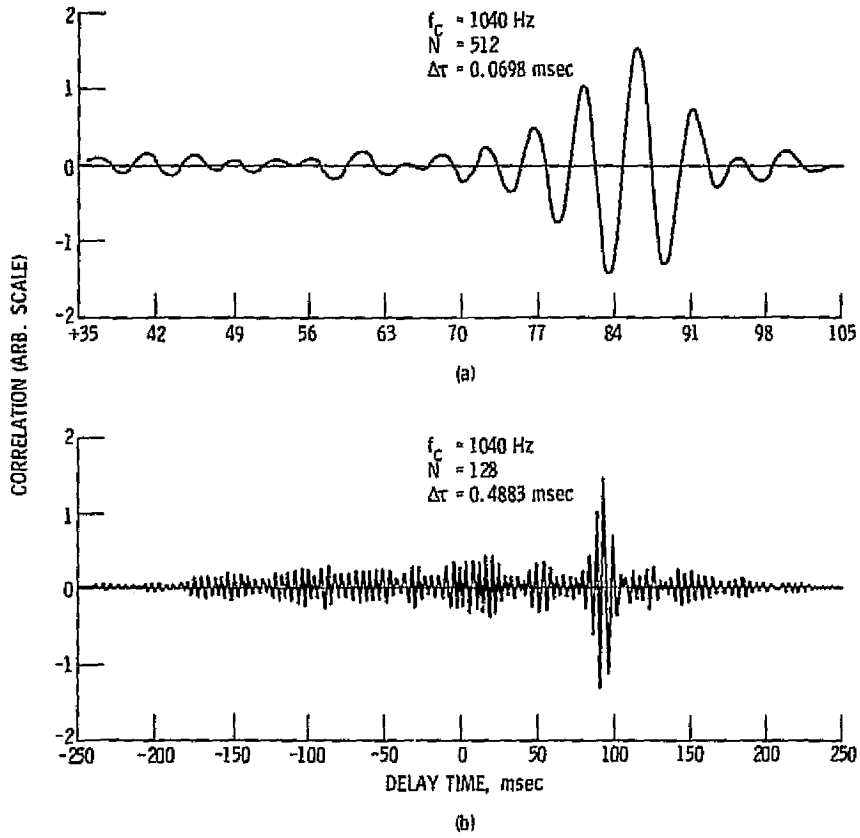

Figure 45. - Band-pass Filtered Cross-correlation Between Downstream Tailpipe Pressure And 120° Far-field Acoustic Pressure, 250 - 1040 Hz (43% Speed).

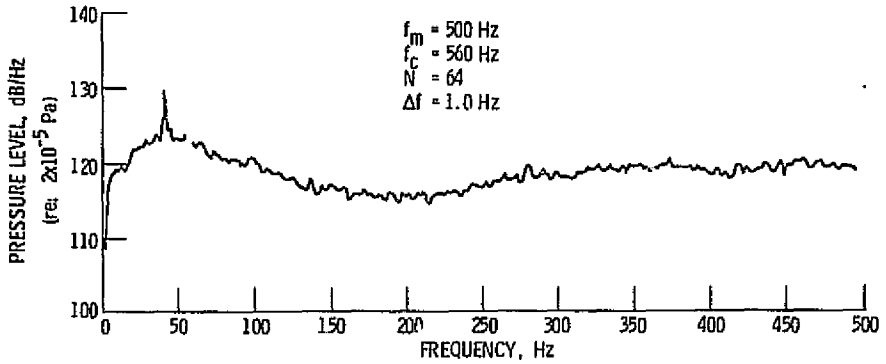

Figure 46. - Combustor Pressure Level Spectrum, 43% Speed.

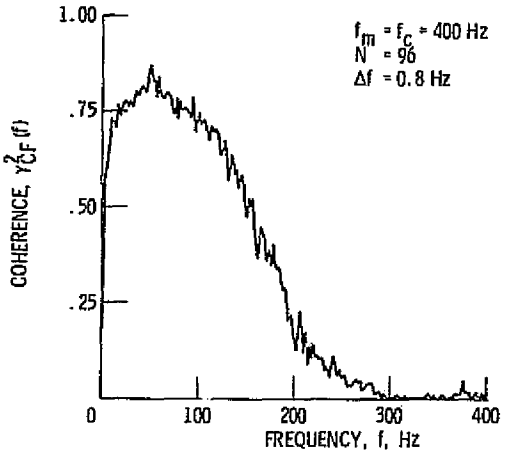

Figure 47. - Coherence Between Combustor Pressures; 90^0 Azimuthal Separation (43% Speed).

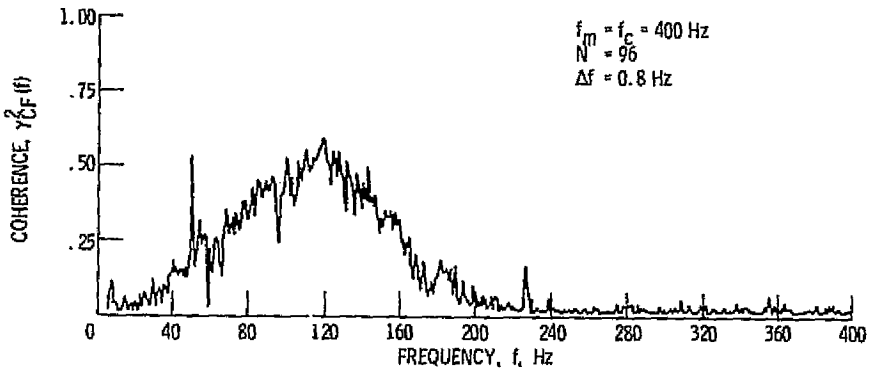

Figure 48. - Coherence Between Combustor Pressure And 120° Far-field Acoustic Pressure (43% Speed).

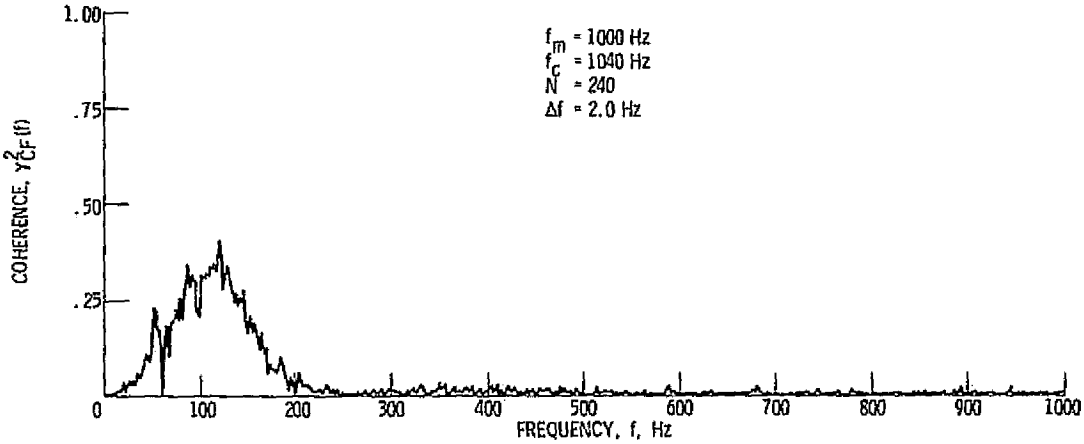

Figure 49. - Coherence Between Out-Of-Line Combustor Pressure And 120° Far-field Acoustic Pressure (43% Speed).

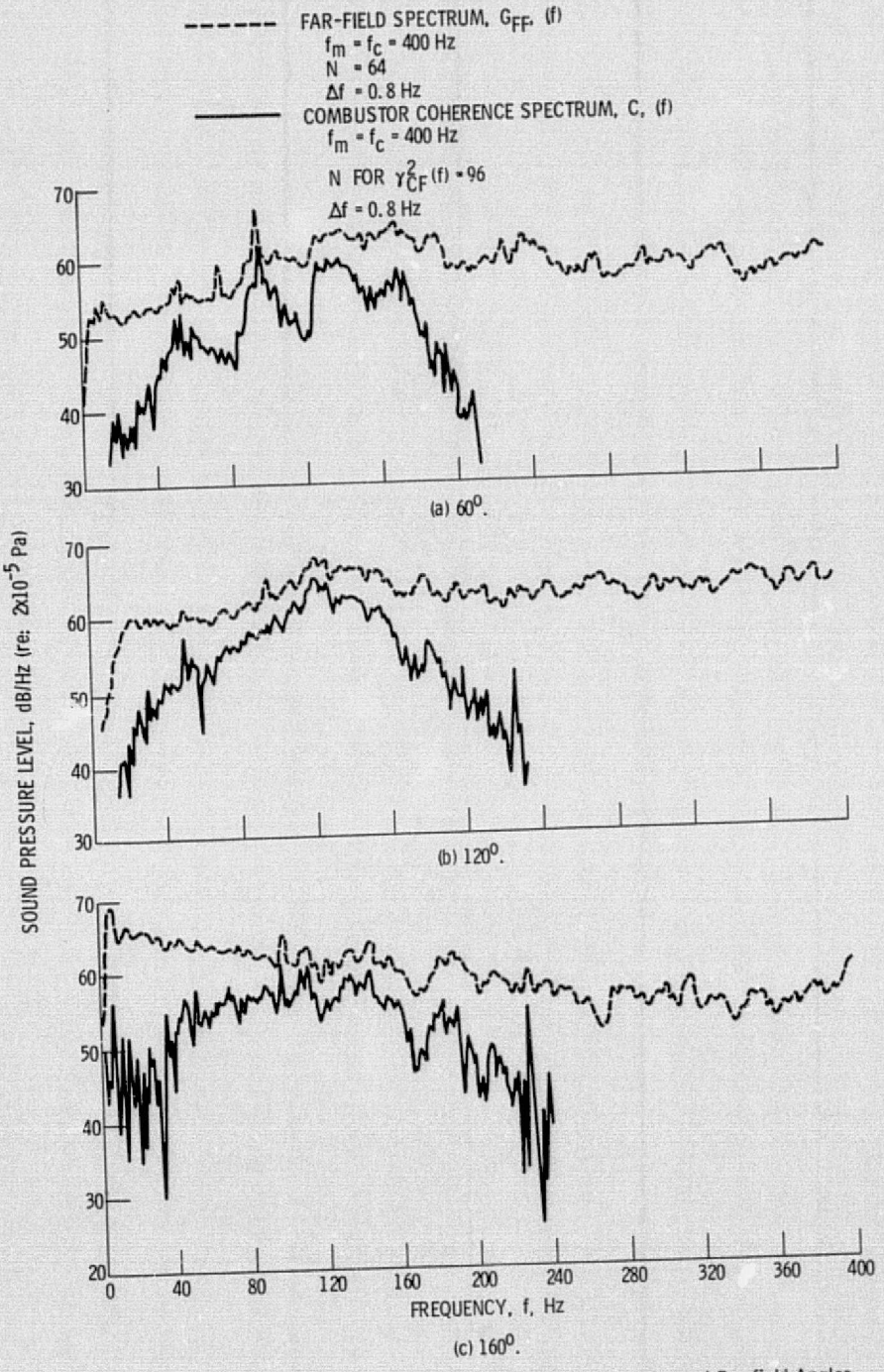

Figure 50. - Far-field And Combustor Coherence Spectra For Several Far-field Angles (43% Speed).

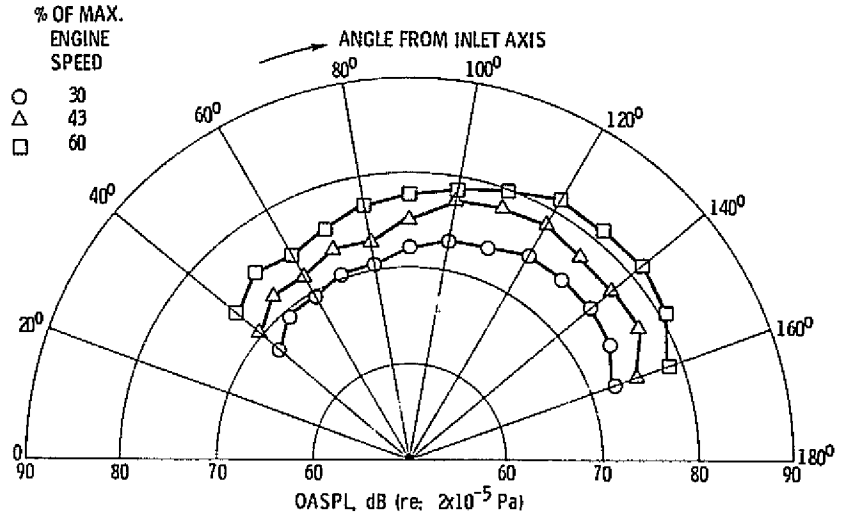

Figure 51. - OASPL Combustion Noise Directivity Patterns For Several Operating Speeds.

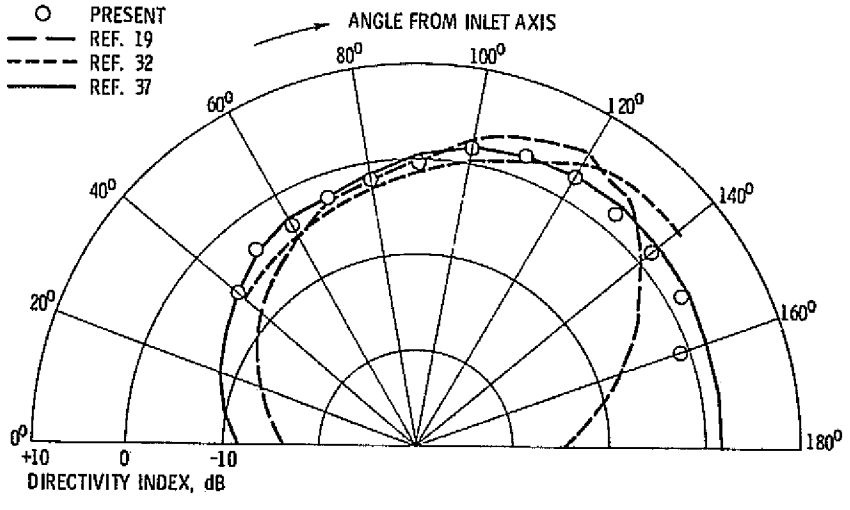

Figure 52. - Combustion Noise Directivity Index.

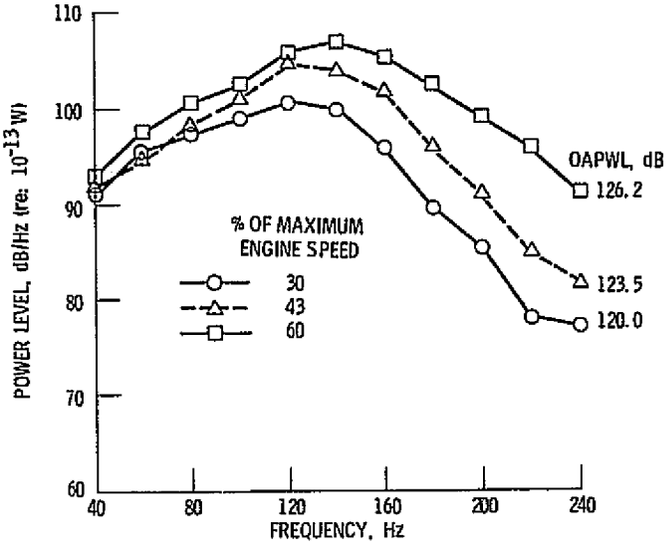

Figure 53. - Combustion Noise Power Level For Several Operating Speeds.

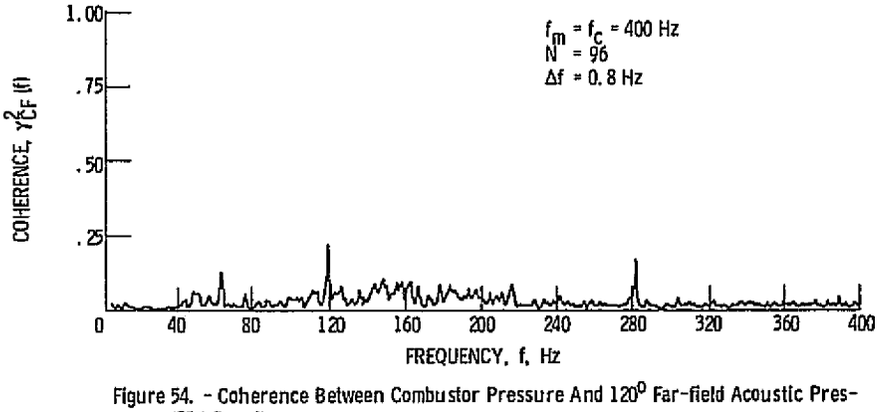

Figure 54. - Coherence Between Combustor Pressure And 120° Far-field Acoustic Pressure (75% Speed).

APPENDIX A

STATISTICAL CONSIDERATIONS

The purpose of this appendix is to discuss some of the statistical uncertainties in the data presented in this study. These statistical errors are an inevitable byproduct of random data analysis techniques and, for the most part, cannot be entirely eliminated from the resulting data.

Computational Scheme

The digital signal processor used to obtain the results presented in this study digitized each sample record of data into 1024 words at a sampling rate 2.048 times the highest frequency (f_m) selected for analysis:

$$f_{sample} = 2.048\ f_m$$

The processor memory period, or sample record length, therefore, is:

$$T = \frac{\text{Number of words/record}}{\text{Number of words/sec}}$$

$$= 1024/(2.048\ f_m) = 500/f_m,\ \text{sec/record} \qquad \text{(A1)}$$

Since the number of words/record is fixed, the resolution bandwidth is

$$B_e = 1/T = f_m/500$$

The number of statistical degrees of freedom per sample record, therefore is (ref. 26)

$$n = 2B_eT = 2(f_m/500)(500/f_m) = 2 \tag{A2}$$

So, if N disjoint (i.e., independent) sample records are averaged, the total number of statistical degrees of freedom in the average is

$$n_{tot} = 2N \tag{A3}$$

For a total tape record length of 120 seconds, the maximum number of independent sample records is

$$N = 120/T \tag{A4}$$

Bias Error Due to Time Delay

In the usual analysis of signal pairs, the similarities, or mutual properties between the two signals do not coincide with one another until some time period has elapsed. In the present investigation, of course, this is the acoustic propagation time between the combustor and the far-field, which was shown in chapter 4 to be about 87 msec.

As pointed out in reference 30, failure to account for this time delay leads to a bias error in the coherence function, which becomes underestimated. The best procedure to eliminate or minimize this bias error is to delay the signal which occurs earlier in time, thus allowing the later signal to "catch up" before implementing any computation. The processor used to obtain the results shown in this paper, however, did not have such a precomputation delay feature when computing coherence functions. The bias error, therefore, was

calculated and the correction applied to the overall power levels. From (30), the bias error due to time delay is given by

$$\frac{\hat{\gamma}^2_{CF}(f)}{\gamma^2_{CF}(f)} = \left(1 - \frac{\tau}{T}\right)^2 \qquad \text{(A5)}$$

where

$\hat{\gamma}^2_{CF}(f)$ is the estimated (i.e., measured) value of the coherence function between combustor and far-field, at the frequency, f

$\gamma^2_{CF}(f)$ is the true value of the coherence function

τ is the delay time between the two signals

T is the processor memory period

It is obvious from (A5) that to minimize this bias error, T should be made as large as possible. From equations (A3) and (A4), however, to increase the number of statistical degrees of freedom, and therefore minimize random error (see below), T should be made as small as possible. Any selection of T, therefore, in computing the coherence function, represents a compromise. For the results shown in chapter 5, f_m was chosen at 400 Hz. So, from (A1),

$$T = 500/400 \text{ Hz} = 1.25 \text{ sec/record}$$

Substituting this into (A3)

$$\frac{\hat{\gamma}^2_{CF}(f)}{\gamma^2_{CF}(f)} = \left(1 - \frac{0.087}{1.25}\right)^2 = 0.866$$

The measured values of the coherence function, therefore, are about 87 percent of the true values. In terms of decibels, then,

this represents an error of about 10 log(1/0.866) = 0.6 dB. This amount was added to the overall combustor far-field power levels shown in figure 12 and in the appropriate column of table I, in the text.

Coherence Function Confidence Limits

Because of the finite sample length of the data, there are both variance and bias errors in the computation of the coherence functions.

The confidence limits on the coherence function estimate due to these errors may be calculated, to a close degree of approximation, from (ref. 38):

$$\tanh[w(f) - (n_{tot} - 2)^{-1}b(f) - \sigma_w Z_{\alpha/2}] < \gamma_{CF}(f) \leq \tanh[w(f) - (n_{tot} - 2)^{-1}b(f) + \sigma_w Z_{\alpha/2}] \qquad \text{(A6)}$$

where

$w(f) = \tanh^{-1}[\hat{\gamma}_{CF}(f)]$

n_{tot} = number of statistical degrees of freedom in the estimate = 2N

$b(f) = [\gamma_{CF}(f) + 1.1]/2[\gamma_{CF}(f) + 0.1]$

$\sigma_w = \sqrt{1/(n_{tot} - 2)}$

$Z_{\alpha/2}$ = the 100 $\alpha/2$ percentage point of the standardized normal probability distribution

Note from the above, that to solve for the confidence limits on the coherence function estimate, $\hat{\gamma}_{CF}(f)$, the true value, $\gamma_{CF}(f)$ must

be known. The procedure used here to calculate the confidence limits was to assume that the estimated value could be substituted for the true value in b(f). This is clearly adequate as long as

$$[w(f) \pm \sigma_w Z_{\alpha/2}](n - 2) >> b(f) \qquad \text{(A7)}$$

Furthermore, to produce a conservative result, the estimated values of $\hat{\gamma}^2_{CF}$ used in (A6) were those obtained before correcting for the time delay bias. (It should be noted that the number of statistical degrees of freedom in ref. 38 is exactly one-half the number used here. Care must be used, therefore, when comparing the equations of ref. 38 with those used here.)

Example: For 90 percent confidence limits, then $Z_{\alpha/2} = 1.645$ (see any table of the standardized normal probability distribution). For the present work with a 120 second taped record, and T = 1.25 seconds, then

$$N = 120/T = 120 \text{ sec}/1.25 \text{ sec} = 96$$

$$n_{tot} = 2(96) = 192$$

$$(n_{tot} - 2)^{-1} = 1/190 = 0.00526$$

$$\sigma_w = \sqrt{1/(n_{tot} - 2)} = 0.07267$$

For a measured coherence $\hat{\gamma}^2_{CF}(f)$ of, say, 0.5, we have:

$$w(f) = \tanh^{-1}(\sqrt{0.5}) = 0.881$$

$$b(f) = [\sqrt{0.5} + 1.1]/2[\sqrt{0.5} + 0.1] = 1.119$$

Substituting these into (A6), gives:

$$\tanh[0.881 - 0.00526(1.119) - 0.0726(1.645)] < \gamma_{CF}(f) \leq$$

$$\tanh[0.881 - 0.00526(1.119) + 0.0726(1.645)]$$

or,

$$0.407 < \gamma^2_{CF}(f) \leq 0.576$$

Or, in decibels, referenced to the estimate

$$-0.89 \text{ dB} < 10 \log \frac{\gamma^2_{CF}(f)}{\hat{\gamma}^2_{CF}(f)} \leq +0.61 \text{ dB}$$

So, for any measured coherence value of 0.5, the associated combustor coherence spectrum has a 90 percent confidence limit of about -0.9 dB to +0.6 dB just due to the uncertainty in $\hat{\gamma}^2_{CF}(f)$.

For lower values of the measured coherence function, the confidence limits are wider. For example, at a measured coherence of 0.1, calculations identical to the above produce 90 percent confidence limits of -4.1 dB to +2.3 dB. In both cases above, it can be verified that the inequality given by (A7) is satisfied.

Confidence Limits on Combustor Coherence Spectra and Power Spectra

The directivity and power results shown in this study were obtained by multiplying the measured coherence function by the far-field spectrum, on a frequency by frequency basis. The statistical errors in the coherence functions were described above. There also are, however, statistical errors associated with the far-field spectral estimate. These errors combine (though not in an additive fashion) with the errors in the coherence estimate to produce the

final error in the combustor coherence spectra. In reference 26, it is shown the variance error, ϵ_r, in spectral estimates obtained by FFT techniques such as used here is given by:

$$\epsilon_r[\hat{G}_{FF}(f)] = \sqrt{\frac{2}{n_{tot}}}$$

where $\hat{G}_{FF}(f)$ is the far-field spectral estimate.

For the present case, N = 64 (the far-field spectra were computed independently, and the number of averages was required to be a power of 2 because of the FFT algorithm used by the DSP), so $n_{tot} = 128$. So, the error is approximately 12.5 percent, or about 0.5 dB. This error prevails throughout the spectral range because of the constant bandwidth. This is in contrast to an error band of at least 1.5 dB associated with the coherence function estimate. In reference 30, it is shown that for cases such as this, when one error is significantly larger than the other, the larger error dominates the final coherence spectrum estimate. With the assumption that the variance errors in the combustor coherence spectra are dominated by the variance errors in the coherence function, figure A1 shows a typical combustor coherence spectrum, with the associated 90 percent confidence limits sketched in. This figure is for an engine speed of 43 percent of maximum and a far-field microphone angle of 120°.

With the exception of several frequencies at the 60° far-field angle (see appendix C), the coherence functions between the fluctuating combustor pressure and the far-field acoustic pressure did not vary significantly in either magnitude or shape with respect to

far-field angle or engine speed. For this reason, the confidence limits on the combustor coherence spectra, as a function of frequency, were essentially the same at all far-field angles. The power spectra (fig. 53), therefore, which were obtained by a spacial integration of the combustor coherence spectra, have 90 percent confidence limits virtually identical to that of figure A1. The confidence limits on figure A1, consequently, are representative of all spectral results obtained in this investigation via the coherence function.

The bias errors in the far-field spectral estimates are proportional to the resolution bandwidth, which for this case has an effective value of 1 Hz. Because the far-field spectra were all smoothly varying (i.e., no tones), these bias errors may be considered negligible.

Confidence Limits on OASPL and OAWPL

From figure A1, the 90 percent confidence band on the coherence spectra and the power spectra are quite narrow at frequencies near the peak (approximately ±0.5 dB). This band broadens at frequencies away from the peak. At 40 Hz the 90 percent confidence limits are about -3 dB to +2 dB, and at 240 Hz the 90 percent confidence limits are about -10 dB to +4 dB. At these two extremes, however, the measured spectral levels are considerably below the levels at the peak. The large uncertainty band at the extremes of the spectra, therefore, do not greatly affect the overall levels,

which are obtained by anti-logarithmically summing the individual spectral levels at each frequency. For example, at the 120° far-field microphone angle, for an engine speed of 43 percent of maximum, the computed OASPL is 78 dB (fig. 51), with 90 percent confidence limits of -1.5 dB to +0.9 dB. Similar results prevail at all angles and operating conditions on figure 51. For the OAPWL at 43 percent operating speed, the computed value is 123.5 dB (fig. 53), with 90 percent confidence limits of -1.7 dB to +1.0 dB. Again, similar results prevail at the other operating speeds.

The possibility of random statistical error in the computation of the transfer function accounting for the reduced slope cannot be estimated since this requires knowledge of the absolute value of the measured function (26). Only the relative value is shown in figure 21. However, it does not seem likely that random error is responsible since all the measured transfer functions with respect to the combustor have slopes consistently somewhat less than 2.0.

Similar comments also apply to the phase results: the confidence limits on the phase spectra cannot be computed without an absolute numerical value of the transfer function. However, it is true that as the coherence is reduced, the variance of the phase estimate increases. This is likely the reason for the apparent random phase fluctuation seen at the low and high frequency limits of several of the time delay removed phase plots in Chapter 4.

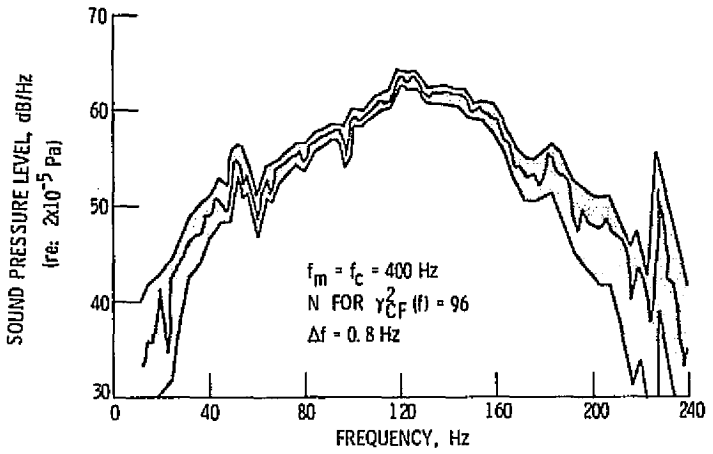

Figure A1. - 90% Confidence Limits For Combustor Coherence Spectrum At 120^0 Far-field Angle (43% Speed).

APPENDIX B

TABULATION OF COHERENCE FUNCTION CONFIDENCE LIMITS

This appendix contains a tabulation of the 90 percent confidence limits for ordinary coherence function estimates between 0.01 and 0.99. The confidence limits for a specified value of the measured coherence are tabulated as a function of the number of independent samples (N) averaged to obtain the estimate. The first set of tables is for the linear variable $\gamma^2(f)$. The second set of tables is in terms of decibels referenced to the measured value. This second set of tables may also be used to determine confidence limits on coherence spectra if the variance error in the spectral estimate is small compared to the error in the coherence estimate (see appendix A).

Equation (A6) was used to generate the tables for cases where the measured coherence is less than 0.75. For tabulated values of the measured coherence greater than 0.75, equation (A6) was used with b(f) set equal to unity (ref. 38). Blanked locations in the table indicate that either N or the measured coherence are too low for equation (A6) to be valid.

Table B-1. 90 Percent Confidence Limits on Coherence Function Measured with Average of N Samples

Measured coherence	N = 16	N = 32	N = 64	N = 128	N = 256	N = 512	N = 1024	N = 2048	N = 4096
.01					.000-.027	.002-.022	.004-.018	.005-.016	.007-.014
.02					.004-.043	.008-.036	.011-.031	.013-.028	.015-.025
.03				.004-.069	.009-.057	.015-.049	.019-.043	.022-.039	.024-.036
.04				.008-.083	.016-.070	.022-.061	.027-.055	.031-.050	.033-.047
.05			.004-.118	.013-.097	.022-.083	.030-.073	.035-.066	.039-.061	.042-.058
.06			.008-.132	.019-.111	.029-.095	.038-.085	.044-.077	.048-.072	.052-.069
.07			.012-.146	.025-.123	.037-.107	.046-.096	.053-.088	.058-.083	.061-.079
.08		.003-.192	.017-.160	.032-.136	.045-.119	.054-.108	.062-.099	.067-.094	.071-.090
.09		.005-.206	.022-.173	.039-.148	.052-.131	.063-.119	.071-.110	.076-.104	.080-.100
.10		.008-.220	.028-.185	.046-.160	.061-.142	.072-.130	.080-.121	.086-.115	.090-.110
.11		.012-.233	.033-.198	.053-.172	.069-.154	.080-.141	.089-.132	.095-.125	.099-.121
.12		.016-.246	.040-.210	.061-.184	.077-.165	.089-.152	.098-.142	.104-.136	.109-.131
.13		.020-.259	.046-.222	.069-.195	.086-.176	.098-.163	.107-.153	.114-.146	.119-.141
.14		.025-.271	.053-.234	.076-.207	.094-.187	.107-.173	.117-.164	.124-.157	.128-.152
.15	.003-.333	.030-.283	.060-.245	.085-.218	.103-.198	.117-.184	.126-.174	.133-.167	.138-.162
.16	.005-.345	.035-.295	.067-.257	.093-.229	.112-.209	.126-.195	.136-.184	.143-.177	.148-.172
.17	.008-.357	.041-.306	.075-.268	.101-.240	.121-.220	.135-.205	.145-.195	.152-.188	.158-.182
.18	.011-.369	.047-.318	.082-.279	.110-.251	.130-.230	.144-.216	.155-.205	.162-.198	.167-.193
.19	.014-.380	.053-.329	.090-.290	.118-.262	.139-.241	.154-.226	.164-.216	.172-.208	.177-.203
.20	.018-.392	.060-.340	.098-.301	.127-.272	.148-.251	.163-.237	.174-.226	.182-.218	.187-.213
.21	.022-.403	.066-.351	.106-.312	.136-.283	.157-.262	.173-.247	.184-.236	.191-.229	.197-.223
.22	.026-.413	.073-.362	.114-.323	.144-.293	.167-.272	.182-.257	.193-.246	.201-.239	.207-.233
.23	.031-.424	.080-.372	.122-.333	.153-.304	.176-.283	.192-.268	.203-.257	.211-.249	.217-.243
.24	.035-.435	.088-.383	.131-.344	.163-.314	.185-.293	.201-.278	.213-.267	.221-.259	.226-.253
.25	.041-.445	.095-.393	.139-.354	.172-.325	.195-.303	.211-.288	.223-.277	.231-.269	.236-.264
.26	.046-.455	.103-.404	.148-.364	.181-.335	.204-.314	.221-.298	.232-.287	.240-.279	.246-.274
.27	.052-.465	.111-.414	.157-.374	.190-.345	.214-.324	.230-.308	.242-.297	.250-.289	.256-.284
.28	.058-.475	.119-.424	.166-.385	.200-.355	.223-.334	.240-.318	.252-.307	.260-.299	.266-.294
.29	.064-.485	.127-.434	.175-.395	.209-.365	.233-.344	.250-.329	.262-.317	.270-.309	.276-.304
.30	.071-.494	.135-.444	.184-.405	.219-.375	.243-.354	.260-.339	.272-.327	.280-.320	.286-.314
.31	.077-.504	.144-.453	.193-.415	.228-.385	.253-.364	.270-.349	.282-.338	.290-.330	.296-.324
.32	.084-.513	.152-.463	.202-.424	.238-.395	.262-.374	.280-.359	.292-.348	.300-.340	.306-.334
.33	.092-.522	.161-.473	.212-.434	.248-.405	.272-.384	.290-.369	.302-.358	.310-.350	.316-.344
.34	.099-.531	.170-.482	.221-.444	.257-.415	.282-.394	.300-.379	.312-.367	.320-.360	.326-.354
.35	.107-.540	.179-.491	.231-.453	.267-.425	.292-.404	.309-.389	.322-.377	.330-.370	.336-.364
.36	.115-.549	.188-.501	.241-.463	.277-.435	.302-.414	.319-.398	.332-.387	.340-.379	.346-.374
.37	.123-.558	.198-.510	.251-.473	.287-.444	.312-.424	.330-.408	.342-.397	.350-.389	.356-.384
.38	.131-.567	.207-.519	.260-.482	.297-.454	.322-.433	.340-.418	.352-.407	.360-.399	.366-.394
.39	.139-.576	.217-.528	.270-.492	.307-.464	.332-.443	.350-.428	.362-.417	.370-.409	.376-.404
.40	.148-.584	.226-.537	.280-.501	.317-.473	.342-.453	.360-.438	.372-.427	.380-.419	.386-.414
.41	.157-.593	.238-.548	.292-.511	.328-.483	.353-.463	.370-.448	.382-.437	.390-.429	.396-.424
.42	.166-.601	.248-.557	.302-.520	.338-.493	.363-.472	.380-.458	.392-.447	.400-.439	.406-.434
.43	.175-.609	.258-.566	.312-.530	.348-.502	.373-.482	.390-.467	.402-.457	.410-.449	.416-.443
.44	.185-.618	.268-.575	.322-.539	.359-.512	.384-.492	.401-.477	.412-.466	.421-.459	.426-.453
.45	.195-.626	.279-.583	.333-.548	.369-.521	.394-.501	.411-.487	.423-.476	.431-.469	.436-.463
.46	.204-.634	.289-.592	.343-.557	.380-.530	.404-.511	.421-.496	.433-.486	.441-.479	.447-.473
.47	.215-.642	.300-.600	.354-.566	.390-.540	.415-.520	.431-.506	.443-.496	.451-.488	.457-.483
.48	.225-.650	.310-.609	.364-.575	.401-.549	.425-.530	.442-.516	.453-.506	.461-.498	.467-.493
.49	.235-.658	.321-.617	.375-.584	.411-.558	.435-.539	.452-.525	.463-.515	.471-.508	.477-.503
.50	.246-.666	.332-.626	.386-.593	.422-.568	.446-.549	.462-.535	.474-.525	.481-.518	.487-.513

Table B-1. Concluded.

Measured coherence	N = 16	N = 32	N = 64	N = 128	N = 256	N = 512	N = 1024	N = 2048	N = 4096
.51	.257-.673	.343-.634	.397-.602	.432-.577	.456-.558	.473-.545	.484-.535	.492-.528	.497-.523
.52	.268-.681	.354-.642	.408-.610	.443-.586	.467-.568	.483-.554	.494-.544	.502-.537	.507-.532
.53	.279-.689	.365-.651	.419-.619	.454-.595	.477-.577	.493-.564	.504-.554	.512-.547	.517-.542
.54	.290-.696	.376-.659	.430-.628	.465-.604	.488-.586	.504-.573	.515-.564	.522-.557	.528-.552
.55	.302-.704	.387-.667	.441-.637	.475-.613	.499-.596	.514-.583	.525-.574	.532-.567	.538-.562
.56	.313-.711	.399-.675	.452-.645	.486-.622	.509-.605	.525-.592	.535-.583	.543-.577	.548-.572
.57	.325-.719	.411-.683	.463-.654	.497-.631	.520-.614	.535-.602	.546-.593	.553-.586	.558-.582
.58	.337-.726	.422-.691	.474-.662	.508-.640	.530-.624	.546-.611	.556-.603	.563-.596	.568-.591
.59	.350-.734	.434-.699	.486-.671	.519-.649	.541-.633	.556-.621	.566-.612	.573-.606	.578-.601
.60	.362-.741	.446-.707	.497-.680	.530-.658	.552-.642	.567-.630	.577-.622	.584-.616	.589-.611
.61	.375-.748	.458-.715	.509-.688	.541-.667	.563-.652	.577-.640	.587-.631	.594-.625	.599-.621
.62	.387-.755	.470-.723	.520-.697	.552-.676	.573-.661	.588-.649	.598-.641	.604-.635	.609-.631
.63	.400-.762	.482-.731	.532-.705	.563-.685	.584-.670	.598-.659	.608-.651	.615-.645	.619-.640
.64	.413-.770	.494-.739	.543-.713	.575-.694	.595-.679	.609-.668	.618-.660	.625-.654	.629-.650
.65	.427-.777	.507-.747	.555-.722	.586-.703	.606-.688	.619-.678	.629-.670	.635-.664	.640-.660
.66	.440-.784	.519-.754	.567-.730	.597-.712	.617-.697	.630-.687	.639-.679	.645-.674	.650-.670
.67	.454-.791	.532-.762	.579-.739	.608-.720	.628-.707	.641-.696	.650-.689	.656-.684	.660-.680
.68	.467-.798	.545-.770	.591-.747	.620-.729	.639-.716	.651-.706	.660-.699	.666-.693	.670-.689
.69	.481-.804	.557-.777	.603-.755	.631-.738	.650-.725	.662-.715	.671-.708	.676-.703	.680-.699
.70	.496-.811	.570-.785	.615-.763	.642-.747	.661-.734	.673-.725	.681-.718	.687-.713	.691-.709
.71	.510-.818	.583-.792	.627-.772	.654-.755	.672-.743	.683-.734	.692-.727	.697-.722	.701-.719
.72	.524-.825	.596-.800	.639-.780	.665-.764	.683-.752	.694-.743	.702-.737	.707-.732	.711-.728
.73	.539-.831	.610-.808	.651-.788	.677-.773	.694-.761	.705-.752	.713-.746	.718-.742	.721-.738
.74	.554-.838	.623-.815	.663-.796	.688-.781	.705-.770	.716-.762	.723-.756	.728-.751	.732-.748
.75	.569-.845	.636-.822	.675-.804	.700-.790	.716-.779	.726-.771	.734-.765	.739-.761	.742-.758
.76	.584-.851	.650-.830	.688-.812	.712-.799	.727-.788	.737-.780	.744-.775	.749-.770	.752-.767
.77	.599-.858	.663-.837	.700-.820	.723-.807	.738-.797	.748-.790	.755-.784	.759-.780	.763-.777
.78	.615-.864	.677-.845	.713-.828	.735-.816	.749-.806	.759-.799	.765-.794	.770-.790	.773-.787
.79	.631-.871	.690-.852	.725-.836	.747-.824	.760-.815	.770-.808	.776-.803	.780-.799	.783-.797
.80	.646-.877	.704-.859	.738-.844	.758-.833	.772-.824	.780-.817	.786-.812	.791-.809	.793-.806
.81	.662-.884	.718-.867	.750-.852	.770-.841	.783-.833	.791-.827	.797-.822	.801-.819	.804-.816
.82	.679-.890	.732-.874	.763-.860	.782-.850	.794-.842	.802-.836	.808-.831	.811-.828	.814-.826
.83	.695-.897	.746-.881	.776-.868	.794-.858	.805-.851	.813-.845	.818-.841	.822-.838	.824-.836
.84	.712-.903	.761-.888	.789-.876	.806-.867	.817-.860	.824-.854	.829-.850	.832-.847	.835-.845
.85	.728-.909	.775-.895	.801-.884	.818-.875	.828-.868	.835-.863	.839-.860	.843-.857	.845-.855
.86	.745-.915	.789-.903	.814-.892	.830-.884	.839-.877	.846-.873	.850-.869	.853-.866	.855-.865
.87	.762-.922	.804-.910	.827-.900	.841-.892	.851-.886	.857-.882	.861-.878	.864-.876	.865-.874
.88	.780-.928	.818-.917	.840-.908	.853-.901	.862-.895	.868-.891	.871-.888	.874-.886	.876-.884
.89	.797-.934	.833-.924	.853-.915	.866-.909	.873-.904	.879-.900	.882-.897	.884-.895	.886-.894
.90	.815-.940	.848-.931	.866-.923	.878-.917	.885-.913	.890-.909	.893-.907	.895-.905	.896-.903
.91	.832-.946	.862-.938	.879-.931	.890-.926	.896-.921	.901-.918	.903-.916	.905-.914	.907-.913
.92	.850-.952	.877-.945	.893-.939	.902-.934	.908-.930	.912-.927	.914-.925	.916-.924	.917-.923
.93	.868-.958	.892-.952	.906-.946	.914-.942	.919-.939	.923-.937	.925-.935	.926-.933	.927-.932
.94	.887-.964	.908-.959	.919-.954	.926-.951	.931-.948	.934-.946	.936-.944	.937-.943	.938-.942
.95	.905-.970	.923-.966	.933-.962	.938-.959	.942-.956	.945-.955	.946-.953	.947-.952	.948-.952
.96	.924-.976	.938-.973	.946-.970	.951-.967	.954-.965	.956-.964	.957-.963	.958-.962	.959-.961
.97	.943-.982	.953-.979	.959-.977	.963-.975	.965-.974	.967-.973	.968-.972	.968-.971	.969-.971
.98	.961-.988	.969-.986	.973-.985	.975-.984	.977-.983	.978-.982	.978-.981	.979-.981	.979-.981
.99	.981-.994	.984-.993	.986-.992	.988-.992	.988-.991	.989-.991	.989-.991	.989-.990	.990-.990

Table B-2. 90 Percent Confidence Limits on Coherent Output Power Spectrum Computed Via

Coherence Function Measured with Average of N Samples (Decibels)

Measured coherence	N = 16	N = 32	N = 64	N = 128	N = 256	N = 512	N = 1024	N = 2048	N = 4096
.01					-13.3/+ 4.4	-6.8/+ 3.4	-4.1/+ 2.6	-2.6/+ 1.9	-1.8/+ 1.4
.02					-6.8/+ 3.3	-4.1/+ 2.5	-2.6/+ 1.9	-1.8/+ 1.4	-1.2/+ 1.0
.03				-8.9/+ 3.6	-5.0/+ 2.8	-3.1/+ 2.1	-2.1/+ 1.6	-1.4/+ 1.1	-1.0/+ 0.8
.04				-6.9/+ 3.2	-4.1/+ 2.4	-2.6/+ 1.8	-1.7/+ 1.4	-1.2/+ 1.0	-0.8/+ 0.7
.05			-10.8/+ 3.7	-5.7/+ 2.9	-3.5/+ 2.2	-2.3/+ 1.6	-1.5/+ 1.2	-1.0/+ 0.9	-0.7/+ 0.6
.06			-8.9/+ 3.4	-5.0/+ 2.7	-3.1/+ 2.0	-2.0/+ 1.5	-1.4/+ 1.1	-0.9/+ 0.8	-0.6/+ 0.6
.07			-7.7/+ 3.2	-4.4/+ 2.5	-2.8/+ 1.9	-1.8/+ 1.4	-1.2/+ 1.0	-0.8/+ 0.7	-0.6/+ 0.5
.08			-6.8/+ 3.0	-4.0/+ 2.3	-2.5/+ 1.7	-1.7/+ 1.3	-1.1/+ 0.9	-0.8/+ 0.7	-0.5/+ 0.5
.09		-12.4/+ 3.6	-6.1/+ 2.8	-3.7/+ 2.2	-2.3/+ 1.6	-1.6/+ 1.2	-1.1/+ 0.9	-0.7/+ 0.6	-0.5/+ 0.5
.10		-10.8/+ 3.4	-5.6/+ 2.7	-3.4/+ 2.0	-2.2/+ 1.5	-1.4/+ 1.1	-1.0/+ 0.8	-0.7/+ 0.6	-0.5/+ 0.4
.11		-9.7/+ 3.3	-5.2/+ 2.5	-3.2/+ 1.9	-2.0/+ 1.5	-1.4/+ 1.1	-0.9/+ 0.8	-0.6/+ 0.6	-0.4/+ 0.4
.12		-8.8/+ 3.1	-4.8/+ 2.4	-3.0/+ 1.8	-1.9/+ 1.4	-1.3/+ 1.0	-0.9/+ 0.7	-0.6/+ 0.5	-0.4/+ 0.4
.13		-8.1/+ 3.0	-4.5/+ 2.3	-2.8/+ 1.8	-1.8/+ 1.3	-1.2/+ 1.0	-0.8/+ 0.7	-0.6/+ 0.5	-0.4/+ 0.4
.14		-7.5/+ 2.9	-4.2/+ 2.2	-2.6/+ 1.7	-1.7/+ 1.3	-1.2/+ 0.9	-0.8/+ 0.7	-0.5/+ 0.5	-0.4/+ 0.3
.15	-16.6/+ 3.5	-7.0/+ 2.8	-4.0/+ 2.1	-2.5/+ 1.6	-1.6/+ 1.2	-1.1/+ 0.9	-0.7/+ 0.6	-0.5/+ 0.5	-0.4/+ 0.3
.16	-14.8/+ 3.3	-6.5/+ 2.7	-3.8/+ 2.1	-2.4/+ 1.6	-1.6/+ 1.2	-1.0/+ 0.9	-0.7/+ 0.6	-0.5/+ 0.4	-0.3/+ 0.3
.17	-13.4/+ 3.2	-6.2/+ 2.6	-3.6/+ 2.0	-2.3/+ 1.5	-1.5/+ 1.1	-1.0/+ 0.8	-0.7/+ 0.6	-0.5/+ 0.4	-0.3/+ 0.3
.18	-12.2/+ 3.1	-5.8/+ 2.5	-3.4/+ 1.9	-2.2/+ 1.4	-1.4/+ 1.1	-1.0/+ 0.8	-0.7/+ 0.6	-0.5/+ 0.4	-0.3/+ 0.3
.19	-11.3/+ 3.0	-5.5/+ 2.4	-3.3/+ 1.8	-2.1/+ 1.4	-1.4/+ 1.0	-0.9/+ 0.8	-0.6/+ 0.5	-0.4/+ 0.4	-0.3/+ 0.3
.20	-10.5/+ 2.9	-5.2/+ 2.3	-3.1/+ 1.8	-2.0/+ 1.3	-1.3/+ 1.0	-0.9/+ 0.7	-0.6/+ 0.5	-0.4/+ 0.4	-0.3/+ 0.3
.21	-9.9/+ 2.8	-5.0/+ 2.2	-3.0/+ 1.7	-1.9/+ 1.3	-1.3/+ 1.0	-0.9/+ 0.7	-0.6/+ 0.5	-0.4/+ 0.4	-0.3/+ 0.3
.22	-9.3/+ 2.7	-4.8/+ 2.2	-2.9/+ 1.7	-1.8/+ 1.3	-1.2/+ 0.9	-0.8/+ 0.7	-0.6/+ 0.5	-0.4/+ 0.4	-0.3/+ 0.3
.23	-8.8/+ 2.7	-4.6/+ 2.1	-2.7/+ 1.6	-1.8/+ 1.2	-1.2/+ 0.9	-0.8/+ 0.7	-0.5/+ 0.5	-0.4/+ 0.3	-0.3/+ 0.2
.24	-8.3/+ 2.6	-4.4/+ 2.0	-2.6/+ 1.6	-1.7/+ 1.2	-1.1/+ 0.9	-0.8/+ 0.6	-0.5/+ 0.5	-0.4/+ 0.3	-0.3/+ 0.2
.25	-7.9/+ 2.5	-4.2/+ 2.0	-2.5/+ 1.5	-1.6/+ 1.1	-1.1/+ 0.8	-0.7/+ 0.6	-0.5/+ 0.4	-0.4/+ 0.3	-0.2/+ 0.2
.26	-7.5/+ 2.4	-4.0/+ 1.9	-2.4/+ 1.5	-1.6/+ 1.1	-1.0/+ 0.8	-0.7/+ 0.6	-0.5/+ 0.4	-0.3/+ 0.3	-0.2/+ 0.2
.27	-7.2/+ 2.4	-3.9/+ 1.9	-2.4/+ 1.4	-1.5/+ 1.1	-1.0/+ 0.8	-0.7/+ 0.6	-0.5/+ 0.4	-0.3/+ 0.3	-0.2/+ 0.2
.28	-6.8/+ 2.3	-3.7/+ 1.8	-2.3/+ 1.4	-1.5/+ 1.0	-1.0/+ 0.8	-0.7/+ 0.6	-0.5/+ 0.4	-0.3/+ 0.3	-0.2/+ 0.2
.29	-6.6/+ 2.2	-3.6/+ 1.7	-2.2/+ 1.3	-1.4/+ 1.0	-0.9/+ 0.7	-0.6/+ 0.5	-0.4/+ 0.4	-0.3/+ 0.3	-0.2/+ 0.2
.30	-6.3/+ 2.2	-3.5/+ 1.7	-2.1/+ 1.3	-1.4/+ 1.0	-0.9/+ 0.7	-0.6/+ 0.5	-0.4/+ 0.4	-0.3/+ 0.3	-0.2/+ 0.2
.31	-6.0/+ 2.1	-3.3/+ 1.7	-2.1/+ 1.3	-1.3/+ 0.9	-0.9/+ 0.7	-0.6/+ 0.5	-0.4/+ 0.4	-0.3/+ 0.3	-0.2/+ 0.2
.32	-5.8/+ 2.0	-3.2/+ 1.6	-2.0/+ 1.2	-1.3/+ 0.9	-0.9/+ 0.7	-0.6/+ 0.5	-0.4/+ 0.4	-0.3/+ 0.3	-0.2/+ 0.2
.33	-5.6/+ 2.0	-3.1/+ 1.6	-1.9/+ 1.2	-1.2/+ 0.9	-0.8/+ 0.7	-0.6/+ 0.5	-0.4/+ 0.3	-0.3/+ 0.2	-0.2/+ 0.2
.34	-5.4/+ 1.9	-3.0/+ 1.5	-1.9/+ 1.2	-1.2/+ 0.9	-0.8/+ 0.6	-0.6/+ 0.5	-0.4/+ 0.3	-0.3/+ 0.2	-0.2/+ 0.2
.35	-5.2/+ 1.9	-2.9/+ 1.5	-1.8/+ 1.1	-1.2/+ 0.8	-0.8/+ 0.6	-0.5/+ 0.5	-0.4/+ 0.3	-0.3/+ 0.2	-0.2/+ 0.2
.36	-5.0/+ 1.8	-2.8/+ 1.4	-1.7/+ 1.1	-1.1/+ 0.8	-0.8/+ 0.6	-0.5/+ 0.4	-0.4/+ 0.3	-0.2/+ 0.2	-0.2/+ 0.2
.37	-4.8/+ 1.8	-2.7/+ 1.4	-1.7/+ 1.1	-1.1/+ 0.8	-0.7/+ 0.6	-0.5/+ 0.4	-0.3/+ 0.3	-0.2/+ 0.2	-0.2/+ 0.2
.38	-4.6/+ 1.7	-2.6/+ 1.4	-1.6/+ 1.0	-1.1/+ 0.8	-0.7/+ 0.6	-0.5/+ 0.4	-0.3/+ 0.3	-0.2/+ 0.2	-0.2/+ 0.2
.39	-4.5/+ 1.7	-2.6/+ 1.3	-1.6/+ 1.0	-1.0/+ 0.8	-0.7/+ 0.6	-0.5/+ 0.4	-0.3/+ 0.3	-0.2/+ 0.2	-0.2/+ 0.1
.40	-4.3/+ 1.6	-2.5/+ 1.3	-1.5/+ 1.0	-1.0/+ 0.7	-0.7/+ 0.5	-0.5/+ 0.4	-0.3/+ 0.3	-0.2/+ 0.2	-0.2/+ 0.1
.41	-4.2/+ 1.6	-2.4/+ 1.3	-1.5/+ 1.0	-1.0/+ 0.7	-0.7/+ 0.5	-0.4/+ 0.4	-0.3/+ 0.3	-0.2/+ 0.2	-0.1/+ 0.1
.42	-4.0/+ 1.6	-2.3/+ 1.2	-1.4/+ 0.9	-0.9/+ 0.7	-0.6/+ 0.5	-0.4/+ 0.4	-0.3/+ 0.3	-0.2/+ 0.2	-0.1/+ 0.1
.43	-3.9/+ 1.5	-2.2/+ 1.2	-1.4/+ 0.9	-0.9/+ 0.7	-0.6/+ 0.5	-0.4/+ 0.4	-0.3/+ 0.3	-0.2/+ 0.2	-0.1/+ 0.1
.44	-3.8/+ 1.5	-2.1/+ 1.2	-1.4/+ 0.9	-0.9/+ 0.7	-0.6/+ 0.5	-0.4/+ 0.4	-0.3/+ 0.3	-0.2/+ 0.2	-0.1/+ 0.1
.45	-3.6/+ 1.4	-2.1/+ 1.1	-1.3/+ 0.9	-0.9/+ 0.6	-0.6/+ 0.5	-0.4/+ 0.3	-0.3/+ 0.2	-0.2/+ 0.2	-0.1/+ 0.1
.46	-3.5/+ 1.4	-2.0/+ 1.1	-1.3/+ 0.8	-0.8/+ 0.6	-0.6/+ 0.5	-0.4/+ 0.3	-0.3/+ 0.2	-0.2/+ 0.2	-0.1/+ 0.1
.47	-3.4/+ 1.4	-2.0/+ 1.1	-1.2/+ 0.8	-0.8/+ 0.6	-0.5/+ 0.4	-0.4/+ 0.3	-0.3/+ 0.2	-0.2/+ 0.2	-0.1/+ 0.1
.48	-3.3/+ 1.3	-1.9/+ 1.0	-1.2/+ 0.8	-0.8/+ 0.6	-0.5/+ 0.4	-0.4/+ 0.3	-0.3/+ 0.2	-0.2/+ 0.2	-0.1/+ 0.1
.49	-3.2/+ 1.3	-1.8/+ 1.0	-1.2/+ 0.8	-0.8/+ 0.6	-0.5/+ 0.4	-0.4/+ 0.3	-0.2/+ 0.2	-0.2/+ 0.2	-0.1/+ 0.1
.50	-3.1/+ 1.2	-1.8/+ 1.0	-1.1/+ 0.7	-0.7/+ 0.6	-0.5/+ 0.4	-0.3/+ 0.3	-0.2/+ 0.2	-0.2/+ 0.2	-0.1/+ 0.1

Table B-2. Concluded.

Measured coherence	N = 16	N = 32	N = 64	N = 128	N = 256	N = 512	N = 1024	N = 2048	N = 4096
.51	-3.0/+ 1.2	-1.7/+ 0.9	-1.1/+ 0.7	-0.7/+ 0.5	-0.5/+ 0.4	-0.3/+ 0.3	-0.2/+ 0.2	-0.2/+ 0.1	-0.1/+ 0.1
.52	-2.9/+ 1.2	-1.7/+ 0.9	-1.1/+ 0.7	-0.7/+ 0.5	-0.5/+ 0.4	-0.3/+ 0.3	-0.2/+ 0.2	-0.2/+ 0.1	-0.1/+ 0.1
.53	-2.8/+ 1.1	-1.6/+ 0.9	-1.0/+ 0.7	-0.7/+ 0.5	-0.5/+ 0.4	-0.3/+ 0.3	-0.2/+ 0.2	-0.1/+ 0.1	-0.1/+ 0.1
.54	-2.7/+ 1.1	-1.6/+ 0.9	-1.0/+ 0.7	-0.7/+ 0.5	-0.4/+ 0.4	-0.3/+ 0.3	-0.2/+ 0.2	-0.1/+ 0.1	-0.1/+ 0.1
.55	-2.6/+ 1.1	-1.5/+ 0.8	-1.0/+ 0.6	-0.6/+ 0.5	-0.4/+ 0.3	-0.3/+ 0.3	-0.2/+ 0.2	-0.1/+ 0.1	-0.1/+ 0.1
.56	-2.5/+ 1.0	-1.5/+ 0.8	-0.9/+ 0.6	-0.6/+ 0.5	-0.4/+ 0.3	-0.3/+ 0.2	-0.2/+ 0.2	-0.1/+ 0.1	-0.1/+ 0.1
.57	-2.4/+ 1.0	-1.4/+ 0.8	-0.9/+ 0.6	-0.6/+ 0.4	-0.4/+ 0.3	-0.3/+ 0.2	-0.2/+ 0.2	-0.1/+ 0.1	-0.1/+ 0.1
.58	-2.4/+ 1.0	-1.4/+ 0.8	-0.9/+ 0.6	-0.6/+ 0.4	-0.4/+ 0.3	-0.3/+ 0.2	-0.2/+ 0.2	-0.1/+ 0.1	-0.1/+ 0.1
.59	-2.3/+ 0.9	-1.3/+ 0.7	-0.8/+ 0.6	-0.6/+ 0.4	-0.4/+ 0.3	-0.3/+ 0.2	-0.2/+ 0.2	-0.1/+ 0.1	-0.1/+ 0.1
.60	-2.2/+ 0.9	-1.3/+ 0.7	-0.8/+ 0.5	-0.5/+ 0.4	-0.4/+ 0.3	-0.2/+ 0.2	-0.2/+ 0.2	-0.1/+ 0.1	-0.1/+ 0.1
.61	-2.1/+ 0.9	-1.2/+ 0.7	-0.8/+ 0.5	-0.5/+ 0.4	-0.4/+ 0.3	-0.2/+ 0.2	-0.2/+ 0.2	-0.1/+ 0.1	-0.1/+ 0.1
.62	-2.0/+ 0.9	-1.2/+ 0.7	-0.8/+ 0.5	-0.5/+ 0.4	-0.3/+ 0.3	-0.2/+ 0.2	-0.2/+ 0.1	-0.1/+ 0.1	-0.1/+ 0.1
.63	-2.0/+ 0.8	-1.2/+ 0.6	-0.7/+ 0.5	-0.5/+ 0.4	-0.3/+ 0.3	-0.2/+ 0.2	-0.2/+ 0.1	-0.1/+ 0.1	-0.1/+ 0.1
.64	-1.9/+ 0.8	-1.1/+ 0.6	-0.7/+ 0.5	-0.5/+ 0.4	-0.3/+ 0.3	-0.2/+ 0.2	-0.1/+ 0.1	-0.1/+ 0.1	-0.1/+ 0.1
.65	-1.8/+ 0.8	-1.1/+ 0.6	-0.7/+ 0.5	-0.5/+ 0.3	-0.3/+ 0.2	-0.2/+ 0.2	-0.1/+ 0.1	-0.1/+ 0.1	-0.1/+ 0.1
.66	-1.8/+ 0.7	-1.0/+ 0.6	-0.7/+ 0.4	-0.4/+ 0.3	-0.3/+ 0.2	-0.2/+ 0.2	-0.1/+ 0.1	-0.1/+ 0.1	-0.1/+ 0.1
.67	-1.7/+ 0.7	-1.0/+ 0.6	-0.6/+ 0.4	-0.4/+ 0.3	-0.3/+ 0.2	-0.2/+ 0.2	-0.1/+ 0.1	-0.1/+ 0.1	-0.1/+ 0.1
.68	-1.6/+ 0.7	-1.0/+ 0.5	-0.6/+ 0.4	-0.4/+ 0.3	-0.3/+ 0.2	-0.2/+ 0.2	-0.1/+ 0.1	-0.1/+ 0.1	-0.1/+ 0.1
.69	-1.6/+ 0.7	-0.9/+ 0.5	-0.6/+ 0.4	-0.4/+ 0.3	-0.3/+ 0.2	-0.2/+ 0.2	-0.1/+ 0.1	-0.1/+ 0.1	-0.1/+ 0.1
.70	-1.5/+ 0.6	-0.9/+ 0.5	-0.6/+ 0.4	-0.4/+ 0.3	-0.3/+ 0.2	-0.2/+ 0.1	-0.1/+ 0.1	-0.1/+ 0.1	-0.1/+ 0.1
.71	-1.4/+ 0.6	-0.9/+ 0.5	-0.5/+ 0.4	-0.4/+ 0.3	-0.2/+ 0.2	-0.2/+ 0.1	-0.1/+ 0.1	-0.1/+ 0.1	-0.1/+ 0.1
.72	-1.4/+ 0.6	-0.8/+ 0.5	-0.5/+ 0.3	-0.3/+ 0.3	-0.2/+ 0.2	-0.2/+ 0.1	-0.1/+ 0.1	-0.1/+ 0.1	-0.1/+ 0.1
.73	-1.3/+ 0.6	-0.8/+ 0.4	-0.5/+ 0.3	-0.3/+ 0.2	-0.2/+ 0.2	-0.2/+ 0.1	-0.1/+ 0.1	-0.1/+ 0.1	-0.1/+ 0.0
.74	-1.3/+ 0.5	-0.7/+ 0.4	-0.5/+ 0.3	-0.3/+ 0.2	-0.2/+ 0.2	-0.1/+ 0.1	-0.1/+ 0.1	-0.1/+ 0.1	-0.0/+ 0.0
.75	-1.2/+ 0.5	-0.7/+ 0.4	-0.5/+ 0.3	-0.3/+ 0.2	-0.2/+ 0.2	-0.1/+ 0.1	-0.1/+ 0.1	-0.1/+ 0.1	-0.0/+ 0.0
.76	-1.1/+ 0.5	-0.7/+ 0.4	-0.4/+ 0.3	-0.3/+ 0.2	-0.2/+ 0.2	-0.1/+ 0.1	-0.1/+ 0.1	-0.1/+ 0.1	-0.0/+ 0.0
.77	-1.1/+ 0.5	-0.6/+ 0.4	-0.4/+ 0.3	-0.3/+ 0.2	-0.2/+ 0.2	-0.1/+ 0.1	-0.1/+ 0.1	-0.1/+ 0.1	-0.0/+ 0.0
.78	-1.0/+ 0.4	-0.6/+ 0.3	-0.4/+ 0.3	-0.3/+ 0.2	-0.2/+ 0.1	-0.1/+ 0.1	-0.1/+ 0.1	-0.1/+ 0.1	-0.0/+ 0.0
.79	-1.0/+ 0.4	-0.6/+ 0.3	-0.4/+ 0.2	-0.2/+ 0.2	-0.2/+ 0.1	-0.1/+ 0.1	-0.1/+ 0.1	-0.1/+ 0.1	-0.0/+ 0.0
.80	-0.9/+ 0.4	-0.6/+ 0.3	-0.4/+ 0.2	-0.2/+ 0.2	-0.2/+ 0.1	-0.1/+ 0.1	-0.1/+ 0.1	-0.0/+ 0.0	-0.0/+ 0.0
.81	-0.9/+ 0.4	-0.5/+ 0.3	-0.3/+ 0.2	-0.2/+ 0.2	-0.1/+ 0.1	-0.1/+ 0.1	-0.1/+ 0.1	-0.0/+ 0.0	-0.0/+ 0.0
.82	-0.8/+ 0.4	-0.5/+ 0.3	-0.3/+ 0.2	-0.2/+ 0.2	-0.1/+ 0.1	-0.1/+ 0.1	-0.1/+ 0.1	-0.0/+ 0.0	-0.0/+ 0.0
.83	-0.8/+ 0.3	-0.5/+ 0.3	-0.3/+ 0.2	-0.2/+ 0.1	-0.1/+ 0.1	-0.1/+ 0.1	-0.1/+ 0.1	-0.0/+ 0.0	-0.0/+ 0.0
.84	-0.7/+ 0.3	-0.4/+ 0.2	-0.3/+ 0.2	-0.2/+ 0.1	-0.1/+ 0.1	-0.1/+ 0.1	-0.1/+ 0.1	-0.0/+ 0.0	-0.0/+ 0.0
.85	-0.7/+ 0.3	-0.4/+ 0.2	-0.3/+ 0.2	-0.2/+ 0.1	-0.1/+ 0.1	-0.1/+ 0.1	-0.1/+ 0.0	-0.0/+ 0.0	-0.0/+ 0.0
.86	-0.6/+ 0.3	-0.4/+ 0.2	-0.2/+ 0.2	-0.2/+ 0.1	-0.1/+ 0.1	-0.1/+ 0.1	-0.1/+ 0.0	-0.0/+ 0.0	-0.0/+ 0.0
.87	-0.6/+ 0.3	-0.3/+ 0.2	-0.2/+ 0.1	-0.1/+ 0.1	-0.1/+ 0.1	-0.1/+ 0.1	-0.0/+ 0.0	-0.0/+ 0.0	-0.0/+ 0.0
.88	-0.5/+ 0.2	-0.3/+ 0.2	-0.2/+ 0.1	-0.1/+ 0.1	-0.1/+ 0.1	-0.1/+ 0.1	-0.0/+ 0.0	-0.0/+ 0.0	-0.0/+ 0.0
.89	-0.5/+ 0.2	-0.3/+ 0.2	-0.2/+ 0.1	-0.1/+ 0.1	-0.1/+ 0.1	-0.1/+ 0.0	-0.0/+ 0.0	-0.0/+ 0.0	-0.0/+ 0.0
.90	-0.4/+ 0.2	-0.3/+ 0.1	-0.2/+ 0.1	-0.1/+ 0.1	-0.1/+ 0.1	-0.1/+ 0.0	-0.0/+ 0.0	-0.0/+ 0.0	-0.0/+ 0.0
.91	-0.4/+ 0.2	-0.2/+ 0.1	-0.1/+ 0.1	-0.1/+ 0.1	-0.1/+ 0.1	-0.0/+ 0.0	-0.0/+ 0.0	-0.0/+ 0.0	-0.0/+ 0.0
.92	-0.3/+ 0.2	-0.2/+ 0.1	-0.1/+ 0.1	-0.1/+ 0.1	-0.1/+ 0.0	-0.0/+ 0.0	-0.0/+ 0.0	-0.0/+ 0.0	-0.0/+ 0.0
.93	-0.3/+ 0.1	-0.2/+ 0.1	-0.1/+ 0.1	-0.1/+ 0.1	-0.1/+ 0.0	-0.0/+ 0.0	-0.0/+ 0.0	-0.0/+ 0.0	-0.0/+ 0.0
.94	-0.3/+ 0.1	-0.2/+ 0.1	-0.1/+ 0.1	-0.1/+ 0.0	-0.0/+ 0.0	-0.0/+ 0.0	-0.0/+ 0.0	-0.0/+ 0.0	-0.0/+ 0.0
.95	-0.2/+ 0.1	-0.1/+ 0.1	-0.1/+ 0.1	-0.1/+ 0.0	-0.0/+ 0.0	-0.0/+ 0.0	-0.0/+ 0.0	-0.0/+ 0.0	-0.0/+ 0.0
.96	-0.2/+ 0.1	-0.1/+ 0.1	-0.1/+ 0.0	-0.0/+ 0.0	-0.0/+ 0.0	-0.0/+ 0.0	-0.0/+ 0.0	-0.0/+ 0.0	-0.0/+ 0.0
.97	-0.1/+ 0.1	-0.1/+ 0.0	-0.0/+ 0.0	-0.0/+ 0.0	-0.0/+ 0.0	-0.0/+ 0.0	-0.0/+ 0.0	-0.0/+ 0.0	-0.0/+ 0.0
.98	-0.1/+ 0.0	-0.0/+ 0.0	-0.0/+ 0.0	-0.0/+ 0.0	-0.0/+ 0.0	-0.0/+ 0.0	-0.0/+ 0.0	-0.0/+ 0.0	-0.0/+ 0.0
.99	-0.0/+ 0.0	-0.0/+ 0.0	-0.0/+ 0.0	-0.0/+ 0.0	-0.0/+ 0.0	-0.0/+ 0.0	-0.0/+ 0.0	-0.0/+ 0.0	-0.0/+ 0.0

APPENDIX C

DIRECTIVITY PATTERN FOR SEVERAL FREQUENCIES

In chapter 5 it was shown that the OASPL combustion directivities as obtained from the coherence functions agreed reasonably well with those of most previous studies. The directivity patterns were relatively uniform, with a slight peak near 120° (relative to the engine inlet axis). The same was not true, however, for certain frequencies. The coherence function at 43 percent engine speed between combustor pressure and the far-field acoustic pressure at the 60° microphone angle was shown in figure 36 and was seen to have several pronounced dips at frequencies of 40, 80, 120, and 160 Hz. The corresponding coherence spectrum was shown in figure 50(a) and, because of the relatively flat far-field spectrum at this angle, also contained dips at these frequencies. These dips gradually disappeared at angles away from 60°. The result, however, is an unusual directivity pattern at these frequencies, and this is shown in figure C1. In addition to the peak near 120°, there is now a 7 to 10 dB drop at 60°. Similar results were found for these same frequencies at all engine operating speeds through 60 percent. This dip does not show up in the OASPL directivity, of course, because of the logarithmic addition associated with obtaining an OASPL.

There are several possible reasons for this result. The first of these simply involves the presence of a noise source at these

frequencies which does not correlate with the combustor pressures. Such an extraneous noise source, however, would have to be highly directional (i.e., radiating strongly only at the 60° angle) and this seems quite inconsistent with the low frequencies involved.

It is also possible that the combustion noise is radiating from both aft and front ends of the engine, arriving at the 60° microphone out of phase, resulting in a partial cancellation. This saturation may arise from the time delay difference between the forward traveling acoustic waves (the speed of which is diminished by the gas flow speed within the engine) and the rearward traveling acoustic waves (the speed of which is augmented by the gas flow speed within the engine). Additionally, the plane of the bellmouth inlet is at a different distance from the 60° microphone than is the exit plane of the primary nozzle. The combined difference in propagation time may be sufficient to introduce a phase shift at the 60° microphone which results in cancellation. Such a situation, however, would obviously have to prevail only at the frequencies in question.

Finally, we are left with the possibility of some unusual phasing relationship at 60° between casing radiation (i.e., the engine as a unit vibrating) and direct acoustic radiation from the aft end. The highest frequency in question (200 Hz) has a corresponding wavelength of about 1.7 meters. This is certainly not large in comparison with the length of the engine, which is approximately 3.75 meters long. Phasing between casing radiation and aft-end radiation to produce a partial cancellation of 60° is, therefore, quite possible. Again, however, this phenomenon would have to be restricted

only to those frequencies in question.

The final remark to be made in this appendix, therefore, is simply that no definite conclusions can be reached regarding the dip in the directivity pattern which occur only at very specific frequencies, independent of engine operating speed. Precisely the same results were observed when the tests were rerun about 10 days later. The possibility, therefore, of an isolated anomalous test arena or environmental condition may be ruled out.

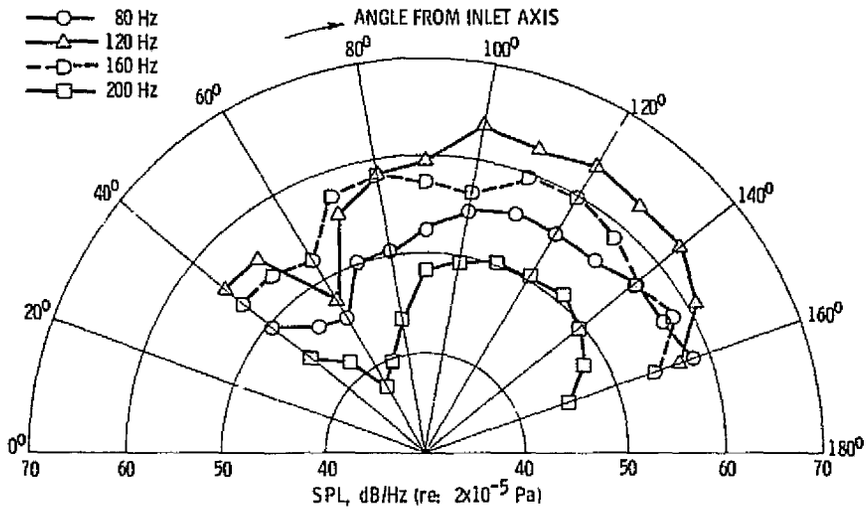

Figure C-1. - Directivity Pattern Of Combustion Noise For Several Frequencies.

APPENDIX D

FOURIER ANALYSIS OF RANDOM SIGNALS

The purpose of this appendix is to provide a brief review of the various frequency and time domain representations of random signals. It is intended primarily as background information for the reader not familiar with the techniques of random data analysis. Rigorous derivations and detailed interrelationships of the various functions used in the main body of this thesis, including digital computation techniques, may be found in numerous textbooks on the subject. Reference (26) is the primary source for most of the material presented in this appendix. The Fourier transform operation referred to here is understood to be the discrete, finite range Fourier transform described, for example, in ref. (26).

Auto-Spectral Density

Given a single realization of a random signal, say $x(t)$, then its Fourier transform $S_x(j\omega)$ will, in general, have a real and imaginary part:

$$S_x(j\omega) = \mathcal{F}[x(t)] = a(\omega) + jb(\omega) \qquad (j = \sqrt{-1})$$

where ω is the circular frequency.

The auto-spectral density of the signal $G_{xx}(\omega)$ may be approximated by:

$$G_{xx}(\omega) = S_x(j\omega)S_x^*(j\omega) = a^2(\omega) + b^2(\omega)$$

where the * signifies complex conjugate.

The auto-spectral density is a real-valued function, and is the quantity measured by conventional analog filtering procedures, as the filter bandwidth becomes very small.

The basic method for implementing this calculation digitally is as follows:

1. Record a sample of the signal
2. Do a Fourier transform of the data sample
3. Multiply the Fourier transform by its complex conjugate
4. Add this result to the previous sum of spectral densities
5. Repeat the sequence above N times
6. Divide the final result by N to obtain an ensemble averaged spectral density estimate

Note that because the signal is random, an estimate of the true spectral density is obtained by averaging the results of N ensembles. The spectral densities themselves must be averaged and not the Fourier transforms, since the real and imaginary parts would average to zero for a random signal.

Cross-Spectral Density

The cross-spectral density $G_{xy}(j\omega)$ between two signals, say $x(t)$ and $y(t)$, indicates similarities between the two signals in the frequency domain and contains relative phase information. It is obtained from:

$$G_{xy}(j\omega) = S_x(j\omega)S_y^*(j\omega)$$

In general, this will be a complex quantity with real and imaginary parts, sometimes referred to as the coincident and quadrature spectral densities, respectively. That is

$$G_{xy}(j\omega) = Co(\omega) + jQuad(\omega)$$

The magnitude of the cross-spectral density is real valued and for random functions is given by the polar combination of the averaged Co and Quad spectra:

$$|G_{xy}(j\omega)| = [Co^2(\omega) + Quad^2(\omega)]^{1/2}$$

The phase of the cross-spectral density is also real-valued and is given by

$$\theta_{xy}(\omega) = \theta_x(\omega) - \theta_y(\omega) = \text{Arctan}\left[\frac{Quad(\omega)}{Co(\omega)}\right]$$

The phase of the cross-spectral density is the phase difference between the signals x(t) and y(t).

Transfer Function

The transfer function $H_{xy}(j\omega)$ between two signals x(t) and y(t) provides frequency domain information about the nature of the transfer of a signal through a system. It is a complex quantity having real and imaginary parts and is given by the cross spectral density between the two signals normalized with respect to the auto-spectral density of the signal considered as input:

$$H_{xy}(j\omega) = \frac{G_{xy}(j\omega)}{G_{xx}(\omega)}$$

Its magnitude, $|H_{xy}(j\omega)|$, is real valued and is given by polar combination of the real and imaginary parts. Its phase is also real valued and given by the inverse tangent of the ratio of the imaginary to real parts, and is clearly the same as the phase of the cross-spectral density.

Ordinary Coherence Function

The ordinary coherence function $\gamma^2_{xy}(\omega)$ between two random signals, say $x(t)$ and $y(t)$, is a numerical measure of the similarities between the two signals at each frequency. It is given by the square of the ensemble averaged cross-spectral density normalized with respect to the product of the individual averaged auto-spectral densities.

$$\gamma^2_{xy}(\omega) = \frac{|G_{xy}(j\omega)|^2}{G_{yy}(\omega)G_{xx}(\omega)}$$

It is a real valued function which must take on a value between zero and one, with high (low) coherence at a particular frequency meaning high (low) correlation at that frequency. As described in chapter 5 it may, under the appropriate circumstances, be interpreted as the fractional portion of the mean-square value at $y(t)$ which is due to the input $x(t)$. It should be pointed out that when computing coherence functions from spectral density estimates, as defined in the equation above, the ensemble averaging must be performed on the individual spectral densities, and not on the computed

coherence function from each sample. The latter approach will always yield a coherence of unit (see ref. (26)).

Cross-Correlation Function

The time domain definition of the cross-correlation function, for random signals is:

$$R_{xy}(\tau) = \lim_{T\to\infty} \frac{1}{T} \int_0^T x(t)y(t + \tau)dt$$

The cross-correlation function and the cross-spectral density are Fourier transform pairs and hence $R_{xy}(\tau)$ may also be computed from:

$$R_{xy}(\tau) = \mathcal{F}^{-1}[G_{xy}(j\omega)]$$

The DSP used in this investigation utilized the Fourier transform relationship above to compute the cross-correlation functions.

REFERENCES

1. "Transportation Noise and Its Control," DOT Report P5630.1, U.S. Department of Transportation, 1972.

2. Lighthill, M. J.: "On Sound Generated Aerodynamically, I. General Theory," Proc. Roy. Soc. (London), Series A, Vol. 211, 1952, pp. 564-587.

3. "Effects of Forward Velocity on Jet Mixing Noise," Lockheed-Georgia Company, NASA CR-2702, 1976.

4. von Glahn, U., Groesbeck, D., and Goodykoontz, J.: "Velocity Decay and Acoustic Characteristics of Various Nozzle Geometries with Forward Velocity," AIAA Paper No. 73-629, 1973.

5. "High Velocity Jet Noise Source Location and Reduction," Task 4 Final Report - Development/Evaluation of Techniques for Inflight Investigation, General Electric Company, FAA Report No. FAA-RD-76-79, IV, 1977.

6. Hanson, D. B.: "Study of the Inflow Distortion Sources in the NASA QF-1B Fan Using Measured Blade and Vane Pressures," NASA CR (to be assigned), NASA Contract No. NAS3-19749.

7. Dietrich, D. A., Heidmann, M. F., and Abbott, J. M.: "Acoustic Signatures of a Model Fan in the NASA-Lewis Anechoic Wind Tunnel," AIAA Paper 77-59, 1977.

8. Stone, J. R.: "On The Effects of Flight on Jet Engine Exhaust Noise," NASA TM X-71819, 1975.

9. Merriman, J. E., et al.: "Forward Motion and Installation Effects on Engine Noise," AIAA Paper No. 76-584, 1976.

10. Kozlowski, H., and Packman, A.: "Aerodynamic and Acoustic Tests of Duct-Burning Turbofan Exhaust Nozzles," NASA CR 2628, 1976.

11. Gutierrez, O. A.: "Aeroacoustic Studies of Coannular Nozzles Suitable for Supersonic Cruise Aircraft Applications," in Proceedings of the SCAR Conference, Part 1, NASA CP-001, 1976.

12. Doyle, V. L., and Matta, R. K.: "Attenuation of Upstream Generated Low Frequency Noise by Gas Turbines," NASA CR-135219, 1976.

13. Gerend, R. P., Kumasaka, H. P., and Roundhill, J. P.: "Core Engine Noise," AIAA Paper 73-1027, 1973.

14. Hoch, R. G., Thomas, P., and Weiss, E.: "An Experimental Investigation of the Core Engine Noise of a Turbofan Engine," AIAA Paper 75-526, 1975.

15. Mathews, D. C., and Perachio, A. A.: "Progress in Core Engine and Turbine Noise Technology," AIAA Paper 74-948, 1974.

16. Burdsall, E. A., Brochu, F. P., and Scaramella, V. M.: "Results of Acoustic Testing of the JT8D-109 Refan Engines," NASA CR-134875, 1975.

17. Abdelhamid, A. N., et al.: "Noise Characteristics of Combustion Augmented High Speed Jets," AIAA Paper No. 73-189, 1973.

18. Strahle, W. C., Muthukrishnan, M., and Neale, D. H.: "Coherence Between Internal and External Noise Generated by Gas Turbine Combustors," AIAA Paper 77-20, 1977.

19. Mathews, D. C., Rekos, N. F., and Nagel, R. T.: "Combustion Noise Investigation," FAA Report No. FAA RD-77-3, 1977.

20. Lighthill, M. J.: "On Sound Generated Aerodynamically, II. Turbulence as a Source of Sound," Proc. Roy. Soc. (London), Series A, Vol. 222, 1954, pp. 1-32.

21. Lilley, G. M.: "The Generation of Sound in a Mixing Region," U.S. Air Force Report AFAPL-TR-72, Vol. IV, 1972.

22. Phillips, O. M.: "On the Generation of Sound by Supersonic Turbulent Shear Layers," J. Fluid Mechanics, Vol. 9, Part 1, 1960, pp. 1-28.

23. Goldstein, M. E.: "Aeroacoustics," NASA SP-346, 1974.

24. Rayleigh, J. W.: "The Theory of Sound," Dover Publications, 1945.

25. Siddon, T. E.: "Surface Dipole Strength by Cross-Correlation Method," J. Acoustical Soc. of America, Vol. 53, No. 2, 1973, pp. 619-633.

26. Bendat, J. S., and Piersol, A. G.: Random Data: Analysis and Measurement Procedures, John Wiley & Sons, 1971.

27. Papoulis, A.: Probability, Random Variables, and Stochastic Processes, McGraw-Hill Book Company, 1965, p. 317.

28. Curle, N.: "The Influence of Solid Boundaries Upon Aerodynamic Sound," Proc. Roy. Soc. (London), Series A, Vol. 231, 1955.

29. Morse, P. M., and Ingard, K. V.: Theoretical Acoustics, McGraw Hill Book Company, 1968, p. 511.

30. Halvorsen, W. G., and Bendat, J. S.: "Noise Source Identification Using Coherent Output Power Spectra," Sound and Vibration, Vol. 9, No. 8, 1975, pp. 15-24.

31. Moore, M. T.: "Sound Separation Probes for Flowing Duct Noise Measurements," Paper No. 4.5.1, Proceedings of the 23rd International Instrumentation Symposium, 1977, pp. 451-459.

32. Matta, R. K., Sandusky, G. T., and Doyle, V. L.: "GE Core Engine Noise Investigation, Low Emission Engines," DOT Report No. FAA-RD-77-4, 1977.

33. Ho, P. Y., and Tedrick, R. N.: "Combustion Noise Prediction Techniques for Small Gas Turbine Engines," Inter-Noise 72 Proceedings; 1972.

34. Strahle, W. C., et al.: "An Investigation of Combustion and Entropy Noise," NASA CR-135220, 1977.

35. Shields, F. D., and Bass, H. E.: "Atmospheric Absorption of High Frequency Noise and Application to Fractional Octave Bands," NASA CR-2760, 1977.

36. Montegani, F. J.: "Some Propulsion System Noise Data Handling Conventions and Computer Programs Used at the Lewis Research Center," NASA TM X-3013, 1974.

37. Huff, R. G., Clark, B. J., and Dorsch, R. G.: "Interim Prediction Method for Low Frequency Core Engine Noise," NASA TM X-71627, 1974.

38. Enochson, L. D., and Goodman, N. R.: "Gaussian Approximation to the Distribution of Sample Coherence," AFFDL TR-65-67, Air Force Flight Dynamics Laboratory, 1965.